

**VIRTUAL PROTOTYPING OF AXIAL PISTON MACHINES
OF SWASHPLATE TYPE**

by
Rene Chacon

A Dissertation

Submitted to the Faculty of Purdue University

In Partial Fulfillment of the Requirements for the degree of

Doctor of Philosophy



School of Agricultural & Biological Engineering

West Lafayette, Indiana

August 2019

**THE PURDUE UNIVERSITY GRADUATE SCHOOL
STATEMENT OF COMMITTEE APPROVAL**

Dr. Andrea Vacca, Co-Chair

Department of Agricultural and Biological Engineering

Dr. Farshid Sadeghi, Co-Chair

Department of Mechanical Engineering

Dr. Raymond J. Cipra

Department of Mechanical Engineering

Dr. Carlo Scalo

Department of Mechanical Engineering

Approved by:

Dr. Nathan S. Mosier

Head of the Graduate Program

To my family

ACKNOWLEDGMENTS

First of all, I would like to thank my advisor Dr. Monika Ivantysynova for the support, guidance and encouragement throughout my research here at Maha Fluid Power Research Center. None of this work would've been possible without her guidance. She will be dearly missed. I would like to give a special acknowledgement to Dr. Andrea Vacca and Dr. Farshid Sadeghi for taking on the responsibility of committee co-chairs in Monika's absence. Their guidance on the final months of my Ph.D. has been essential.

Second, I would like to thank my family, although, they are hundreds of miles away from Lafayette, IN. Their unconditional support all throughout my student life has been of the upmost importance for me. None of these would be possible without their support, many thanks for all.

Third, to my friends during my stay here at the Maha Fluid Power Lab. Thank you for the endless discussions on the research topic, sharing your knowledge, and for your friendship.

Finally, the staff at Maha. Special thanks to Susan Gauger for being such a good person. You really made of Maha that much more special, you were of the biggest help to me when I needed it. For that I thank you. Also, Ben, David, Connie and Deb, thank you for your work here at Maha, you make this place a unique place in the world.

TABLE OF CONTENTS

LIST OF TABLES	8
LIST OF FIGURES	9
NOMENCLATURE	14
LIST OF ABBREVIATIONS.....	16
ABSTRACT.....	17
1. INTRODUCTION	18
1.1 Background and Motivation	19
1.2 State of the Art	21
1.3 Aim of this Work	27
1.4 Original Contributions of this work.....	27
2. INTRODUCTION TO AXIAL PISTON MACHINES OF SWASH PLATE TYPE	28
2.1 Kinematics of Axial Piston Machines of Swashplate Type.....	28
2.2 The Function of the Lubricating Interfaces	29
2.3 External Loads on the Rotating Group	30
2.4 Lubricating Interfaces Geometry	34
2.4.1 Cylinder Block/Valve plate Interface	34
2.4.2 Slipper/Swash Plate Interface	35
2.4.3 Piston/Cylinder Interface	36
3. NUMERICAL MODELS FOR VIRTUAL PROTOTYPING	38
3.1 Pressure Module.....	39
3.2 Thermal model to predict port and case fluid temperatures	42
3.3 Thermo-Elastohydrodynamic Model	44
3.3.1 Grid Generation and Boundary Conditions	47
3.3.2 Cylinder Block/Valve Plate Interface	47
3.3.3 Elastic deformation due to pressure loads	50
3.3.4 Thermal boundaries	54
3.3.5 Piston / Cylinder Interface	57
3.3.6 Elastic deformation due to pressure loads	57

3.3.7	Thermal boundaries	58
3.3.8	Slipper / Swash plate Interface	60
3.3.9	Thermal boundaries	62
3.3.10	Slipper/Swash plate interface convection coefficients calculation	65
4.	DESIGN METHODOLOGY OF SWASH PLATE TYPE AXIAL PISTON MACHINES	67
4.1	General Design Methodology Overview	67
4.2	Preliminary Design	68
4.3	Virtual Prototyping	72
4.4	Case Study	75
5.	VALVE PLATE ANALYSIS AND DESIGN OPTIMIZATION.....	77
5.1	Objectives and constraints	84
5.2	Valve Plate Optimization Design Variables	85
5.3	Design parameters settings	87
5.3.1	Valve plate optimization example	88
5.3.1.1	Valve plate optimization example results.....	89
6.	SOLID BODIES DESIGN AND FEM ANALYSIS.....	95
6.1	Impact if the elastic deformation of the end case valve plate assembly	97
6.2	Solid bodies design methodology	103
7.	Virtual Prototyping for Lubricating Interfaces	108
7.1	Material selection.....	111
7.2	Operating conditions	112
7.3	Cylinder Block/Valve Plate Interface Design Variables within Virtual Prototyping	114
7.4	Cylinder Block/Valve Plate Interface Design Prototyping Example.....	116
7.5	Slipper/Swash Plate Interface Design within Virtual Prototyping	122
7.6	Slipper/Swash Plate Interface Design Prototyping Example.....	123
7.7	Piston/Cylinder Interface Design within Virtual Prototyping	126
8.	PHYSICAL PROTOTYPE AND EXPERIMENTAL SETUP	127
8.1	Component Inspection	128
8.2	Axial Piston Machine Assembly.....	132
8.3	Test Stand.....	133
9.	EXPERIMENTAL RESULTS	136

9.1 Experimental Results and Simulation Comparison	138
9.2 Discussion	143
10. CONCLUSIONS	144
APPENDIX.....	146
REFERENCES	147
VITA.....	151
PUBLICATIONS.....	152

LIST OF TABLES

Table 3.1.: Thermal boundary conditions applied to the cylinder block	56
Table 3.2.: Thermal boundary conditions applied to the valve plate & end case assembly	56
Table 3.3.: Piston/cylinder interface thermal boundaries	59
Table 3.4.: Thermal boundary conditions for the Slipper	64
Table 3.5.: Thermal boundary conditions for the swashplate	64
Table 3.6.: Convection coefficients used for the slipper swashplate interface.	66
Table 4.1.: Objective functions for the valve plate optimization.....	76
Table 5.1.: Objective functions for the valve plate optimization.....	84
Table 5.2.: Constraints for the valve plate optimization.....	85
Table 5.3.: Operating conditions range for the axial piston machine	87
Table 5.4.: Valve plate optimization variable boundaries	88
Table 5.5.: Operating conditions range for the axial piston machine	88
Table 5.6.: Valve plate optimization result parameters	89
Table 5.7.: Valve plate optimization simulation results	91
Table 7.1.: Material properties influencing the lubricating interfaces' behavior	111
Table 7.2. Operating conditions.....	113
Table 8.1. Operating conditions range.....	127
Table 8.2. Test rig set up components.	135

LIST OF FIGURES

Figure 1.1. Axial piston machine cross-section.	18
Figure 1.2. Axial piston machine components.....	19
Figure 1.3. Measured overall efficiency of variable displacement axial piston motors at 2000 rpm and 200 bar (from Baker and Ivantysynova, 2009).	20
Figure 1.4. Valve plate optimization method (from Kalbfleisch, 2015).....	23
Figure 2.1. Schematic of an Axial Piston Machine (Seeniraj & Ivantysynova, 2009).	28
Figure 2.2. Axial Piston Machine Swash Plate Type Cross-section.....	30
Figure 2.3. Cylinder Block Free Body Diagram.....	31
Figure 2.4. Piston/Slipper Assembly Free Body Diagram.....	32
Figure 2.5. Free Body Diagram of the Slipper Forces.....	33
Figure 2.6. Cylinder block/valve plate interface schematic.....	34
Figure 2.7. Slipper/swash plate representation.	36
Figure 2.8. Piston/cylinder interface control points.....	37
Figure 3.1. Multi-domain axial piston machine model.....	39
Figure 3.2. Instantaneous Pressure Calculation Control Volume.	40
Figure 3.3. Simplified heat and mass transfer in the axial piston machine port and case flow temperature prediction model (Shang & Ivantysynova, 2015).	43
Figure 3.4. Port and case flow temperature prediction model scheme (Shang & Ivantysynova, 2015).	43
Figure 3.5. Fluid structure thermal interaction model example cylinder block/valve plate interface (Zecchi, 2013).	46
Figure 3.6. Structure grid used to solve the fluid flow (Zecchi, 2013).....	48
Figure 3.7. Boundary conditions for the solution of the Reynolds equation (Zecchi, 2013).....	49
Figure 3.8. Boundary conditions for the energy equation (Zecchi, 2013).....	50
Figure 3.9. Solid mesh for the cylinder block.....	51
Figure 3.10. Deformation due to the reference pressure of 100 bar applied on an element face on the sealing land (a) and in one of the displacement chambers (b) (Zecchi, 2013).	52
Figure 3.11. Valve plate surface deflection, comparison between linear and non-linear (deflection in z-direction).....	53

Figure 3.12. Cylinder block /valve plate interface pressure boundaries.....	53
Figure 3.13. Cylinder block /valve plate interface thermal boundaries.....	54
Figure 3.14. Piston and cylinder block mesh.....	57
Figure 3.15. Piston/cylinder interface pressure boundaries.....	58
Figure 3.16. Piston/cylinder interface thermal boundaries.....	59
Figure 3.17. Structure grid used to solve the fluid flow energy equation (Schenk, 2014).	60
Figure 3.18. Structured grid used for the Reynolds (left) and energy equations (right).....	60
Figure 3.19. Fine mesh of a bimetal slipper.....	61
Figure 3.20. Pressure boundary conditions on the slipper and swash plate.....	62
Figure 3.21. Thermal boundary conditions on the slipper and swash plate.....	63
Figure 3.22. Fluid flow around rotating kit.....	65
Figure 3.23. CFD simulation results, convection coefficients.....	65
Figure 4.1. General design methodology flowchart.....	67
Figure 4.2: Preliminary design flowchart.	69
Figure 4.3. Main geometrical dimension of axial piston machines of swash plate type.	70
Figure 4.4. Axial piston machine main dimensions.....	71
Figure 4.5. Virtual prototyping flowchart.....	74
Figure 4.6. 3D computational model. Cross-section lateral view (a) and isometric view (b) are shown (Chacon, 2019).	76
Figure 5.1. Valve plate representation.	78
Figure 5.2: Valve plate area opening to the displacement chamber representation.....	79
Figure 5.3. Opening area profile to the displacement chamber from the discharge and suction ports representation.	80
Figure 5.4. Opening area profile to the displacement chamber from the discharge and suction ports as a function of the shaft angle.	80
Figure 5.5. Four quadrants of operation of general swash plate type axial piston machine (shaft rotation in a single direction).	82
Figure 5.6. Valve plate optimization flowchart.	83
Figure 5.7: Nonlinear Groove Area Opening (Kalbfleisch, 2015).	85
Figure 5.8. Valve plate optimization results, Vol. efficiency vs $\Delta Q_{hp}(OC1)$	90
Figure 5.9. Valve plate optimization results, Vol. efficiency vs $\Delta M_x(OC1)$	90

Figure 5.10. Recommended valve plate volumetric efficiency.	92
Figure 5.11. Recommended valve plate ΔQ_{HP}	93
Figure 5.12. Recommended valve plate ΔM_X	93
Figure 5.13. Recommended valve plate M_X	94
Figure 6.1. Cylinder block/valve plate interface fluid film thickness.	95
Figure 6.2. Cylinder block surface elastic deformation.	96
Figure 6.3. Cylinder block/valve plate elastic deformation.	96
Figure 6.4. End case designs rib less and rib design shown in top and bottom, respectively.	97
Figure 6.5. Pressure boundary conditions for the cylinder block valve plate interface.	98
Figure 6.6. Valve plate surface deformation (2500 rpm 350 bar at full displacement).	99
Figure 6.7. Valve plate surface deformation enlarged comparison (2500 rpm 350 bar at full displacement).	99
Figure 6.8. Cylinder block/valve plate fluid film thickness design A (a) and design B (b) (2500 rpm 350 bar at full displacement).	100
Figure 6.9. Fluid film thickness design A (left) and design B (right) (2500 rpm 350 bar at full displacement).	100
Figure 6.10. Simulation results (2500 rpm 350 bar at full displacement).	101
Figure 6.11. Simulation results (1000 rpm 100 bar at 50% displacement).	102
Figure 6.12. Simulation results (2500 rpm 350 bar at 50% displacement).	103
Figure 6.13. Solid body design methodology.	104
Figure 6.14. Example of swash plate pressure field calculated in the TEHD model.	105
Figure 6.15. An example of the swash plate pressure boundaries applied to the three-dimensional mesh.	105
Figure 6.16. Example of swash plate von Mises stress distribution.	107
Figure 6.17. Example of swash plate sliding surface deformation in the z-axis.	107
Figure 7.1: Lubricating interfaces general design methodology.	109
Figure 7.2. Cross section of bimetal valve plate mesh.	112
Figure 7.3. Cross section of bimetal valve plate mesh.	112
Figure 7.4. Cylinder block/valve plate interface schematic.	114
Figure 7.5. Cylinder block length and canal length representation.	115
Figure 7.6: Cylinder block's bottom view and sealing land design parameters.	115

Figure 7.7. Endcase designs.....	116
Figure 7.8. Energy dissipation in the cylinder block/valve plate interface (n=4000 rpm, Δp =450 bar and full displacement).....	118
Figure 7.9. Leakage flow from the cylinder block/valve plate interface (n=4000 rpm, Δp =450 bar and full displacement).....	118
Figure 7.10. Velocity correction (n=4000 rpm, Δp =450 bar and full displacement).	119
Figure 7.11. Energy dissipation and number of contacts predicted from the cylinder block/valve plate interface (n=4000 rpm, Δp =450 bar and full displacement).	120
Figure 7.12. Underbalance, recommended, and overbalanced designs comparison breakdown by leakage, viscous friction, and total energy dissipation.	120
Figure 7.13. Three-dimensional representation of the fluid film, color scale fluid film thickness (n=4000 rpm, Δp =450 bar and full displacement).....	121
Figure 7.14. Three-dimensional representation of the fluid film, color scale pressure (n=4000 rpm, Δp =450 bar and full displacement).....	122
Figure 7.15. Slipper/swash plate interface schematic.....	122
Figure 7.16. Slipper design dimensions.....	123
Figure 7.17. Energy dissipation in the slipper/swash plate interface (n=4000 rpm, Δp =450 bar and full displacement).....	124
Figure 7.18. Fluid film thickness (n=4000 rpm, Δp =450 bar and full displacement).	125
Figure 7.19. Fluid film thickness and pressure field in color (n=4000 rpm, Δp =450 bar and full displacement).	125
Figure 7.20. Piston/cylinder interface schematic.....	126
Figure 7.21. Piston/cylinder interface main dimensions.....	126
Figure 8.1. Axial piston machine of swash plate type physical prototype.	128
Figure 8.2. CMM inspection of components.	128
Figure 8.3. Piston dimensions and tolerances.....	129
Figure 8.4. Piston/slipper assembly prototype.....	129
Figure 8.5. Three profilometer traces across the barrel piston surface.....	130
Figure 8.6. Slipper profilometer trace.....	130
Figure 8.7. Slipper leading edge dimensions.....	131
Figure 8.8. Slipper leading edge profilometer traces.....	131
Figure 8.9. Axial piston machine of swash plate exploded view.....	132
Figure 8.10. Assembly cross-section.	133

Figure 8.11. Fixture to install cylinder block spring and snap ring.	133
Figure 8.12. Steady state test rig with 24 cc prototype mounted.	134
Figure 8.13. ISO schematic of the steady-state test rig.....	134
Figure 9.1. Prototype efficiencies at $n = 1000$ rpm, $T = 52$ °C, and $\Delta p = 50$ –400 bar.....	136
Figure 9.2. Prototype efficiencies at $n = 2000$ rpm, $T = 52$ °C, and $\Delta p = 50$ –400 bar.....	137
Figure 9.3. Prototype efficiencies at $n = 3000$ rpm, $T = 52$ °C, and $\Delta p = 50$ –400 bar.....	137
Figure 9.4. Volumetric efficiency measured compared against simulated at $n = 1000$ rpm, $T = 52$ °C, and $\Delta p = 50$ –400 bar.....	138
Figure 9.5. Volumetric efficiency measured compared against simulated at $n = 2000$ rpm, $T = 52$ °C, and $\Delta p = 50$ –400 bar.....	139
Figure 9.6. Volumetric efficiency measured compared against simulated at $n = 3000$ rpm, $T = 52$ °C, and $\Delta p = 50$ –400 bar.....	139
Figure 9.7. Mechanical efficiency measured compared against simulated at $n = 1000$ rpm, $T = 52$ °C, and $\Delta p = 50$ –400 bar.....	140
Figure 9.8. Mechanical efficiency measured compared against simulated at $n = 2000$ rpm, $T = 52$ °C, and $\Delta p = 50$ –400 bar.....	140
Figure 9.9. Mechanical efficiency measured compared against simulated at $n = 3000$ rpm, $T = 52$ °C, and $\Delta p = 50$ –400 bar.....	140
Figure 9.10. Drain flow comparison at $n = 1000$ rpm, $T = 52$ °C, and $\Delta p = 50$ –400 bar.....	141
Figure 9.11. Drain flow comparison at $n = 2000$ rpm, $T = 52$ °C, and $\Delta p = 50$ –400 bar.....	141
Figure 9.12. Drain flow comparison at $n = 3000$ rpm, $T = 52$ °C, and $\Delta p = 50$ –400 bar.....	142
Figure 9.13. Worn slipper retainer plate after measurements.	143

NOMENCLATURE

a	Acceleration	[m/s ²]
A	Area	[m ²]
A_o	Displacement chamber opening are	[m ²]
A_D	Surface area at the bottom of the displacement chamber	[m ²]
A_K	Piston surface area	[m ²]
b	Breadth	[m]
d_K	Piston diameter	[m]
h	Gap height	[m]
K	Bulk modulus	[Pa]
M	Torque	[Nm]
H_K	Piston stroke	[m]
F	Force	[N]
F_{BZ}	Resulting force in an axial direction	[N]
F_{FB}	Spring force	[N]
F_{DB}	Force due to pressure in displacement chamber, applied to the block	[N]
F_{DK}	Force due to pressure in displacement chamber, applied to the piston	[N]
F_{TB}	Friction force due to viscous friction in the piston/cylinder interface, applied to the block	[N]
F_{TK}	Friction force due to viscous friction in the piston/cylinder interface, applied to the piston	[N]
F_{SK}	Swashplate reaction force	[N]
$F_{\omega B}$	Force due to centripetal acceleration transferred to block	[N]
$F_{\omega K}$	Force due to centripetal acceleration on the piston/slipper assembly	[N]
FRB	Total radial force transmitted to the cylinder block	[Nm]
M	Torque	[Nm]
m_K	Piston mass	[kg]

n	Shaft rotational speed	[rpm]
p	Pressure	[Pa]
Δp	Pressure differential	[Pa]
P	Power	[W]
Q	Flow rate	[m ³ /s]
R	Pitch radius	[m]
RB	Outer radius cylinder block	[m]
r	Radial position	[m]
sK	Piston displacement	[m]
T	Temperature	[°C]
t	Time	[s]
V	Velocity	[m/s]
vK	Piston velocity	[m/s]
Vg	Geometric displacement	[m ³]
(r, ϑ, z)	Cylindrical reference system	
(x, y, z)	Cartesian reference system	
β	Swash plate angle	[°]
μ	Dynamic viscosity	[Pa s]
ρ	Oil density	[kg/m ³]
Φd	Viscous dissipation	[W]
φ	Shaft angular position	[°]
ω	Angular velocity	[rad/s]

LIST OF ABBREVIATIONS

B	Block
DC	Displacement chamber
LP	Low pressure
HP	High pressure
K	Piston
f	Fluid film
G	Slipper
T	Cylinder bore
CB	Cylinder block
VP	Valve plate
Δ	Variation
l	Loss
S	Leakage
m	Mechanical

ABSTRACT

Author: Chacon, Rene PhD

Institution: Purdue University

Degree Received: August 2019

Title: Virtual Prototyping of Axial Piston Machines of Swashplate Type

Committee Chairs: Monika Ivantysynova, Andrea Vacca, Farshid Sadeghi

Axial piston machines are widely used in the industry ranging from aerospace, agriculture, automotive, heavy machinery, etc. These applications require better pumps and motors to meet current market demands such as higher power density in hydraulic units, smarter pumps (diagnostics and prognostics), higher efficiencies, and compactness. The current state-of-the-art in pump design is mostly based on heuristic design approach with very limited use of numerical tools since the invention of this positive displacement machine until the present time. The numerical tools being used do not capture the physical phenomena in the thin fluid film between the rotating group components. The work presented in this dissertation aims to demonstrate the feasibility of virtual prototyping utilizing a combination of in-house developed multi-domain models and to propose a novel computational based design methodology for axial piston machines. The methodology is an iterative process between the virtual components in 3D CAD models and the function evaluations for the design requirements utilizing the numerical models which provide an accurate prediction to the behavior of the mechanical components working together. To validate the proposed methodology a case study on a 24 cc/rev axial piston machine was carried out. The machine was built virtually, simulated, and optimized for desired performance. A physical prototype was built based on the case study and tested successfully for forty-five operating conditions.

1. INTRODUCTION

Axial piston machines of swash plate type are a commonly used positive displacement machines, which can work as pumps or motors depending on the loading of the hydraulic system. As shown in Fig. 1.1 they are composed of a rotating group containing the cylinder block and the piston/cylinder assembly, the swash plate, the valve plate, the shaft, and the housing with the end case. The working principal of this type of positive displacement machines is quite simple. The pistons are encased in the cylinder block and are supported via slippers on the swashplate surface. The cylinder block and piston/slipper assemblies rotate together with the shaft which is driven by a prime mover. As the cylinder block rotates together with the piston/slipper assembly, the piston/slipper assembly translates axially within the cylinder bore since it is pressed on the swash plate. The inclination of the swash plate causes a reciprocating motion of the piston, when the piston is the closest to the valve plate is called the inner dead center and when it is the farthest away it is called the outer dead center. The piston starts moving from the inner dead center (IDC) towards the outer dead center (ODC) allowing fluid from the suction port to flow into the displacement chamber. Similarly, the fluid is displaced to discharge port when the piston moves from its ODC to IDC. Figure 1.2 shows the main components of a fixed swash plate type axial piston machine.

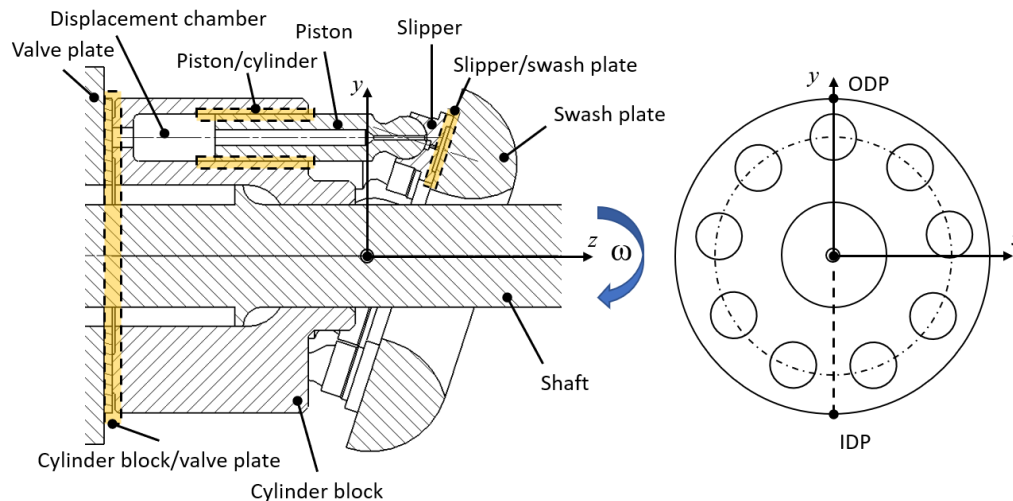


Figure 1.1. Axial piston machine cross-section.

1.1 Background and Motivation

Fluid power systems present multiple advantages, such as high-power density and compactness. This technology is present in a broad range of industrial applications such as aerospace, agriculture, automotive, construction, manufacturing, robotics, etc. Recent developments in fluid power architectures require high efficiencies from positive displacement machines on a wider range of operations such as displacement-controlled systems, power split transmissions, and hydraulic hybrids. The reason for this is that the positive displacement machines are the main source of energy losses in those new system architectures once the throttling losses occurring in valves have been removed.

Axial piston machines of swash plate type are one of the most popular types of positive displacement machines due to their compactness, high efficiencies, ease of controllability of the displacement, and high working pressures. Historically current positive displacement machines have been designed based on a heuristic approach and a limited use of numerical models nowadays. Therefore, increasing the cost of prototypes limits the potential of more sophisticated designs due to limited resources. The cost of the current design process can be greatly diminished by the introduction of virtual prototyping. Virtual prototyping will also allow the pump designers to explore a much larger design space with innovative design possibilities at much lower costs. Also, currently, the overall efficiency of variable axial piston machines drops considerably with reduced displacement. Figure 1.1 shows the drop of overall efficiencies with reducing angle for two types of axial piston machines; swash plate and bent axis type. This comparison clearly shows a higher efficiency of the bent axis type over the whole range of operating conditions.

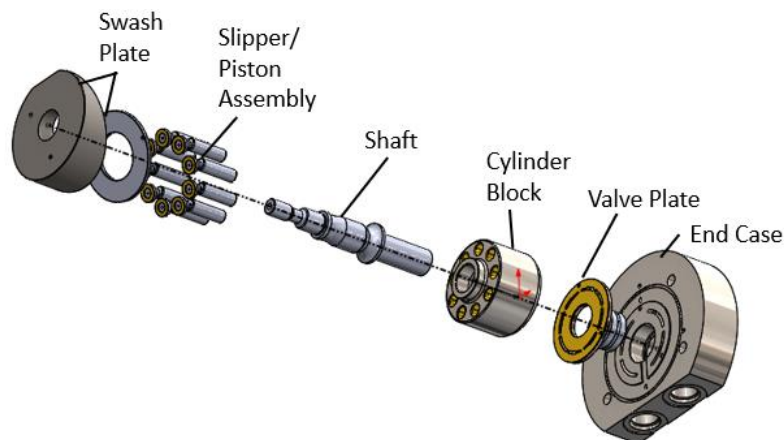


Figure 1.2. Axial piston machine components.

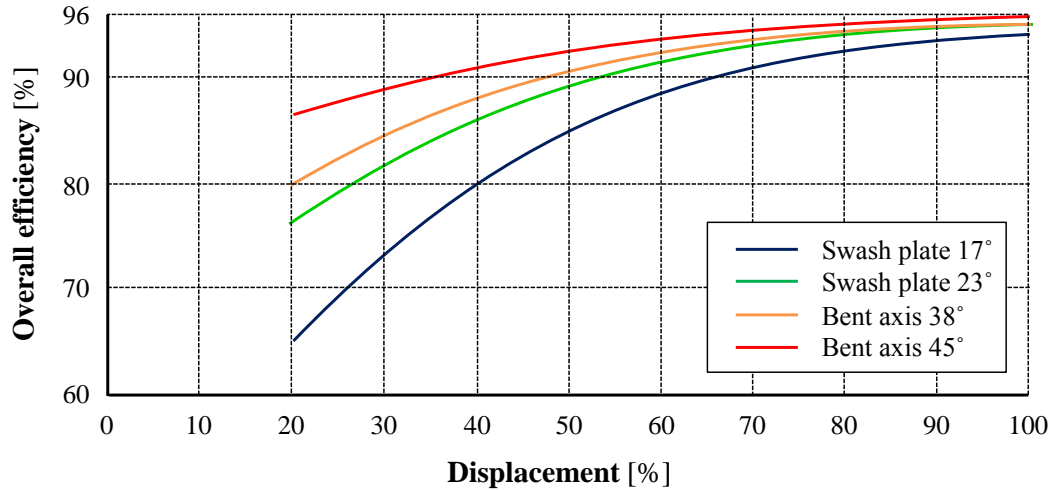


Figure 1.3. Measured overall efficiency of variable displacement axial piston motors at 2000 rpm and 200 bar (from Baker and Ivantysynova, 2009).

As mentioned previously, the current state-of-the-art of design of axial piston machines is a heuristic design approach with a limited amount of numerical modelling which derives in an expensive process, usually requiring years to develop a new pump. The design of these machines is considered like black box design where the designers change different parameters until the pump passes laboratory tests successfully and finally works under all the desired operating conditions. Instead designers have used and still use very simplified calculations methods for determination of the part dimensions of the piston/cylinder, cylinder block/valve plate and slipper/swash plate interface. The main simplifications are to neglect the hydrodynamic effects in those interfaces, assuming parallel surfaces without deformation due to pressure and thermal loading, and neglecting the micro motion of these parts. In the current design practice so called balance factors are utilized to capture some of these unknown effects. For that reason, prototypes need to be manufactured based on the initial design. The prototype parts will be tested under real operating conditions. The likelihood of failing within initial test is almost certain. The initial design usually requires many design reviews, repeated manufacturing of parts, and repeated machine testing. The process will be repeated until a design is found which successfully passes all testing.

The swash plate type axial piston machine has three critical interfaces, which parts form the rotating group of the machine and determine whether the pump or motor will work or fail. These three lubricating interfaces are formed between the piston and cylinder bore, the slipper and swash plate and the cylinder block and valve plate. These three lubricating interfaces perform two

important simultaneous functions: bearing of the external loads exerted on the rotating group and sealing of the pressurized fluid from leaking to the pump case. The design of these three lubricating interfaces has to ensure the generation of a stable load carrying fluid film between these heavily loaded parts preventing metal-to-metal contact between the parts. The fluid film thickness depends on many design parameters: shape of the parts (the pistons, the slippers, the cylinder block, the swash plate, the valve plate and the end case), the material selection and the final part dimensions. The complexity of the physical phenomena contributing to the generation of a stable fluid film requires to model and solve the fluid structure interaction phenomena in all three pump lubricating interfaces. The models capturing the complex physics are computationally very expensive and have never been part of a design process of axial piston machines.

Extensive research on the physics behind the behavior of these lubricating interfaces together with a large growth in computational power over the last couple of decades have led the Maha Fluid Power Research center to the development of a set of advanced multi-domain numerical models. The advanced multi-domain numerical models can be used to gain a unique insight into the behavior of the lubricating interfaces and allow predictions of fluid film thickness, load carrying ability, leakage flow, energy dissipation and the temperature fields of those fluid films separating high dynamic loaded moving parts of the axial piston machine. These numerical models have enabled and motivated the work in this dissertation.

The goal of this thesis is to propose a new design process based on virtual prototyping. The dimensions and shapes of the parts forming the important tribological pump interfaces, namely the pistons, the slippers, the cylinder block, the swash plate, the valve plate and the end case, are determined within a computational framework which utilizes the before mentioned in-house developed models for the calculation of the fluid film behavior and a lumped parameter model for the valve plate port design. Finally, to demonstrate the feasibility of this novel approach.

1.2 State of the Art

In the last few decades, the growing computational power has empowered researchers around the globe in distinct areas to develop more advanced and complex numerical models. These computational models have enabled to revolutionize design processes in a variety of different

fields. As mentioned previously, positive displacement machines historically have been designed heuristic design approach conformed by rules of thumb, experiments, and a small amount of numerical analysis.

To better understand the complex physics taking place in the main lubricating interfaces of axial piston machines, a significant amount of research has been conducted by many researchers in the last four decades worldwide. In those main tribological interfaces (cylinder block/valve plate, piston/cylinder and slipper/swash plate interfaces) a thin fluid film is necessary to bear the external loads derived from the kinematics of the machines and to seal the pressurized fluid in the displacement chambers. The main external load imposed on parts of the machine originates from the periodically changing pressure in the displacement chamber. The valve plate design can be used to influence the pressure rise and fall in each displacement chamber while changing the connection of the displacement chamber between suction and discharge port.

The shape of the displacement chamber pressure profile strongly influences the pulsating forces acting on machine parts and will also impact the noise generation of the machine. Many researchers have focused on valve plate design features with the goal to reduce noise emissions of axial piston machines. Becker (1970) studied the impact of valve plate timing on the pressure in the displacement chamber and ports. Helgestad et al. (1974) investigated the effect of pressure rise in the displacement chambers in noise generation axial piston machines. Many numerical models to simulate the dynamics in axial piston machines were developed by, to name some, Edge and Darling (1986), Palmberg (1989), Harrison and Edge (2000), Ivantysynova (1999), Manring (2000), and Wieczorek and Ivantysynova (2002). These models were part of research towards reducing noise emission from axial piston machines by introducing design changes, some of these were pre-compression filter volumes (Pettersson et al., 1991; Ivantysynova et al., 2005; Johansson, 2005), cross-angle of the swash plate (Johansson et al., 2002; Manring and Dong, 2004), and others. More recently (Seeniraj and Ivantysynova, 2008; Kim, 2012; Kalbfleisch, 2015) developed VpOptim a genetic algorithm optimization tool for the valve plate design. Kalbfleisch (2015) coupled the information coming from the pump dynamics model calculating the instantaneous pressure in the displacement chambers and ports with the NSGA II (Deb, Pratap, Agarwal, &

Meyarivan, 2002), which is non-dominated sorting generic algorithm to optimize the valve plate design. Figure 1.4 shows the flowchart describing the VpOptim tool.

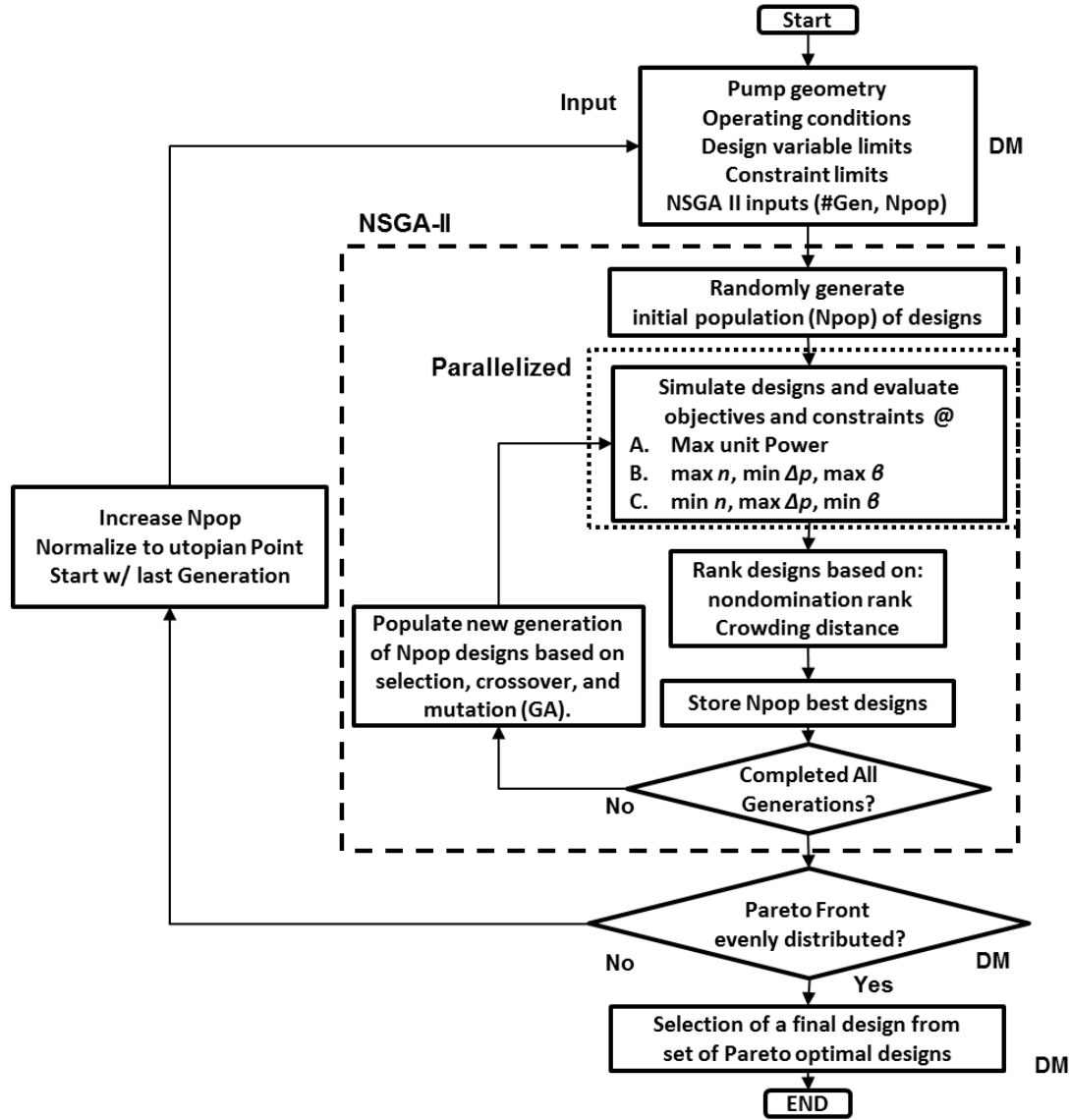


Figure 1.4. Valve plate optimization method (from Kalbfleisch, 2015)

Fundamental research was previously done on the lubricating interfaces, Berge (now Ivantysynova, 1983) solved for the non-isothermal flow in the piston cylinder interface without considering micro-motion of the piston. Fang and Shirakashi (1995) calculated the position of the piston within the cylinder bore in the cylinder block by considering the force balance on the piston. Kleist (1997) expanded the same approach to the rest of the lubricating interfaces. Manring (2000) investigated the effects that contribute to the tipping of the block. Wieczorek and Ivantysynova (2002)

developed CASPAR a non-isothermal fluid flow model which considers micro-motion and the force balance on all components for all three interfaces. CASPAR could predict the fluid film thickness assuming rigid bodies for all the solids involved in the lubricating gaps. Olems (2000) performed several measurements on the cylinder block next to the piston/cylinder lubricating interface and validated his numerical model. Huang and Ivantysynova (2003) expanded on Wieczorek's model by adding pressure deformation effects in the cylinder block/valve plate. Jouini and Ivantysynova (2008) introduced a heat transfer module to the Huang's extended version of the model and validated the model utilizing valve plate temperature measurements for several operating conditions. The valve plate temperature measurements matched the general trend but not in an accurate manner. The heat transfer module was present but no elastic deformations due to thermal loadings were considered.

Richardson et al. (2017) used a customized test rig for a swash plate type axial piston machine with a floating valve plate. Using this test rig, they measured the fluid film thickness and used these measurements to develop a model for the valve plate/cylinder block interface. Hashemi et al. (2016) developed a multi-dynamics model for the slipper/swash plate interface which also includes a mixed-lubrication model, using the authors' software Tribo-x. The model was validated through the creation of a special test rig in which the friction between the slipper and swash plate was measured by Hashemi et al. (2017).

Similarly, Pelosi (2012), Zecchi (2013) and Schenk (2014) developed novel fluid structure thermal interaction models able to predict more accurately the behavior of the fluid film for the piston/cylinder, cylinder block/valve plate and slipper/swash plate interface, respectively. The models include different modules capturing the various physical phenomena like micro-motion of the cylinder block, non-isothermal flow in the lubricating gap, and pressure and thermal elastic deformation on the solid bodies.

The elastic deformations of the solid bodies are solved utilizing an in-house developed FEM model. The numerical model needs sufficient surface boundaries to be constrained such that solid body motion is restricted. The constraints are of paramount importance for numerical reasons and to reproduce the real mechanical system as accurately as possible. The constraints impact the solid

bodies' deformations which would change the fluid film geometry in the lubricating interfaces. The fluid film geometry changes the solution of the non-isothermal flow through the lubricating interfaces. Two main methods were applied on the fluid structure thermal interaction models; zero Dirichlet constraint and inertia relief method. The Dirichlet constraint method constrains nodes to be fixed. The inertia relief method balances all the loads by inertial forces and moments in the form of an inertial acceleration field. The inertia relief method allows the solution of elastic deformations for components which are not physically constrained such as the piston in axial piston machines. (Pelosi & Ivantysynova, 2013)

The solid body elastic deformations not only change the fluid film geometry but they also introduce additional squeeze velocities into the source of the Reynolds equation. The micromotion of the rigid bodies was considered traditionally as the only source of squeeze effect. Schenk and Ivantysynova (2015) introduced the consideration of solid body deformations as a source for the squeeze effect in the solution of the Reynolds equation for the slipper and swash plate interface.

The three models were validated separately in special experiments utilizing dedicated test rigs for each lubricating interface. The piston/cylinder interface model was validated using two specially designed test rigs; one where the pressure and temperature fields have been measured in the fluid film, and a second one where the friction between the piston and the cylinder bore can be measured directly (Pelosi, 2012). The cylinder block valve plate/end case assembly was validated with temperature measurements on a commercial unit by installing thermocouples in the valve plate of a 130 cc axial piston machine (Zecchi, 2013). The slipper/swash plate interface model was validated by measuring the fluid film thickness between the slipper and swashplate by introducing minimal design changes to a commercial unit by installing six eddy current sensors on the swashplate (Schenk, 2014). These very sophisticated thermal fluid structure interaction models developed for these three main interfaces of swash plate type axial piston machines have been used to analyze existing stock units (Schenk, Zecchi, & Ivantysynova, 2013). This model still hasn't been utilized for creating new pump designs.

Ivantysyn (2011) worked on a framework for computational design of axial piston machines utilizing the extended version of CASPAR and the VpOptim developed by Seeniraj and

Ivantysynova (2008). Ivantysyn designed a new valve plate using the VpOptim algorithm. In his work, an analysis of the three lubricating interfaces was also performed where the sensitivity to the balance factor in the cylinder block/valve plate and slipper/swash plate interface was performed. The piston/cylinder interface clearance sensitivity was analyzed utilizing an analytical equation and assuming the piston to be centered in the cylinder bore. These were an initial step towards virtual prototyping but the models that were available at the time neglected many important physical effects impacting the fluid film behavior like micro motion, surface deformation due to pressure and thermal loading. Therefore, these models didn't allow a very reliable prediction of fluid film behavior and machine performance as needed for virtual prototyping. Schenk and Ivantysynova (2011) implemented an optimization for the slipper/swash plate interface using a surrogate model which is a response surface method, since it helps diminish the computational cost of the optimization. This optimization was performed on an existing commercial hydraulic unit but was never implemented.

Recent research has also been done in the prediction of case and outlet temperature in axial piston machine. The temperatures in the case and outlet port are important for the thermal boundary conditions utilized for the calculation of the non-isothermal flow in the lubricating interfaces. Shang and Ivantysynova (2015) developed a model that predicts the case and port flow temperature based on thermodynamics and heat transfer. This model allows the performance prediction of axial piston machines without measured thermal boundaries. This model has been validated by the comparison of simulations against measurement for different hydraulic units at different operating conditions with diverse types of fluids.

Shang and Ivantysynova (2017) investigated novel combinations of materials for the piston/cylinder lubricating interface. The piston's traditional design was modified by adding an aluminum fill inside of the piston, which adds a temperature adaptive capability for the piston through the thermal deflection at different operating conditions. The researchers found they could reduce overall energy dissipation for the piston/cylinder interface.

1.3 Aim of this Work

The aim of the work presented in this dissertation is to propose a new computational based methodology for virtual prototyping of swash plate type axial piston machine utilizing a combination of in-house developed multi-domain models and to demonstrate the feasibility of the proposed.

Virtual prototyping of swash plate type axial piston machines should replace the expensive and time-consuming heuristic design process currently used in industry which relies heavily on experiments. The focus of virtual prototyping process is the optimization of the following main parts of the swash plate type machines:

- Valve plate
- Cylinder block assembly
- Slipper/piston assembly
- Swash plate
- End case

1.4 Original Contributions of this work

The novel computational based methodology for virtual prototyping of swash plate type axial piston machine was presented in this dissertation together with the following:

- Novel valve plate optimization algorithm to consider four quadrants of operation for low noise and low control effort.
- Investigation of influence of end case design on the cylinder block/valve plate interface behavior.
- Investigation of influence of swash plate design on the slipper/swash plate interface behavior.
- Investigation of the influence of micro-surfacing on slippers.
- Novel algorithm for optimal design of cylinder block/valve plate interface using estimated case and port temperatures.
- Built and tested the first swash plate type axial piston machine based on a computational design methodology.

2. INTRODUCTION TO AXIAL PISTON MACHINES OF SWASH PLATE TYPE

As shown previously in the introduction chapter axial piston machines are made by the following main components: cylinder block, piston/slipper assembly, valve plate, swashplate, and shaft. This chapter will detail the inner workings of the machine from a mathematical formulation.

2.1 Kinematics of Axial Piston Machines of Swashplate Type

In the following section the main parameters derived from the machine kinematics of swashplate type axial piston machines are described. The cross section of the machine can be seen in Figure 2.1 with the main coordinate system used to determine the machine's kinematics.

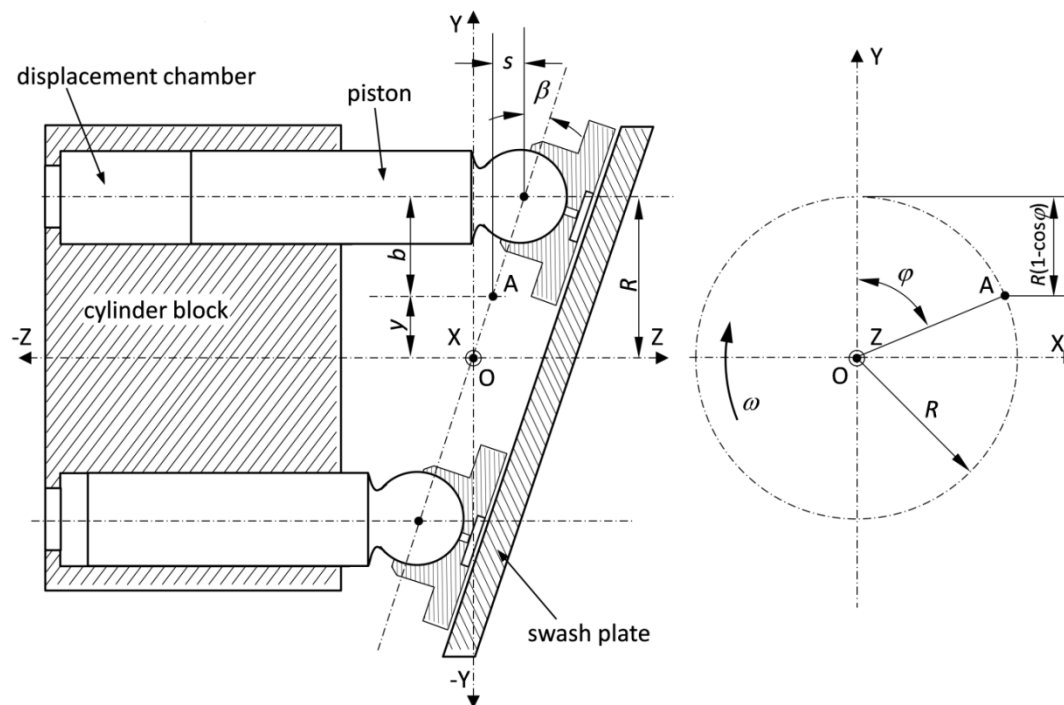


Figure 2.1. Schematic of an Axial Piston Machine (Seeniraj & Ivantysynova, 2009).

The point O, references the origin of the coordinate system, it is determined by the intersection of the shaft axis and the plane parallel to the running surface of the swashplate, which intersects the centers of the ball joints between the slipper and piston.

This position of the piston is indicated with the variable S_K , along the z-axis can be defined as (J. Ivantysyn & Ivantysynova, 2001):

$$S_K = -z. \quad (2.1)$$

From Figure 2.1 follows:

$$z = b \cdot \tan \beta. \quad (2.2)$$

And
$$b = R - y. \quad (2.3)$$

Where
$$y = R \cdot \cos \varphi. \quad (2.4)$$

$$S_K = -R \cdot \tan \beta (1 - \cos \varphi). \quad (2.5)$$

$$H_K = 2 \cdot R \cdot \tan \beta. \quad (2.6)$$

The piston velocity and acceleration are defined as:

$$v_K = -\omega \cdot R \cdot \tan \beta \cdot \sin \varphi. \quad (2.7)$$

$$a_K = -\omega^2 \cdot \tan \beta \cdot \cos \varphi. \quad (2.8)$$

The geometric displacement:

$$V_g = z \cdot A_K \cdot H_K = z \cdot \frac{\pi \cdot d_K^2}{2} \cdot R \cdot \tan \beta. \quad (2.9)$$

For the nominal flow:

$$Q_g = n \cdot z \cdot A_K \cdot H_K. \quad (2.10)$$

For a more complete derivation of the axial piston machine dynamics please refer to Ivantysyn and Ivantysynova (2001).

2.2 The Function of the Lubricating Interfaces

The lubricating gaps are the most critical design elements in the design of axial piston machines of swashplate and bent axis type, shown in Figure 2.2. These lubricating interfaces must fulfill two main functions; bearing the external loads and sealing the pressurized fluid. The interface requires a sufficiently stable fluid film to bear the loads, and a thin fluid film to seal efficiently the pressurized fluid. Additionally, they represent the main sources of energy dissipation of the machine. This energy dissipation is composed by two sources; the leakage flow through the interface towards the case volume and the viscous friction in the fluid. To minimize energy

dissipation these losses have opposite requirements. To reduce leakage flow, a low fluid film is desired, whereas to minimize viscous friction a thicker fluid film is preferred.

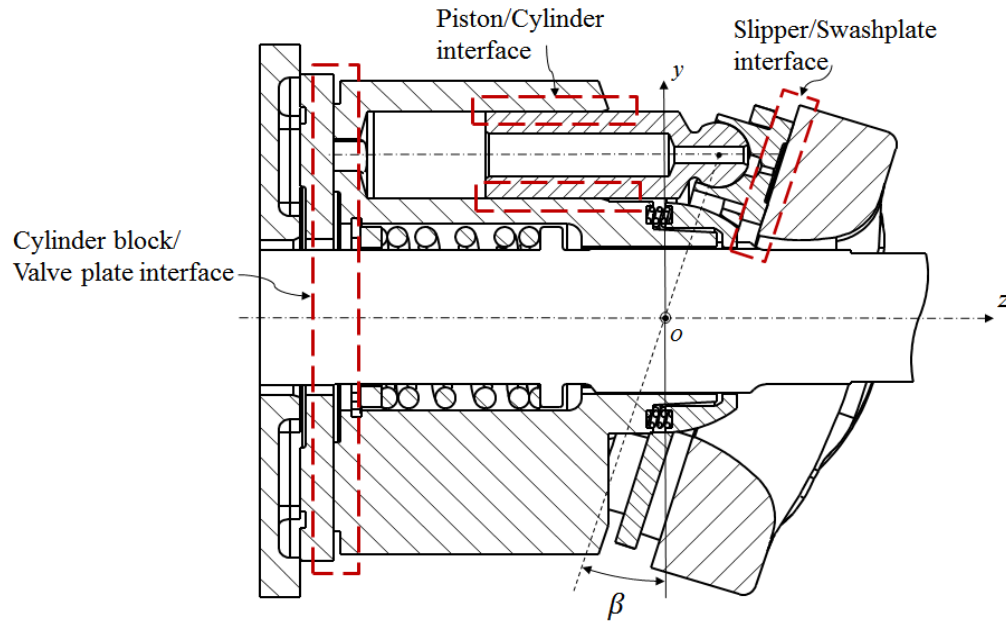


Figure 2.2. Axial Piston Machine Swash Plate Type Cross-section.

2.3 External Loads on the Rotating Group

The loads exerted on the rotating group are of extreme importance to the calculation of the fluid film geometry in the lubricating interfaces. The main external load applied on all the components derive from the pressure in the displacement chambers. These loads are described in this section affecting the three main lubricating interfaces.

The external forces exerted on the cylinder block are described in this section; and, they are shown in Figure 2.3. The cylinder is loaded simultaneously by all the pistons.

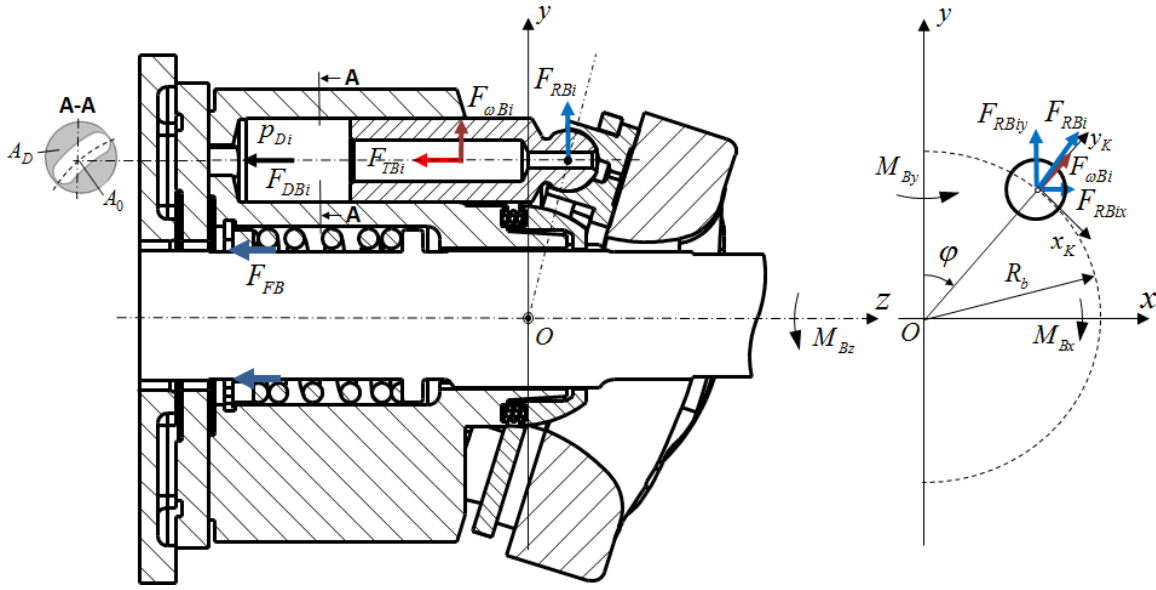


Figure 2.3. Cylinder Block Free Body Diagram.

The main force applied on the cylinder block is due to the pressurized fluid in the displacement chamber. The pressure force F_{DB} , depends on the displacement chamber pressure p_{Di} and surface area A_D , which is defined by the piston diameter d_K and displacement chamber opening area A_0 .

$$F_{DB} = -p_{Di} \cdot A_D. \quad (2.11)$$

$$A_D = d_K^2 \frac{\pi}{4} - A_0. \quad (2.12)$$

Second, the spring force F_{FB} pushes the cylinder block in direction of the valve plate, on the z -axis,. The spring is placed between the cylinder bore and the shaft in order to prevent the block from tipping when running at high speed and very low pressure. Third, the force due to the friction F_{TB} between the piston and the cylinder bore in the piston/cylinder interface. This force is calculated using a comprehensive fluid structure interaction model for the piston/cylinder interface predicting the fluid film and therefore also the viscous friction. Furthermore, the force due to the centripetal acceleration of the piston/slipper assembly, $F_{\omega B}$, acts in the radial direction of the cylinder block, defined as:

$$F_{\omega Bi} = m_K \omega^2 R_B. \quad (2.13)$$

The forces acting on the piston/slipper assembly are shown in Figure 2.4.

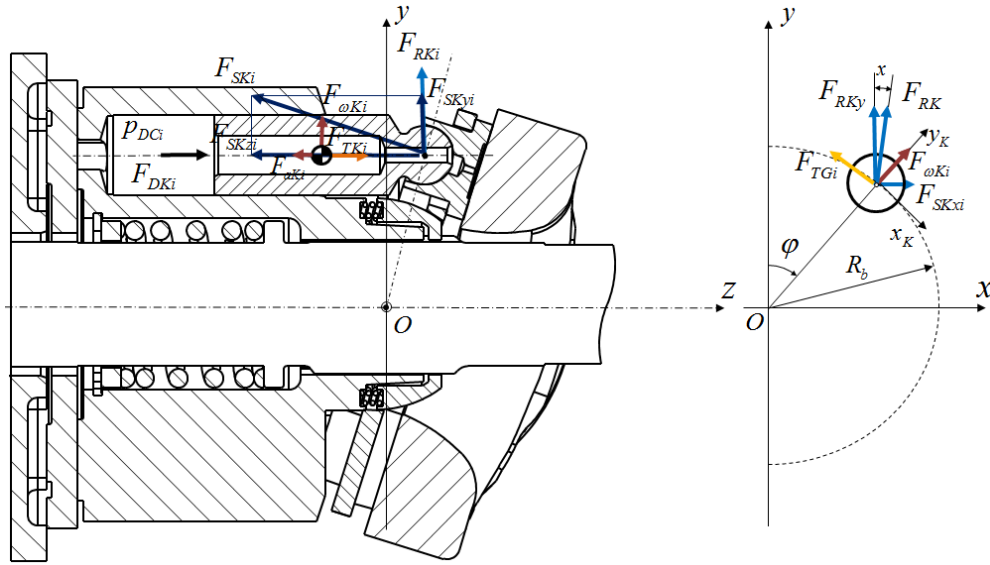


Figure 2.4. Piston/Slipper Assembly Free Body Diagram.

The main force acting on the piston/slipper assembly is due to the pressurized fluid in the displacement chamber, F_{DK} , pushes the bottom of the piston in direction of the swashplate. The force due to the inertia of the piston/slipper assembly acts on the z -axis, F_{aK} ; and finally the force due to the friction between the piston and the cylinder bore also acts in the z -axis, F_{TK} . This last force, F_{TK} , has the same magnitude as F_{TB} but has opposite sign. The total sum of these forces, F_{DK} , F_{aK} , and F_{TK} , has to be reacted by the swashplate. Finally, the reaction force F_{SK} of the swashplate is acting on the piston/slipper assembly. More forces have an impact on the piston/slipper assembly; such as: the viscous friction between the slipper and swashplate on the local x_K direction as shown in Figure 2.4, F_{TG} ; and the body force due to centripetal acceleration, $F_{\omega K}$. The latter force is the same force as the one represented in the Figure 2.3 by $F_{\omega B}$. The forces related to the piston/slipper assembly are all transmitted to the block summed into a resultant side force, F_{RK} , which is the same force represented for a single piston on Figure 2.3 as F_{RBi} . This force is calculated as follows:

$$F_{RBxi} = F_{\omega Ki} \sin \varphi - F_{TG_i} \cos \varphi. \quad (2.14)$$

$$F_{RBxi} = F_{SK_i} + F_{\omega Ki} \cos \varphi + F_{TG_i} \sin \varphi. \quad (2.15)$$

The resulting forces and moments on the cylinder block can be expressed as follows:

$$F_{BZ} = F_{FB} + \sum_{i=1}^Z F_{DBi} + \sum_{i=1}^Z F_{TBzi}. \quad (2.16)$$

$$M_{Bx} = \sum_{i=1}^Z y_i F_{DBi} + \sum_{i=1}^Z y_i F_{TBzi} - \sum_{i=1}^Z z_i F_{RByi}. \quad (2.17)$$

$$M_{By} = - \sum_{i=1}^Z x_i F_{DBi} - \sum_{i=1}^Z x_i F_{TBzi} + \sum_{i=1}^Z z_i F_{RBxi}. \quad (2.18)$$

The external forces and moments Eq. (2.16), (2.17), and (2.18) need to be balanced by the forces and moments generated by the fluid film pressure field:

$$F_{fB} = \int_{SCB} p \, da. \quad (2.19)$$

$$F_{fx} = \int_{SCB} py \, da. \quad (2.20)$$

$$F_{fy} = - \int_{SCB} px \, da. \quad (2.21)$$

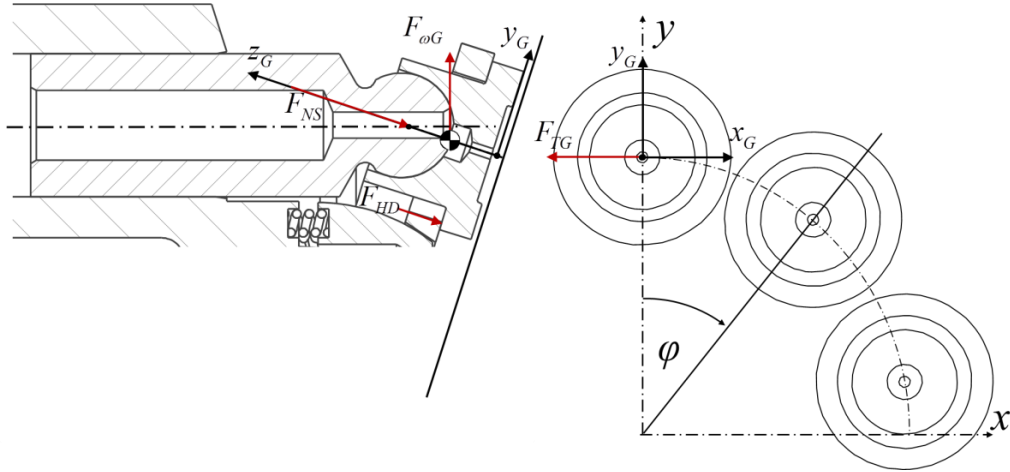


Figure 2.5. Free Body Diagram of the Slipper Forces.

The external loads on the slipper can be explained using Figure 2.5. The main force F_{NS} , known as the clamping force, derives from the combination of forces acting on the piston/slipper assembly. It is the same as F_{SK} but acts in opposite direction. The hold down force depends on the type of

slipper hold down system. Two main types are utilized fixed and positive hold down systems. The first, the fixed hold down allows the slipper to translate in its z -axis for a maximum clearance between slipper and swashplate. Once the maximum clearance has been reached the hold down system imposes a force on the slipper to constrain its movement. The second, the positive hold down system utilizes a spring which constantly pushes on a plate pushing the slippers against the swash plate. The force due to the centrifugal effect acts on the center of mass of the slipper. Finally, there is a force between the slipper and swash plate due to viscous friction F_{TG} .

2.4 Lubricating Interfaces Geometry

For the analysis of the performance of the fluid film in the three lubricating interfaces is important to define their corresponding geometries and local coordinate systems. Each lubricating interface is different in nature and requires its own coordinate system.

2.4.1 Cylinder Block/Valve plate Interface

The cylinder block/valve plate is composed of a rotating and a stationary part. The rotating part is the cylinder block, which besides being able to rotate together with the shaft it can also translate in the z -axis and tilt in the x and y -axis direction. The valve plate is static at any moment in time. In the case of a rigid model, i.e. without consideration of solid bodies thermal and pressure deformation, the fluid film geometry is described solely by the relative position of the cylinder block with respect to the valve plate.

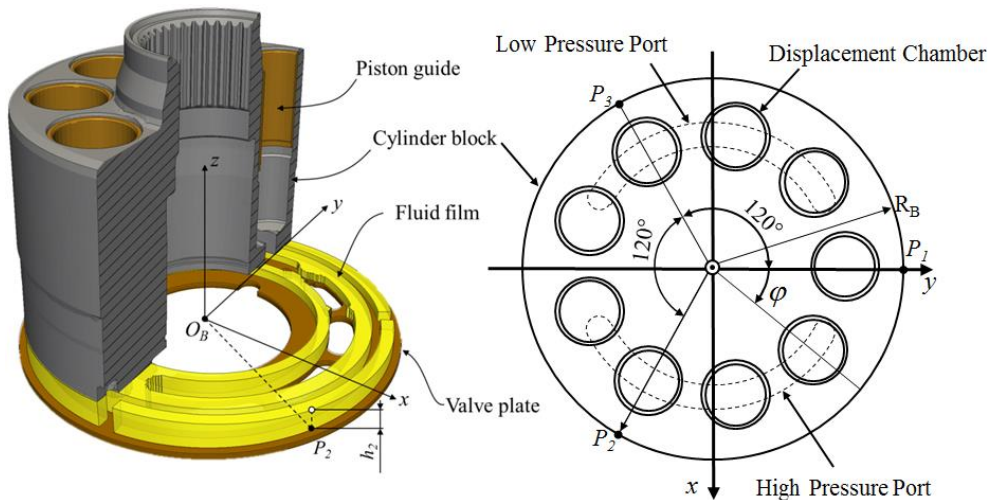


Figure 2.6. Cylinder block/valve plate interface schematic

This is represented in Figure 2.6, where the local coordinate system's origin, O_B , is in the intersection of the valve plate's running surface plane and the shaft axis, with the z-axis pointing towards the swashplate and the y-axis is pointing in the direction of the outer dead center of the machine, the x-axis is pointed towards the high-pressure port of the machine. The fluid film geometry can be described in any point P by the position of the cylinder block with three control points P1, P2, and P3, with respect to the valve plate surface (plane $z=0$). The geometry can be described as expressed by Eq. (2.20) as in Wieczorek and Ivantysynova (2002).

$$h(r, h) = \frac{1}{\sqrt{3}R_B} r \sin \varphi (h_{P2} - h_{P3}) + \frac{1}{3R_B} r \cos \varphi (2h_{P1} - h_{P2} - h_{P3}) + \frac{1}{3} (h_{P1} + h_{P2} + h_{P3}). \quad (2.22)$$

Additional to the cylinder block being able to move relative to the valve plate, both solid bodies can deform elastically due to pressure and thermal effects. In case of considering, surface deformation due to pressure and thermal loading, as well as surface shaping (2.22) need to be modified in order to determine the film geometry. The fluid film thickness at any point can be expressed see (Zecchi and Ivantysynova, 2013):

$$h(r, h) = \frac{1}{\sqrt{3}R_B} r \sin \varphi (h_{P2} - h_{P3}) + \frac{1}{3R_B} r \cos \varphi (2h_{P1} - h_{P2} - h_{P3}) + \frac{1}{3} (h_{P1} + h_{P2} + h_{P3}) + (\delta h_{CB}(r, \varphi) - \delta h_{VP}(r, \varphi)). \quad (2.23)$$

2.4.2 Slipper/Swash Plate Interface

The slipper swash/plate interface is composed of the slipper and the swash plate. The slipper slides on top of the swash plate which is stationary. The slipper rotates around the shaft axis and it translates together with the pistons. The slipper rotates about its own origin and tilts about the x and y axis. The slipper's local coordinate system is shown in Figure 2.7 on the right. The fluid film geometry is described in an equivalent manner as the cylinder block/valve plate interface fluid film geometry in the previous section. The fluid film geometry is described using the height at three control points at the outer radius of the slipper:

$$\begin{aligned}
h(r, \varphi) = & \frac{1}{\sqrt{3}r_{outG}} r \cdot \sin \varphi (h_{P2} - h_{P3}) \\
& + \frac{1}{3r_{outG}} r \cdot \cos \varphi (2h_{P1} - h_{P2} - h_{P3}) \\
& + \frac{1}{3} (h_{P1} + h_{P2} + h_{P3}) + (\delta h_{SL}(r, \varphi) - \delta h_{SW}(r, \varphi)).
\end{aligned} \tag{2.24}$$

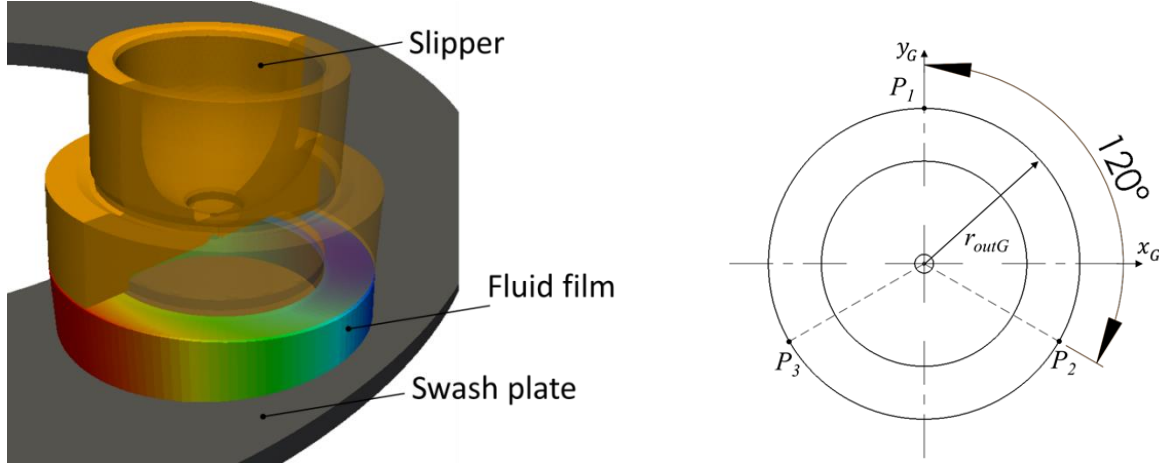


Figure 2.7. Slipper/swash plate representation.

2.4.3 Piston/Cylinder Interface

The piston/cylinder interface fluid film geometry can be described utilizing two control points on the end of the piston guide length (gap length). These control points move with the gap when the gap length is varying as the piston moves in and out of the cylinder bore.

First, a description of the piston position is needed. Because the micro-motion of the piston within the cylinder bore is critical to the buildup of hydrodynamic pressure, the precise position must be well defined. Figure 2.8 shows the convention for defining the piston position. As with any body free to move in three-dimensional space, the piston has 6 degrees of freedom in which it can move; three rotational directions and three translational directions. Position along and rotation about the z_K axis is defined by the kinematics of the pump and the simulation inputs, respectively. This leaves four degrees of freedom to be calculated during the simulation based on a force balance between the external forces and the pressure field generated in the lubricating gap. The position

of these four degrees of freedom is defined by four scalar quantities $\{e_1, e_2, e_3, e_4\}$. Figure 2.8 shows the convention for defining these positions. First, a plane is defined at either end of the guide length. Here, section A-A lies on the plane at the end of the guide length nearest to the swash plate, and section B-B lies on the plane at the end of the guide length nearest to the displacement chamber. In the B-B section, value e_1 defines the distance between the axes of piston and cylinder in the x_K direction, while e_2 defines the distance between the axes in the y_K direction. Similarly, in the A-A section, e_3 and e_4 define the distance between the axes in the y_K and x_K directions, respectively. The four values are combined into an eccentricity vector $\{e_1, e_2, e_3, e_4\}$. Rigid film thickness is calculated from the eccentricity vector at each point in the gap. Surface deformations as described in section 3.3.6 are then applied to this rigid height to arrive at the instantaneous film thickness for each location.

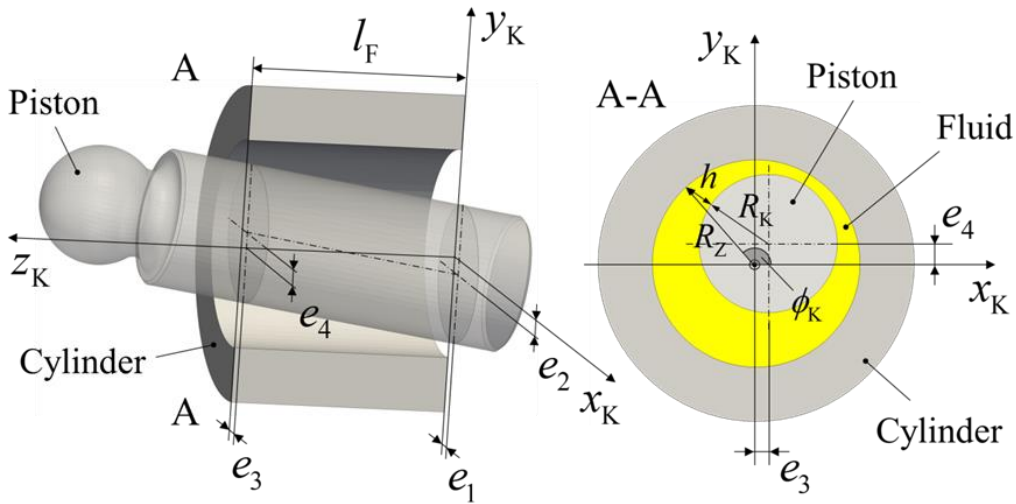


Figure 2.8. Piston/cylinder interface control points.

3. NUMERICAL MODELS FOR VIRTUAL PROTOTYPING

In this chapter, the coupled multi-domain axial piston machine model used to for virtual prototyping of axial piston machines will be described in detail. The coupled multi-domain model is divided in three modules, as shown in Figure 3.1.. The three modules share inputs and outputs between each other. The first is the pressure module which utilizes a lumped parameter approach to calculate the instantaneous pressure in the displacement chamber. The pressure module can also calculate the effective outlet flow due to compressibility and internal losses, as well as port pressures, and moments applied on the swash plate. The pressure module can make use of information calculated from both the thermo-elastohydrodynamic models such as leakage flows through the gaps and temperature values for the outlet and case from the thermal model to update properties on the displacement chamber's pressure calculation. The second module is the thermo-elastohydrodynamic model, it splits into three separate modules one per interface (piston/cylinder, cylinder block/valve plate, and slipper/swash plate interface). The thermo-elastohydrodynamic model predicts the fluid film's behavior in each lubricating interface. It considers the non-isothermal fluid flow through the lubricating interfaces by solving the Reynolds and energy equations. It also considers additional physical phenomena such as elastic deformations due to pressure and thermal effects. Similarly, the thermo-elastohydrodynamic model can use the updated discharge port and case flow temperatures and the instantaneous pressure profile in the displacement chamber, both would change the boundary conditions imposed on the non-isothermal gap module. Finally, the thermal model predicts the discharge port and case flow temperatures based on the thermodynamic and heat transfer characteristics of the machine. The heat transfer part considers the energy dissipated in the lubricating interfaces and the leakage flow through the lubricating interfaces.

As mentioned previously, the three modules can provide and receive information from each other. The most accurate prediction of the axial piston machine performance is achieved by using the three modules in an iterative process until convergence is achieved. The thermal model is used to update the discharge port and case flow temperatures based on the energy dissipation calculated in the lubricating interface with the thermo-elastohydrodynamic model which are needed as inputs for the thermo-elastohydrodynamic model. The thermo-elastohydrodynamic model use updated

energy dissipation from the lubricating interfaces and flow calculation from the axial piston machine.

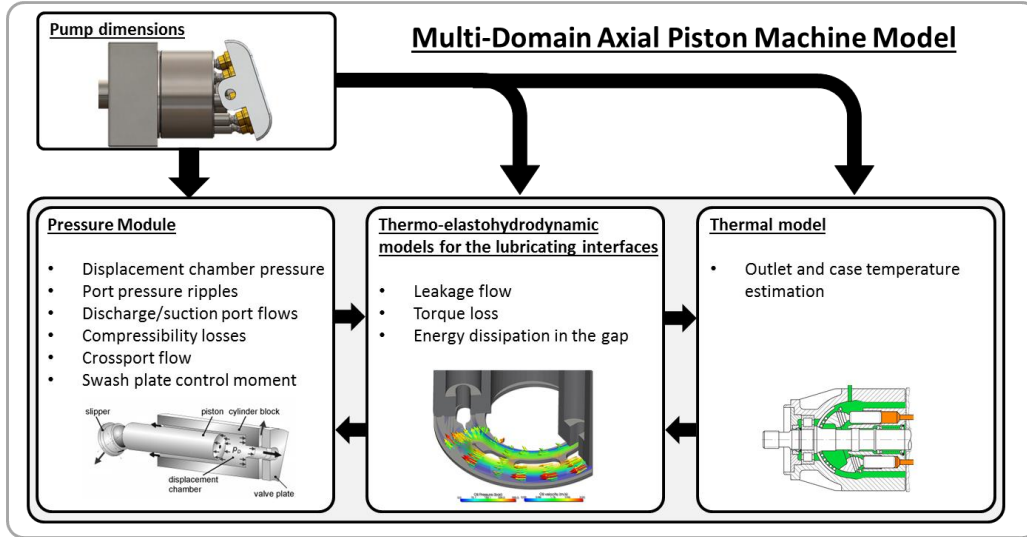


Figure 3.1. Multi-domain axial piston machine model.

3.1 Pressure Module

The instantaneous pressure in the displacement chamber is an essential parameter for the correct calculation of the external forces exerted on the piston\slipper assembly, swash plate, cylinder block, and the valve plate/end case assembly. The instantaneous pressure in the displacement chamber changes continuously over one shaft revolution and it's therefore a function of time; nevertheless, it can be assumed that the pressure is uniform in the entire displacement chamber. A lumped parameter approach can be applied.

The pressure build-up equation can be written as:

$$\frac{dp_{DCi}}{dt} = \frac{K}{V_i} \left(Q_{ri} + Q_{SKi} + Q_{SBi} + Q_{SGi} - \frac{dV}{dt} \right) \quad (3.1)$$

And the orifice equation:

$$Q_{ri} = \alpha \cdot A_r \cdot \sqrt{\frac{2 \cdot \Delta p}{\rho}} \quad (3.2)$$

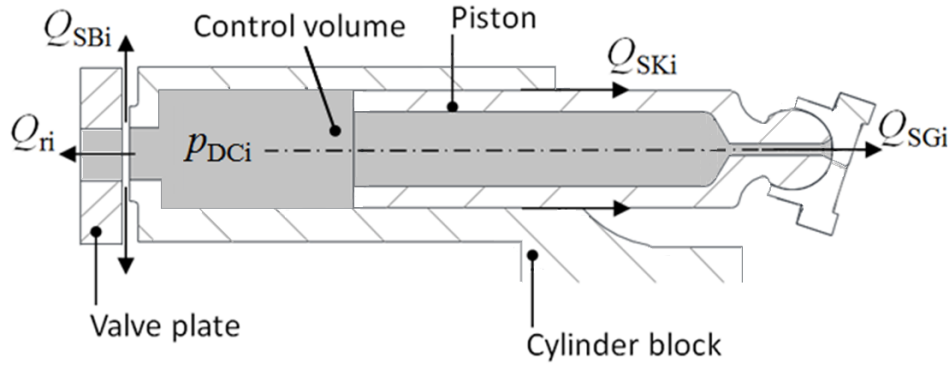


Figure 3.2. Instantaneous Pressure Calculation Control Volume.

In Eq.(3.1), the left-hand side is the derivative of the pressure over time, on the right hand side K is the bulk modulus, V is the fluid volume and dV/dt is its derivative over time; the various Q terms are the flow in and out of the volume, as illustrated in Figure 3.2. Each flow is by convention positive when it enters in the control volume, since this would force the pressure to increase. The flow Q_{ri} is the flow from the low-pressure port to the control volume and from the control volume to the high-pressure port. The other flows labeled with Q_s are the corresponding leakages through the three lubricating gaps: the flow through the slipper/swashplate interface, Q_{SGi} ; the flow through the piston/cylinder interface, Q_{SKi} ; and finally, the flow through the cylinder block/valve plate interface, Q_{SBi} .

More information about the lumped parameter approach to calculate p_{DCi} can be found in previous work done by Wieczorek and Ivantysynova (2002), Seeniraj and Ivantysynova (2008), and Klop (2010). It is important to understand that the result of the calculation (in term of pressure fluctuations) is remarkably affected by the volumes of the low and high pressure ports. Those volumes depend on the system where the unit is mounted in; however, to generate these results no additional lines were considered and the volume of the ports was calculated by measuring the volume of fluid enclosed in the pump from the valve plate openings to the pump inlet and outlet ports. The result is also strongly affected by the fluid properties, bulk modulus in particular.

The instantaneous pressure in each displacement chamber allows the calculation of the following:

- Swash plate moments
- Flow and pressure ripple

- Volumetric efficiency (due to internal leakage and compressibility)

- **Swash Plate Moments**

The total external loads on the swash plate can be calculated using the instantaneous pressure in the displacement, operating speed, and mass of the piston/slipper assembly. The total force applied on each piston considers the force due to the pressure in the displacement chamber F_{DK} , the force due to the inertia of the piston/slipper assembly F_{aK} , and the friction force between the piston and the cylinder bore F_{TK} . The sum of these three forces yield the total force acting on the piston/slipper assembly. This force is utilized to calculate the total force on the swashplate and the moments:

$$F_{DK} = A_K \cdot (p - p_e) = \frac{\pi \cdot d_K^2}{4} \cdot (p - p_e) \quad (3.3)$$

$$F_{aK} = -m_K \cdot a_K = m_K \cdot \omega^2 \cdot R \cdot \tan \beta \cos \varphi \quad (3.4)$$

$$F_{AK} = F_{DK} + F_{aK} + F_{TK} \quad (3.5)$$

The moments on the swashplate are calculated

$$M_{SX} = \frac{R}{\cos^2 \beta} \sum_{i=1}^z F_{AKi} \cos \varphi_i \quad (3.6)$$

$$M_{SY} = R \sum_{i=1}^z F_{AKi} \sin \varphi_i \quad (3.7)$$

$$M_{SZ} = -R \tan \beta \sum_{i=1}^z F_{AKi} \sin \varphi_i \quad (3.8)$$

- **Flow ripple**

The flow ripple is the pulsation in the volumetric flow on both the inlet and the outlet ports. The flow ripple is calculated by calculating the peak to peak value of the flow.

3.2 Thermal model to predict port and case fluid temperatures

The port and case fluid temperatures are crucial for the correct definition of the boundary conditions for the piston/cylinder, slipper/swash plate, and cylinder block/valve plate interfaces, as well as the boundary conditions for the pressure module modifying the fluid properties due to temperature. The thermo-elastohydrodynamic numerical models are very sensitive to the port and case flow temperatures. Shang and Ivantysynova (2015) proposed a lumped parameter to predict the temperatures in the pump/motor ports and case. Figure 3.3 shows the control volumes considered by the model. The heat transfer module has been simplified to consider only a three-volume model between the displacement chamber fluid volume, case fluid volume and the solid parts. The figure also shows the crucial fluid flows in and out of the displacement chamber volume, the first two are the inlet (\dot{m}_{in}) and the outlet flow (\dot{m}_{out}), and the third is the flow from the displacement chamber into the case fluid volume ($\dot{m}_{l,e}$). The fluid flow from the displacement chamber into the case fluid volume is critical to maintain a controlled temperature in the case fluid volume. Figure 3.3 shows the p_{in} and p_{out} which contribute to the temperature variation through adiabatic compression and expansion of the fluid in the displacement chamber. The red arrows represent the convection considered between the different control volumes. Figure 3.3 shows the convection relation between the displacement chamber and the solid parts, the solid part and the case fluid volume, and the housing solid body and the ambient. Finally, Figure 3.3 also represents the heat flux coming from the energy dissipation in the three lubricating interfaces into the solid parts.

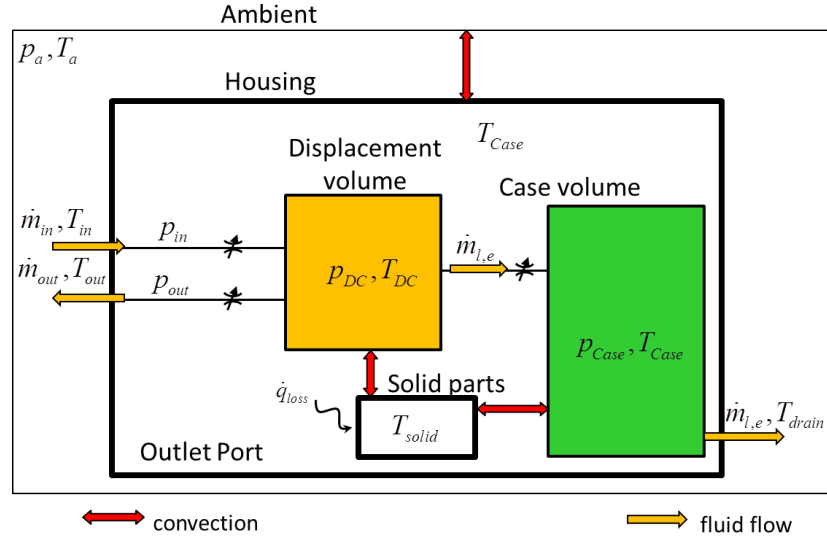


Figure 3.3. Simplified heat and mass transfer in the axial piston machine port and case flow temperature prediction model (Shang & Ivantysynova, 2015).

The temperature prediction model is shown in Figure 3.4 divided into two modules; the thermodynamic and the heat transfer modules. First, the thermodynamic module calculates the temperature change in the displacement chamber and case control volumes due to adiabatic compression and expansion of the fluid. Afterwards, the heat transfer module solves the convective heat-transfer between the control volumes described previously in Figure 3.3. The model checks for convergence between iterations, if there is no change in the discharge port and case volume temperatures the simulation is considered to have converged to a stable solution.

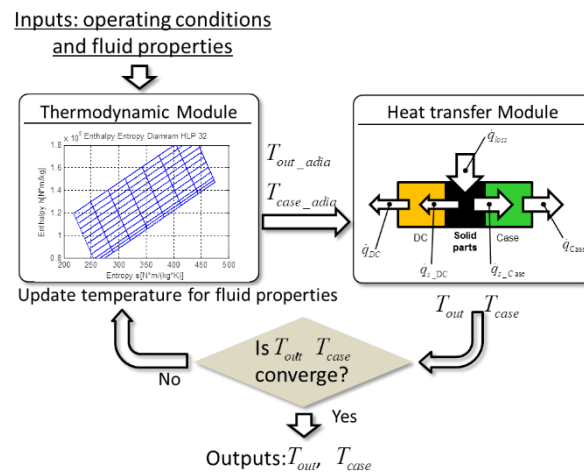


Figure 3.4. Port and case flow temperature prediction model scheme (Shang & Ivantysynova, 2015).

3.3 Thermo-Elastohydrodynamic Model

The numerical model utilized to predict the behavior of the fluid film is an advanced thermo-elastohydrodynamic model (TEHD) specifically developed by previous Maha researchers (Pelosi, 2012; Zecchi, 2013; and Schenk, 2014) for the prediction of the behavior of each lubricating interface (piston/cylinder, cylinder block/valve plate, and slipper/swashplate). The thermo-elastohydrodynamic models developed for the three main lubricating interfaces of swash plate type machines are composed out of similar sub models, i.e. the structure of the models is similar in nature therefore in the interest of keeping this chapter within the scope of the dissertation the cylinder block/valve plate interface developed by Zecchi (2013) will be described as an example. The models assume full fluid film lubrication in the lubricating interface. The model accounts for the machine kinematics, deformation of surfaces of the solids due to pressure and thermal loading, and micro-motion of the parts. The models calculate the fluid film behavior including energy dissipation. The models are composed of four main modules as shown in Figure 3.5. The first one and most important is the gap flow module, where the Reynolds and the energy equation are solved. In this module, a finite volume method approach is used to solve a non-isothermal fluid flow which is governed by both the Reynolds and the Energy equations. This module calculates the fluid film height, pressure, and temperature fields in the lubricating fluid film. These parameters are crucial for the correct prediction of the performance of the cylinder block/valve plate interface.

Second, an in-house linear FEM module that solves for the elastic deformation due to the pressure field in the lubricating gap. Third, a finite volume module that solves for the temperature distribution in the 3D volume of the solids. Finally, another FEM module solves for the elastic deformation due to the thermal stresses.

The Reynolds equation is solved to calculate the pressure field in the gap. The Reynolds equation which was first derived in 1886 by Osborne Reynolds from two main equations: the Navier-Stokes equation and the Continuity equation. The Reynolds equation had to be modified to accommodate for non-rigid surfaces for the cylinder block/valve plate by Zecchi and Ivantysynova (2013), slipper/swash plate interface Schenk and Ivantysynova (2015) and the Piston/Cylinder interface (Pelosi, 2012):

The Reynolds equation used in the cylinder block/valve plate interface is the following equation:

$$\frac{1}{r} \frac{\partial}{\partial r} \left(-\frac{\rho h^3}{12\mu} r \frac{\partial p}{\partial r} \right) + \frac{1}{r} \frac{\partial}{\partial \varphi} \left(-\frac{\rho h^3}{12\mu} r \frac{\partial p}{\partial \varphi} \right) = \omega \left(\rho \frac{\partial h_{CB}}{\partial \varphi} - \frac{1}{2} \frac{\partial(\rho h)}{\partial \varphi} \right) - \rho \frac{\partial h}{\partial t} \quad (3.9)$$

The left-hand side of the equation is the hydrostatic component of the diffusion from the boundaries. The right-hand side of the equation is the source in the Reynolds equation which includes the physical wedge, the translational squeeze and the normal squeeze component.

The energy equation is solved to obtain the temperature distribution of the fluid film between the cylinder block and the valve plate; the temperature determines the fluid physical properties; i.e. density, viscosity, bulk modulus, etc. Additionally, the energy equation defines the heat flux that is transmitted to the solid bodies from the fluid film.

The energy equation can be expressed as follows :

$$\nabla \cdot \left(\rho \nabla T - \frac{\lambda}{c_p} \nabla T \right) = \frac{\mu}{c_p} \Phi_d \quad (3.10)$$

The Eq. (3.10) contains the source term Φ_d , which is the mechanical dissipation function. It expresses the heat power generated per volume unit due to the viscous shear of the fluid in the thin fluid film. It is assumed that all the work to change the fluid element shape at constant volume is all converted to heat. Both pressure and temperature have an impact in the fluid properties due to the high dependence to the pressure and temperature. These are used to update the fluid properties in the gap. The pressure field is fed into another module, an in-house linear FEM module, which using the linear superimposition principle using influence matrixes calculates for the elastic deformation due to pressure in the gap. The deflection of the bodies is then fed back into the gap flow module to update the fluid film geometry; this is done with every angle of rotation. Additionally, the heat flux calculated every degree step, in the gap module, is then used in the finite volume module to calculate the temperature in the solid bodies every revolution. Furthermore, this temperature is then used to calculate the thermal stresses in the body. These are then fed to a second FEM module to calculate the elastic deformations due to thermal effects. The

elastic deformations due to thermal effects are fed back into the gap flow module to update the geometry of the fluid film. This process repeats until a steady state convergence is achieved. A general overview of the structure of the model is illustrated in the Figure 3.5:

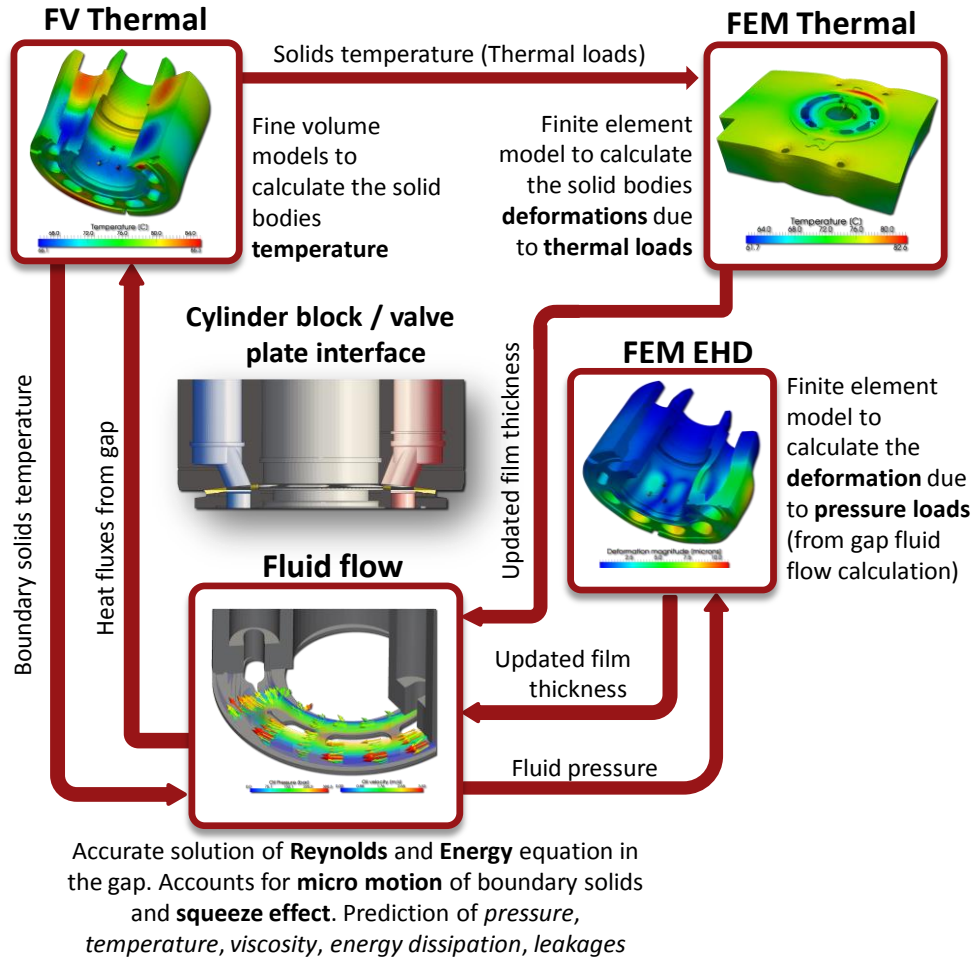


Figure 3.5. Fluid structure thermal interaction model example cylinder block/valve plate interface (Zecchi, 2013).

The model shown in Figure 3.5 allows the calculation of the energy dissipation taking place in the fluid film of the interface.

$$P_l = \int_v \Phi_d dv \quad (3.11)$$

Eq. (3.11) also includes the power loss due to leakage flow. The mechanical energy in the pressurized fluid is dissipated into heat, when it leaks through the gap. The leakage flow can be calculated by integrating the velocity field of the film at the lateral boundaries.

The power loss related to the leakage can be calculated, as shown in

$$P_{l,s} = Q_s \Delta p \quad (3.12)$$

The mechanical loss can be calculated as the difference of the total power dissipated Eq.(3.11) and the leakage loss Eq. (3.12).

3.3.1 Grid Generation and Boundary Conditions

This section explains the grid generation and boundary conditions for the thermo-elastohydrodynamic model of each lubricating interface. The numerical models specific grid generation vary depending on the lubricating interface's geometrical and functional features.

Two main types of meshes are used in the numerical models: the fluid mesh, used to solve the Reynolds and energy equation in the gap; and the solid mesh, used to calculate the temperature distribution of the bodies and to generate the influence matrices.

The solid mesh also represents an important input to the numerical model. It is used to generate the influence matrices which are then used to calculate online the deformation due to pressure; and also, used to calculate the temperature in the solid bodies.

3.3.2 Cylinder Block/Valve Plate Interface

In this section, the boundary conditions that are required for the non-isothermal flow which solves the Reynolds and energy equations in the lubricating gap, pressure and thermal analysis of the cylinder block and the valve plate and end case assembly are discussed.

The fluid film computational domain to calculate the non-isothermal fluid flow is discretized utilizing a structured three-dimensional mesh. The energy equation is solved utilizing this fluid mesh. A similar two-dimensional mesh is utilized for the solution of the Reynolds equation.

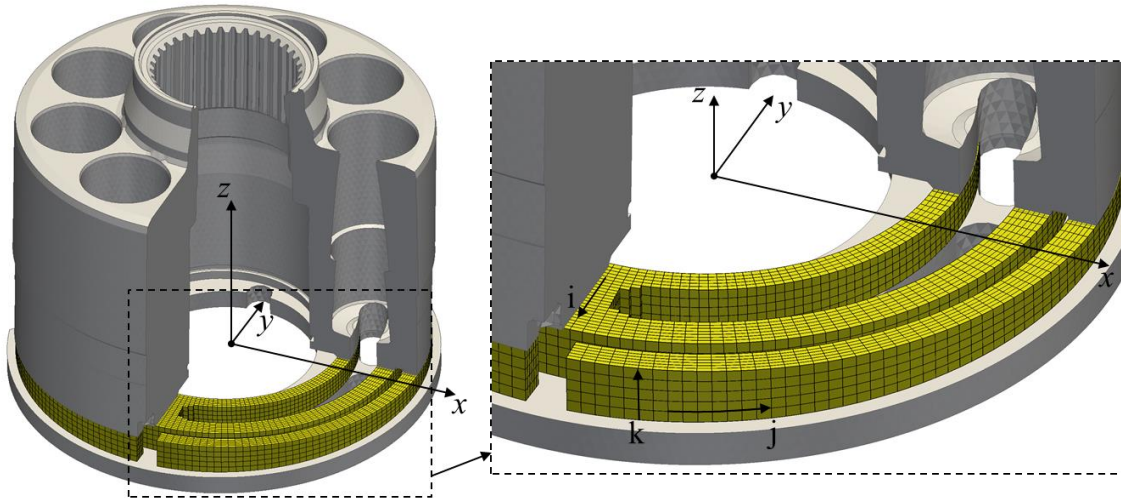


Figure 3.6. Structure grid used to solve the fluid flow (Zecchi, 2013).

The boundary conditions for the solution of the Reynolds equation are shown in Figure 3.7. The pressure boundary is set on the opening edges of the lubricating interface fluid mesh dependent on the whether the edge is overlapping with the high-pressure port or the low-pressure port. The outer edges of the lubricating interface are much simpler since these will see case pressure.

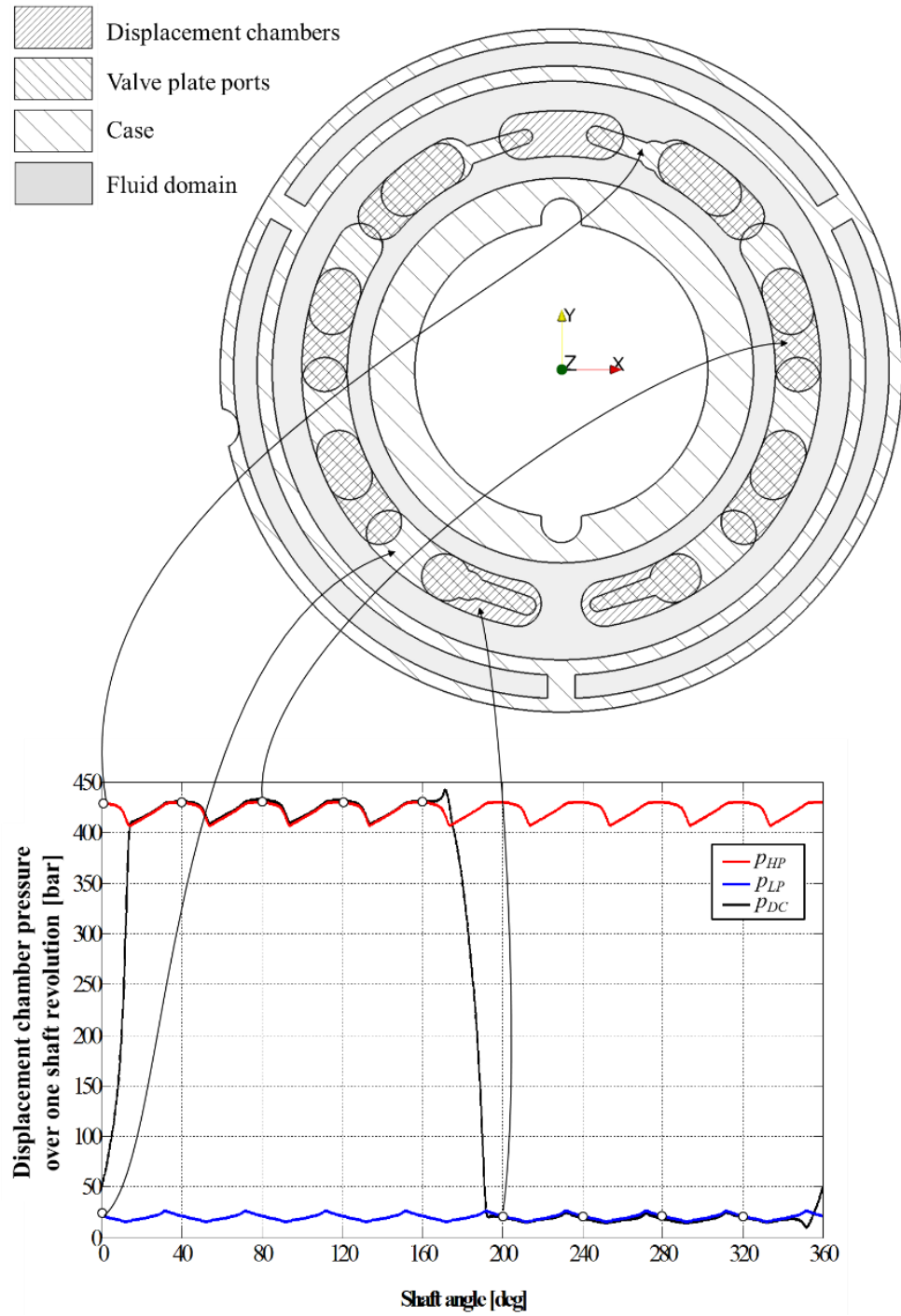


Figure 3.7. Boundary conditions for the solution of the Reynolds equation (Zecchi, 2013).

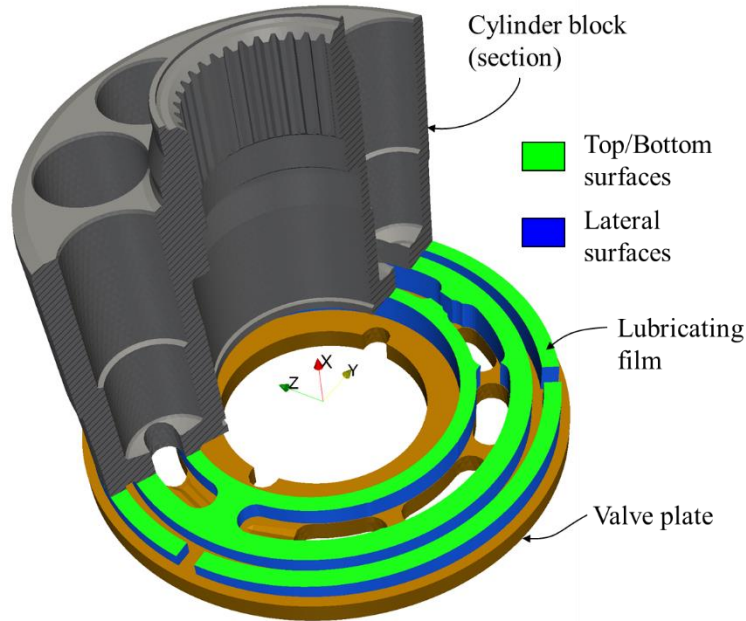


Figure 3.8. Boundary conditions for the energy equation (Zecchi, 2013).

Figure 3.8 shows the thermal boundary conditions applied on the cylinder block/valve plate interface lubricating interface for the solution of the non-isothermal fluid flow. The boundary conditions are set by the temperatures on the contacting regions. The green faces correspond to the fluid cells in contact with the solid bodies, the cylinder block and the valve plate surfaces. Similarly, the lateral faces shown in a blue color are set by the fluid volume to which they are in contact with, three options are possible: the inlet port, outlet port and the case volume. These temperatures are defined either from measurements or the thermal model described in section 3.2.

3.3.3 Elastic deformation due to pressure loads

The FEM module utilized in the thermo-elastohydrodynamic analysis assumes linearity across the whole solid domain. Therefore, the valve plate/end case assembly are considered as a single solid because the fluid structure interaction approach considers a linear model to calculate elastic deformations of the two parts (valve plate and end case), where different material properties are considered for the valve plate and the end case.

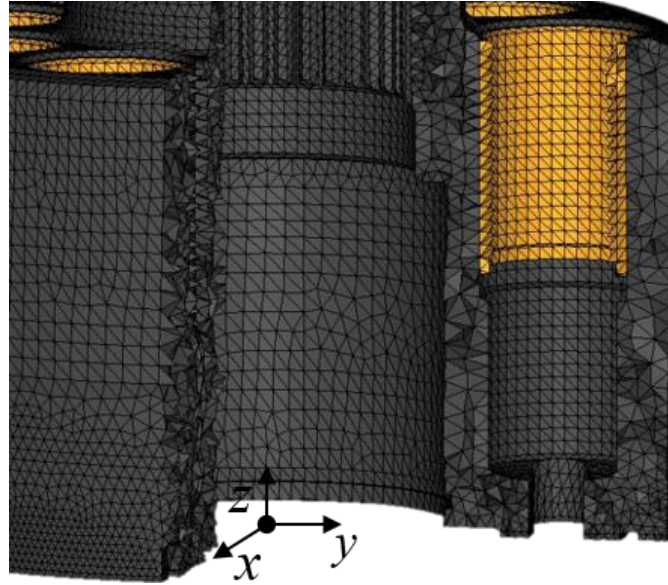


Figure 3.9. Solid mesh for the cylinder block.

Tetrahedrons are used for the 3D elements due to their simplicity allowing an easier meshing process for the solids an example of a 3D mesh is shown in Figure 3.9. As mentioned this mesh is utilized to generate the influence matrices necessary to calculate the elastic deformation due to pressure on the fluid structure interaction model.

Each of the faces that form part of the sealing gap, on the cylinder block or the valve plate, is loaded with a reference pressure of 100 bar including the displacement chambers, and suction and delivery ports. There are two possible options for the physical constraint of the solid body; fixed constraint, or inertia relief. The deformation for all the 3D tetrahedral elements is calculated but only the deformation in the z-direction of the elements conforming the sealing land are stored and save in an influence matrix. Later, when in the fluid structure interaction loop, these influence matrices are used to calculate the deformation of the sealing surface of the solid body by an off-line calculation method based on the superimposition principle and defines the deformation of the solid parts through a certain number of influence matrices. An example of the influence matrices generated is shown in the following Figure 3.10. The deformation in the lubricating gap is shown for two cases, on the left a reference pressure is applied to a single face that composes the sealing surface of the lubricating gap, and on the right the deformation due to a reference pressure applied in the displacement chamber.

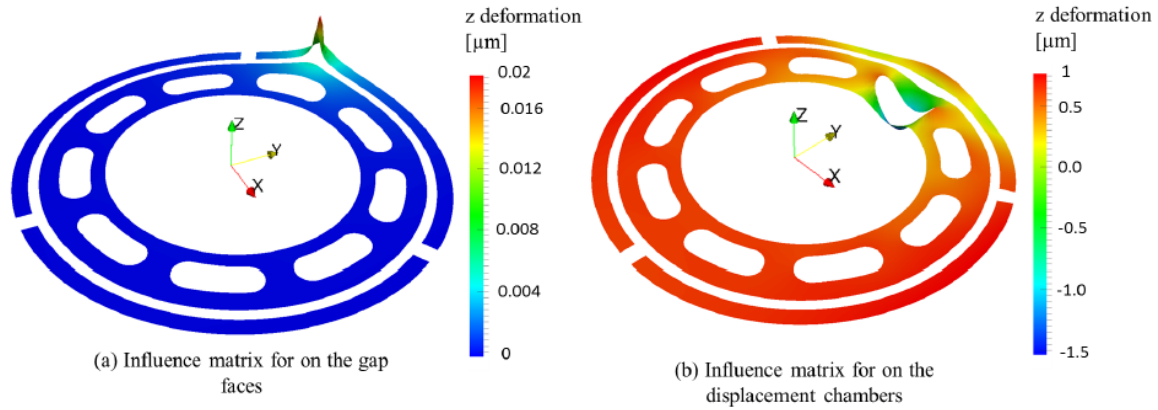


Figure 3.10. Deformation due to the reference pressure of 100 bar applied on an element face on the sealing land (a) and in one of the displacement chambers (b) (Zecchi, 2013).

This linear model approach neglects the influence of the contact problem between valve plate and end case. To check the reasonability of the obtained results a nonlinear analysis was performed to study the surface deformation more accurately using commercial finite element software. The analysis was conducted using Altair RADIOSS solver and HyperMesh. The analysis has been conducted for several sample machines utilizing the same pressure boundary conditions and fixed constraints on the end case bottom surface.

Figure 3.11 illustrates the deformation of the valve plate's sealing surface for one of the sample machine analysis mentioned. The figure on the top (a) shows the result of the linear approach and the figure on the bottom (b) shows the results of the nonlinear approach. As expected the two results are not the same, but the difference in the predicted deformations is quite small. And in terms of relative deformation, they are almost the same. The linear case maximum deformation in the z-direction is of 4.4 microns and minimum deformation is 0 microns which is a relative deformation of 4.4 microns, and for the nonlinear case the maximum deformation on the z-direction is of 6.32 microns and minimum deformation is 1.39 microns which makes the relative deformation 4.93 microns by subtracting the minimum deformation from the maximum deformation. Therefore, it was concluded that the linear approach can be used with a reasonable level of accuracy for the majority of cases of axial piston machines.

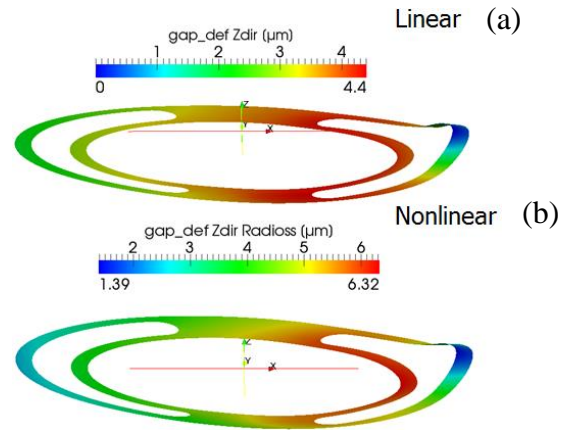


Figure 3.11. Valve plate surface deflection, comparison between linear and non-linear (deflection in z-direction).

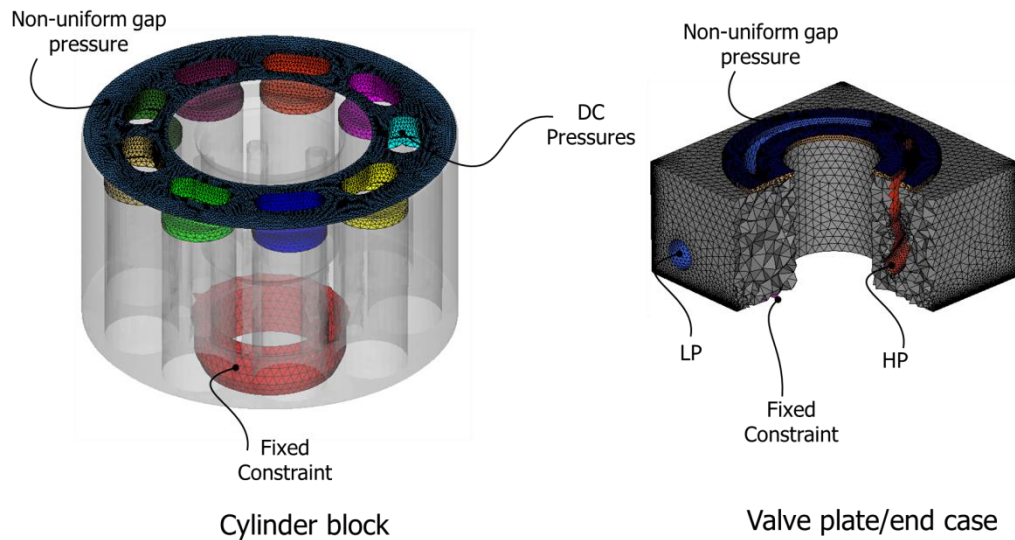


Figure 3.12. Cylinder block /valve plate interface pressure boundaries.

Pressure loads on cylinder block; valve plate and end case are responsible for elastic deformations which affect the lubricating film thickness between cylinder block and valve plate. The pressure-loaded surfaces generating deformations with a major impact on the lubricating interface performance are illustrated exemplarily in Figure 3.12.

The displacement chambers, low pressure and high pressure ports surfaces are characterized by a pressure load which can be assumed to be uniform; the load though can change in time due to the fast variation of the pressure in the displacement chamber or in the valve plate ports. The gap surfaces are instead characterized by a pressure field that is not only function of time but it is also

non-uniform (i.e. a function of space). All the described pressure loads are properly calculated and applied in the simulation model as a function of the shaft angular position: for example, the uniform pressure field applied to each of the displacement chamber and valve plate ports derived from the instantaneous displacement chamber pressure calculation.

The pressure field applied to the gap surfaces is calculated from the solution of the Reynolds equation. Figure 3.12 shows the constrained surfaces for the pressure deformation analysis on the block was done by constraining the top part of the block as shown in the, the section colored in red, and for the end case the “bottom” part of the end case was used as a fixed constraint.

3.3.4 Thermal boundaries

The thermo-elastic analysis allows the temperature field and the associated thermal deflections of the solid parts to be calculated, through the coupling of a heat transfer and a structural problem. The temperature fields of the cylinder block, valve plate and end case assemble are used as a boundary condition to solve for the energy equation in the fluid film, while the thermal deflections are applied as external modification of the fluid film thickness. Figure 3.13 the different boundary surfaces that were defined for the solution of the heat transfer problem: to each surface a different boundary condition is applied. A thermal boundary condition must be defined for each external surface boundary of the bodies.

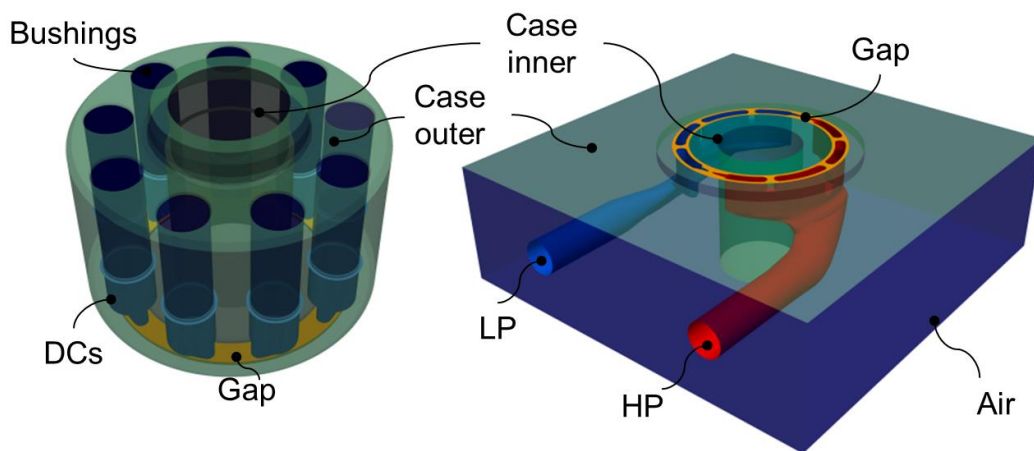


Figure 3.13. Cylinder block /valve plate interface thermal boundaries.

Two types of thermal boundary condition are usually required: Neumann or Mixed boundary. A Neumann boundary is represented by a given heat flux. This type of boundary is applied to all the surfaces in contact with fluid film, thus cylinder bore and gap surfaces on the cylinder block and valve plate bodies. The value applied to the cylinder bore was derived by averaging the heat flux calculated by the piston/cylinder interface model, the value on the surfaces bounding the fluid film between cylinder block and valve plate (labeled as “gap”) is internally calculated from the solution of the non-isothermal fluid flow and automatically applied by the simulation model. Mixed boundary conditions are applied to all the other surfaces; mixed boundary condition is the indirect specification of a heat flux through the Newton’s law of cooling:

$$q = h(T_w - T_\infty) \quad (3.13)$$

In Eq.(3.13), T_w is the temperature of the surface, which is unknown. T_∞ is the temperature of the surrounding fluid volume. The term h is the convection coefficient and it represent another unknown in this analysis; however, h can be estimated with reasonable level of accuracy through CFD simulations and it turns out that is mainly a function of the machine’s speed and displacement. The values provided in the two tables above have been determined using a separate CFD simulation. The boundary conditions assigned to each surface for the cylinder block surfaces are shown in Table 3.1, and similarly, Table 3.2 shows the boundaries for the valve plate and end case assembly.

Table 3.1.: Thermal boundary conditions applied to the cylinder block

Cylinder block thermal boundary conditions		
Name	BC type	Value
Gap	Neumann	(calculated)
Case inner	Mixed	T_{∞} = Case temp [°C]; h = TBD [W/m ² K]
Case outer	Mixed	T_{∞} = Case temp [°C]; h = TBD [W/m ² K]
DCs	Mixed	T_{∞} = Case temp [°C]; h = TBD [W/m ² K]
Bushings	Neumann	From lubricating interface

Table 3.2.: Thermal boundary conditions applied to the valve plate & end case assembly

Valve plate & End case thermal boundary conditions		
Name	BC type	Value
gap	Neumann	(calculated)
case	Mixed	T_{∞} = Case temp [°C]; h = TBD [W/m ² K]
metal	Mixed	T_{∞} = Case temp [°C]; h = TBD [W/m ² K]
LP	Mixed	T_{∞} = LP temp [°C]; h = TBD [W/m ² K]
HP	Mixed	T_{∞} = HP temp [°C]; h = TBD [W/m ² K]
Air	Mixed	T_{∞} = Ambient temp [°C]; h = TBD [W/m ² K]

3.3.5 Piston / Cylinder Interface

This section describes the loading conditions used to calculate the deformations of the piston/cylinder lubricating gap surfaces due to pressure loading and thermal effects. Analyses for pressure induced deformation and temperature induced deformation are carried out separately. However, the same mesh geometry is used for both. (Note that this is done for convenience; different meshes can be used as desired for each analysis.) Different boundary conditions must be applied, corresponding to pressure and thermal loading, respectively.

3.3.6 Elastic deformation due to pressure loads

The meshes for the piston and cylinder are shown in Figure 3.14. Note that the cylinder mesh includes the entire cylinder block and appropriate material properties are given to both.



Figure 3.14. Piston and cylinder block mesh.

The piston/cylinder interface model requires many different boundary conditions. These different boundaries will be described in this section. Some of the boundaries that need to be defined are the ones needed to solve the Reynolds equation in the lubricating gap, others the boundary conditions for the elastic deformation analysis of the solid bodies; both for the thermal and pressure problem.

The boundary conditions for pressure deformation are shown in Figure 3.15. The deformations of a single reference cylinder bore and piston are used to calculate the change in gap thickness. The piston surface associated with the lubricating gap is shown in red in Figure 3.15. The piston

surface is loaded with the pressure field calculated solving the Reynolds equation which varies with angular position. The piston and cylinder bore surfaces are not always in the lubricating gap. The piston translates in and out of the cylinder bore which exposes the surfaces to different pressure loadings; the gap, the case, or the displacement chamber. The areas which extend outside of the lubricating interface into the case are loaded with case pressure and the areas which extend into the displacement chamber are loaded with the displacement chamber pressure. The displacement chambers, shown in blue, are loaded with the corresponding pressure from the instantaneous pressure in the displacement chamber calculation dependent on the angular position. The surfaces shown in green are loaded with case pressure. This is modeled as a constant, uniform pressure field. For the cylinder block and piston the inertia relief technique is used to constrain the solid parts during the pressure deformation (Pelosi & Ivantysynova, 2013).

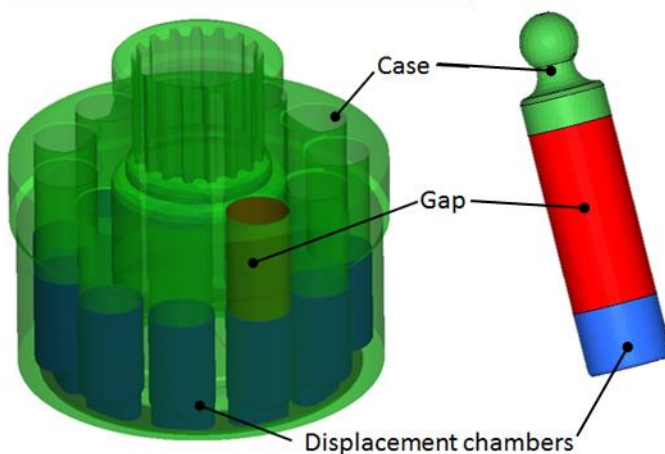


Figure 3.15. Piston/cylinder interface pressure boundaries.

3.3.7 Thermal boundaries

Similarly, as for the cylinder block/valve plate interface, the piston and cylinder interface temperature fields and resulting deformations need to be calculated. Figure 3.16 shows the thermal boundary regions used for the piston/cylinder interface. Note here that all gap surfaces including the reference bore are selected to receive the heat flux calculated in the gap, though only the deformations calculated in the reference gap will be used in the simulation. Both heat flux (Neumann) and mixed boundaries are applied as indicated in Table 3.3. This table shows the applied boundary conditions to each surface and its associated value.

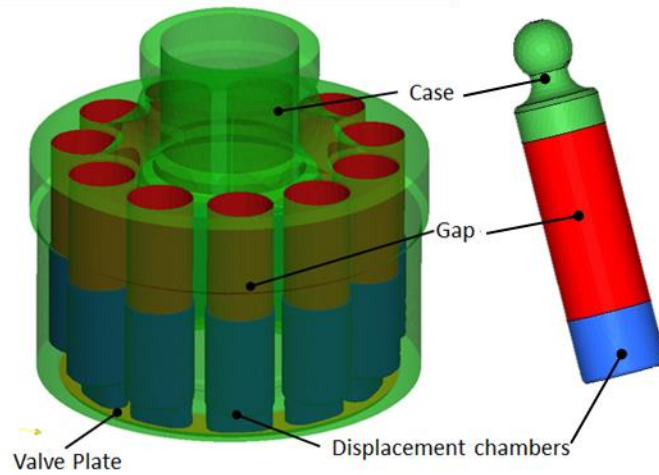


Figure 3.16. Piston/cylinder interface thermal boundaries.

Table 3.3.: Piston/cylinder interface thermal boundaries

Piston/cylinder thermal boundary conditions		
Name	BC type	Value
Gap	Neumann	(calculated)
Case	Mixed	$T_{\infty} = \text{Case temp } [^{\circ}\text{C}]; h = \text{TBD } [\text{W}/\text{m}^2 \text{K}]$
Displacement Chambers	Mixed	$T_{\infty} = \text{Case temp } [^{\circ}\text{C}]; h = \text{TBD } [\text{W}/\text{m}^2 \text{K}]$
Valve Plate	Mixed	$T_{\infty} = \text{Case temp } [^{\circ}\text{C}]; h = \text{TBD } [\text{W}/\text{m}^2 \text{K}]$

3.3.8 Slipper / Swash plate Interface

The slipper/swash plate interface boundary conditions for the non-isothermal flow, and the pressure and thermal deformations of the slipper and swash plate lubricating interface are discussed in the following sections.

The fluid film computational domain is discretized utilizing a structured three-dimensional mesh. The energy equation is solved utilizing this fluid mesh, see Figure 3.17. A similar two-dimensional mesh is utilized for the solution of the Reynolds equation as shown on the left of Figure 3.18.

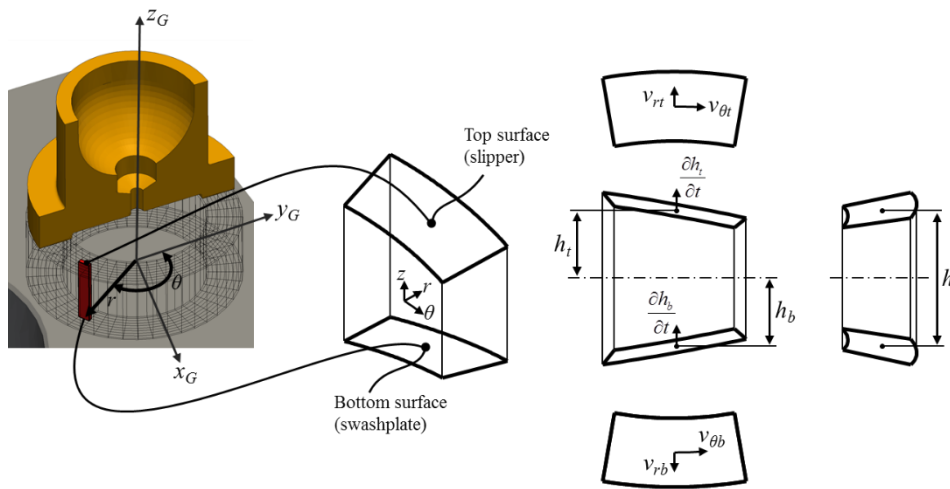


Figure 3.17. Structure grid used to solve the fluid flow energy equation (Schenk, 2014).

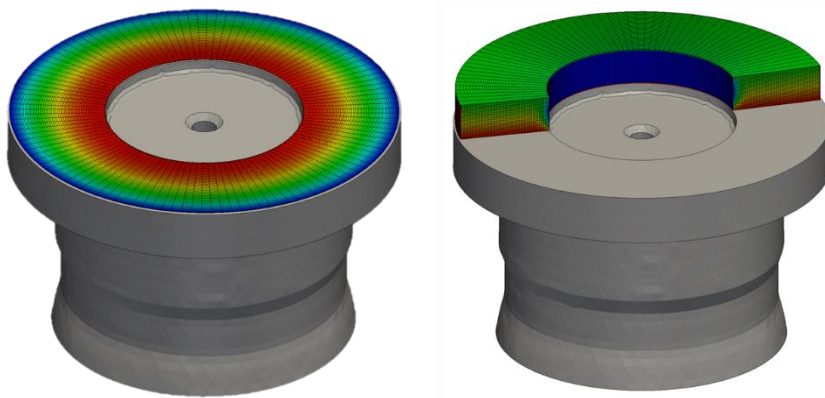


Figure 3.18. Structured grid used for the Reynolds (left) and energy equations (right).

- **Elastic deformation due to pressure loads**

The slipper solid body is meshed using first order linear tetrahedral elements. The example shown in Figure 3.19 meshed with a thin layer assigned for bronze material and the rest of the slipper is steel.

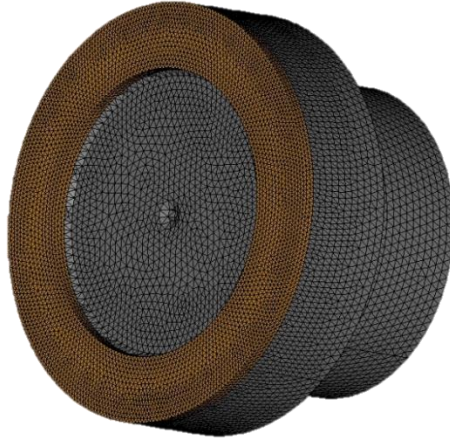


Figure 3.19. Fine mesh of a bimetal slipper.

The sealing gap pressure is interpolated from the polar fluid mesh to the unstructured solid mesh providing an accurate loading scheme. The case pressure is assumed constant, and the pocket pressure is constantly updated using the calculated value. The socket pressure is calculated using a simplified approach:

$$p_{socket} = \frac{F_{SK}}{A_{socket}} \quad (25)$$

Where A_{socket} is not the surface area of the socket, but rather the socket area projected in the swashplate plane. Generally, this is just the area of a circle with a diameter equal to the socket diameter.

The slipper is not constrained using rigid body constraints, but instead any force imbalance is compensated for using the inertia relief technique. To properly constrain the mechanical system, a weighted constraint is imposed which fixes the center of mass to zero displacement.

The swash plate is loaded with each of the slipper's pressure interpolated to the running surface. In addition, a case pressure load is applied to all other surfaces, and the fixed constraint as depicted in Figure 3.20.

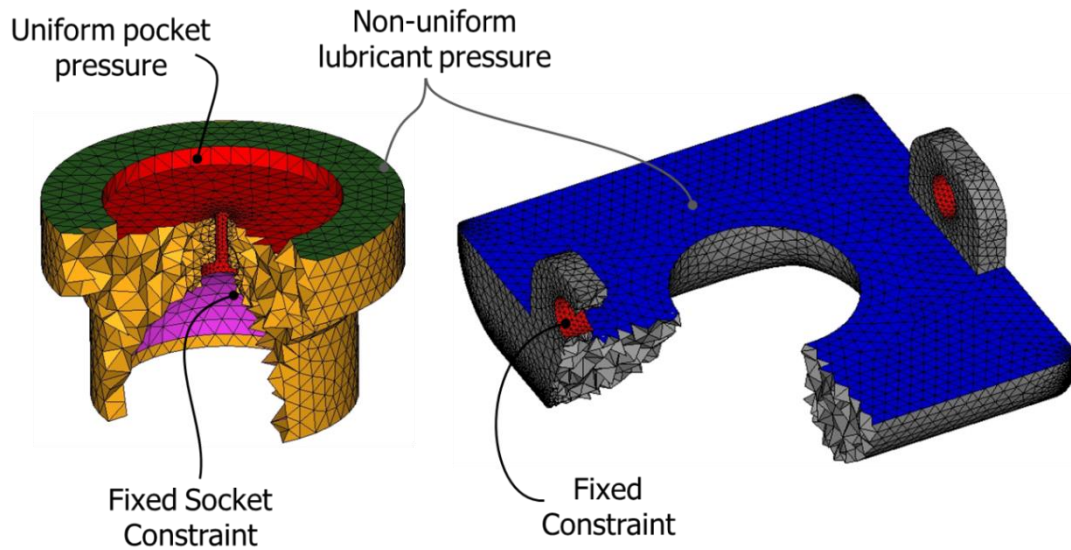


Figure 3.20. Pressure boundary conditions on the slipper and swash plate.

3.3.9 Thermal boundaries

The thermo-elastic analysis allows the temperature field and the associated thermal deflections of the solid parts to be calculated, through the coupling of a heat transfer and a structural problem. The temperature fields of the slipper and swash plate are used as a boundary condition in the solution of the energy equation for the lubricating interface, while the thermal deflections are applied as an external modification on fluid film thickness. Figure 3.21 shows the three-dimensional mesh of the slipper (top) and the swashplate (bottom) with the surface boundary definitions.

Two types of thermal boundaries are applied in the slipper / swash plate thermos-elastic analysis: Neumann and mixed boundaries. The boundary conditions applied to each surface are specified in Table 3.4 for the slipper and

Table 3.5 for the swash plate. The surface which is contact with gap was assigned the Neumann boundary which is a heat flux field calculated in the thermo-elastohydrodynamic model.

The mechanical constraints for the thermos-elastic analysis is the same to that of the pressure deformation analysis. The slipper is constrained utilizing the inertia relief method since its movement is not constrained in any mechanical manner. The swash plate is constrained utilizing the Dirichlet method by fixing the nodes on the surface colored red in Figure 3.21 which would be in contact with the bearing holding it fixed.

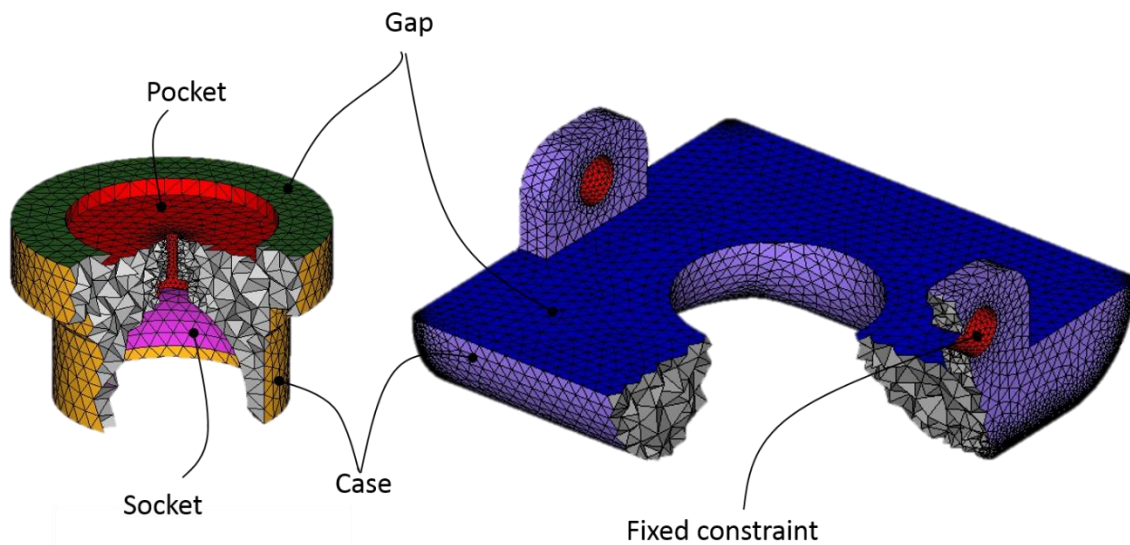


Figure 3.21. Thermal boundary conditions on the slipper and swash plate.

Table 3.4.: Thermal boundary conditions for the Slipper

Slipper thermal boundary conditions		
Name	BC type	Value
Gap	Neumann	(calculated)
Case	Mixed	T_{∞} = Case temp [°C]; h = TBD [$\text{W}/\text{m}^2 \text{K}$]
Socket	Mixed	T_{∞} = Case temp [°C]; h = TBD [$\text{W}/\text{m}^2 \text{K}$]
Pocket	Mixed	T_{∞} = Inlet and outlet average [°C]; h = TBD [$\text{W}/\text{m}^2 \text{K}$]

Table 3.5.: Thermal boundary conditions for the swashplate

Swashplate thermal boundary conditions		
Name	BC type	Value
Gap	Neumann	(calculated)
Case	Mixed	T_{∞} = Case temp [°C]; h = TBD [$\text{W}/\text{m}^2 \text{K}$]
constraint	Mixed	T_{∞} = Case temp [°C]; h = TBD [$\text{W}/\text{m}^2 \text{K}$]

3.3.10 Slipper/Swash plate interface convection coefficients calculation

The convection coefficients required for solid bodies mixed thermal boundaries a CFD analysis is necessary. The CFD simulation requires the fluid volume to be extracted from the axial piston machine. The boundary conditions are set by applying a rotational velocity to the slipper/piston and cylinder block assembly which is associated with the operating condition of interest. Figure 3.22 shows a representation of the fluid flow around the rotating group is shown, with a color scale representing the linear velocity [m/s] on the surface of the solids and arrows representing the velocity of fluid flowing in the case.

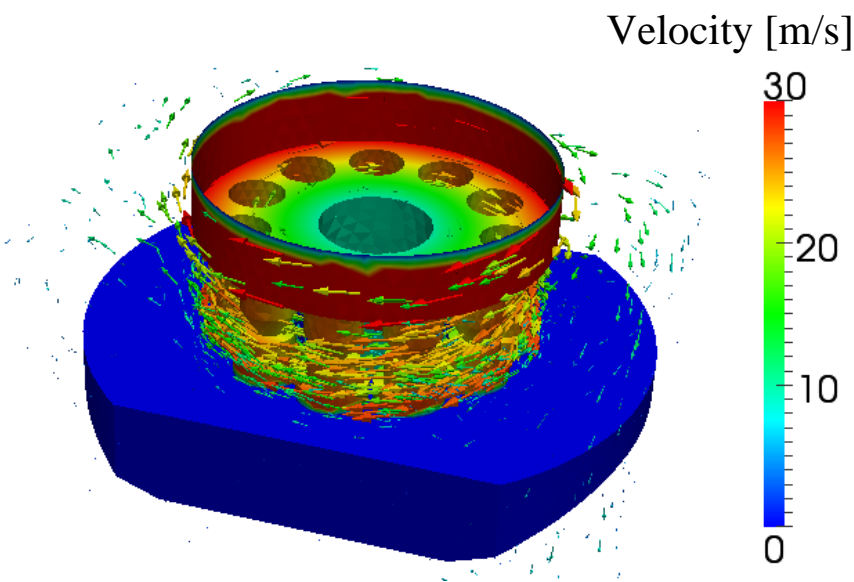


Figure 3.22. Fluid flow around rotating kit.

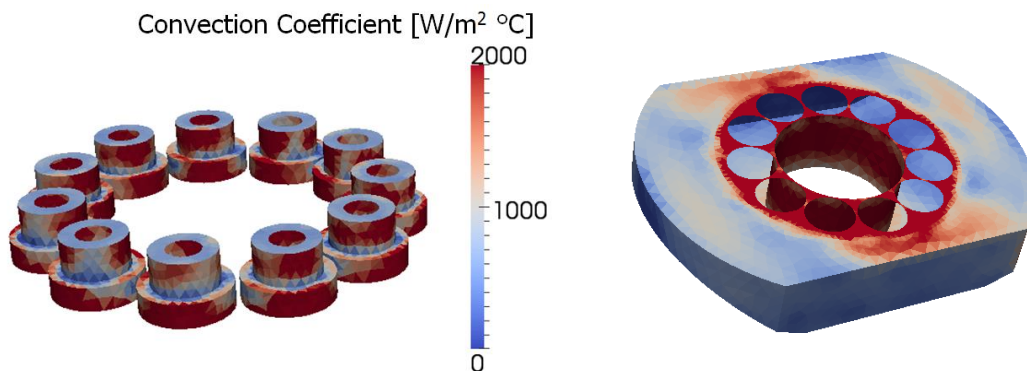


Figure 3.23. CFD simulation results, convection coefficients.

The simulation results of the CFD analysis are shown above in Figure 3.23, where the convection coefficients are represented in the red-blue color scale (cool-warm scale) for both the slippers and the swashplate. This CFD analysis was done for several industrial machines. The mean values used in the model for the different operating conditions in the two solid bodies are shown in Table 5, the coefficients shown were calculated for a single machine. Linear speed is calculated utilizing the pitch diameter and rotational speed:

$$v_l = \omega \cdot R \quad (25)$$

Table 3.6.: Convection coefficients used for the slipper swashplate interface.

Linear speed (m/s)	Mean Convection	Mean Convection
	Coefficient (W/m ² °C)	Coefficient (W/m ² °C)
	Slipper	Swashplate
25	1002.85	839.62
28.25	1075.85	905.75
31.4	1147.81	971.05
34.5	1217.49	1035.74
37.5	1286.57	1099.12
40	1353.89	1161.03
44	1420.77	1223.12
Mean Coefficient	1215	1034

4. DESIGN METHODOLOGY OF SWASH PLATE TYPE AXIAL PISTON MACHINES

The goal of this chapter is to describe the methodology proposed in this thesis for the virtual prototyping of swash plate type axial piston machines. The methodology's approach is described in detail and examples are provided for every part of the methodology.

4.1 General Design Methodology Overview

Virtual prototyping of axial piston machines is detailed in the flow chart shown in Figure 4.1. The first step is to identify the required performance data of the positive displacement machine will be used. The main performance data of the machine are: maximum displacement volume [cc/rev], maximum operating pressure and maximum and minimum speed. This first step is crucial because the rest of the machine design derives from the performance requirements.

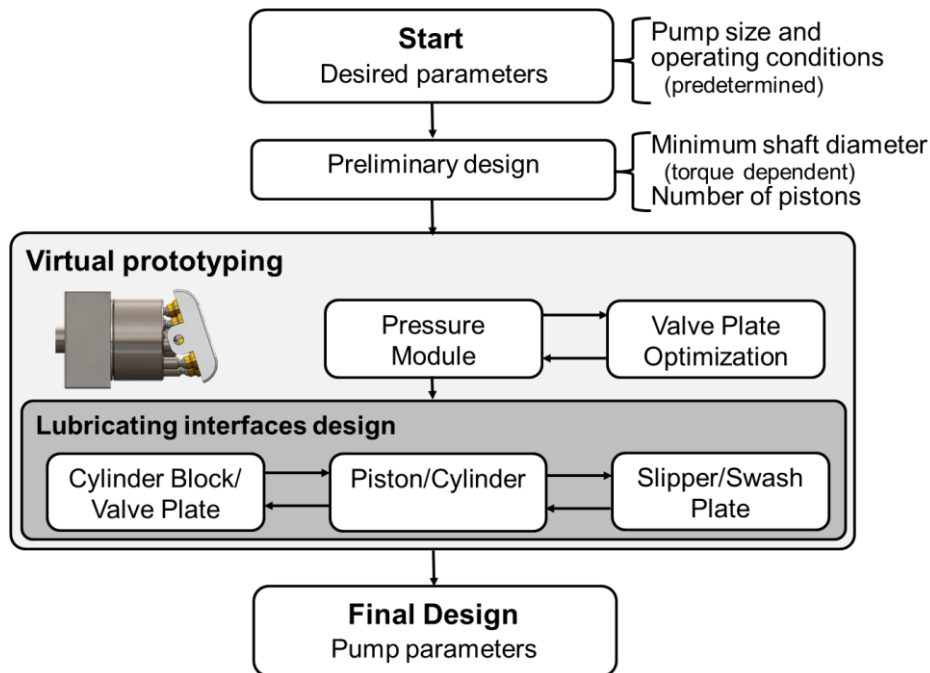


Figure 4.1. General design methodology flowchart.

The second step is the preliminary design, where all the main parameters of the machine are derived. After that the virtual prototyping can begin. First step within virtual prototyping is the analysis of the preliminary design in terms of calculating the following parameters using the mathematical models described in the previous chapter. The pressure module provides effective flow rate, flow ripple, pressure in the displacement chamber, pulsating swash plate moments M_x , M_y , and M_z , as well as, internal leakage. The thermal model will be used to predict fluid temperatures of the machine's discharge port and the case volume.

The three lubricating interface models are used to calculate the following parameters:

- Fluid film thickness between the piston and the cylinder bore, the cylinder block and the valve plate, and the slipper and the swash plate.
- Pressure fields in the fluid film in the lubricating interfaces.
- Leakage flows in all three lubricating interfaces.
- Energy dissipation due to viscous flow in all three lubricating interfaces.
- Temperature distributions in the fluid film and main pump parts (cylinder block, piston, valve plate, slipper, swash plate, and end case).
- Surface deformations of cylinder block, piston, valve plate, slipper, and swash plate due to pressure and thermal loading of these parts.

The parameters will provide the machine designer with the necessary insight to make the decision of which parts require design improvement through optimization. The component's features and dimensions are selected arbitrarily and iteratively depending on the application. The optimization takes place when the design is refined.

4.2 Preliminary Design

The main dimensions of the axial piston machine components are defined in this phase. Pump designers strive to achieve the best pump design by achieving highest energy efficiency, power density, and reliability while maintaining low noise emissions for a range of operating conditions. These are all equally important and some have adverse effects on each other. One example of such a scenario is high efficiency may result in higher manufacturing costs due to higher manufacturing tolerance requirements or material selection.

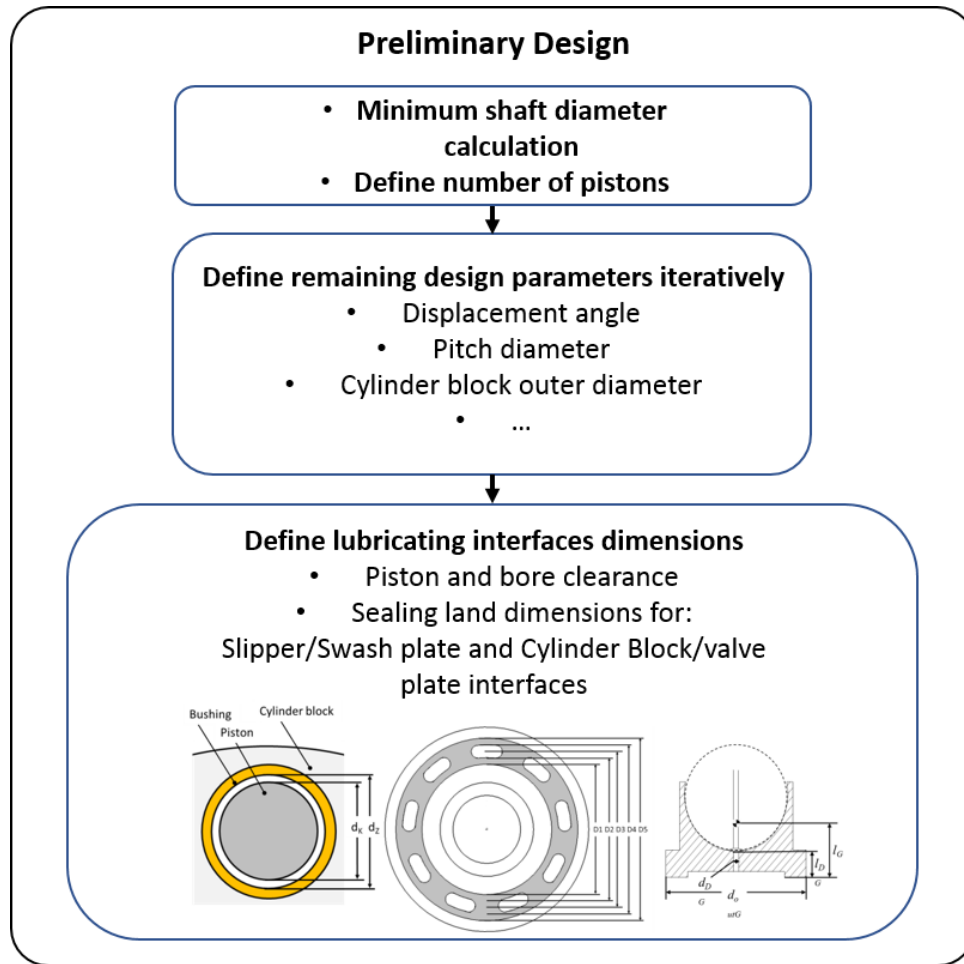


Figure 4.2: Preliminary design flowchart.

The preliminary design shown in Figure 4.2 involves simplified assumptions. First, the number of pistons must be selected together with the minimum shaft diameter required to transmit the desired maximum torque. These two parameters constrain all the base geometrical dimensions of the machine parts; i.e. maximum displacement angle β , piston length l_K , pitch diameter d_B , piston diameter d_K , etc. The base geometrical dimensions are shown in Figure 4.3. The combination of these parameters defines the geometrical displacement of the machine. The shaft diameter calculation must be done first since it will constrain the size of all the other remaining dimensions. An odd number of pistons is most commonly selected because it results in a smaller flow and torque ripple as it has been shown by Ivantysyn and Ivantysynova (2001). The remaining

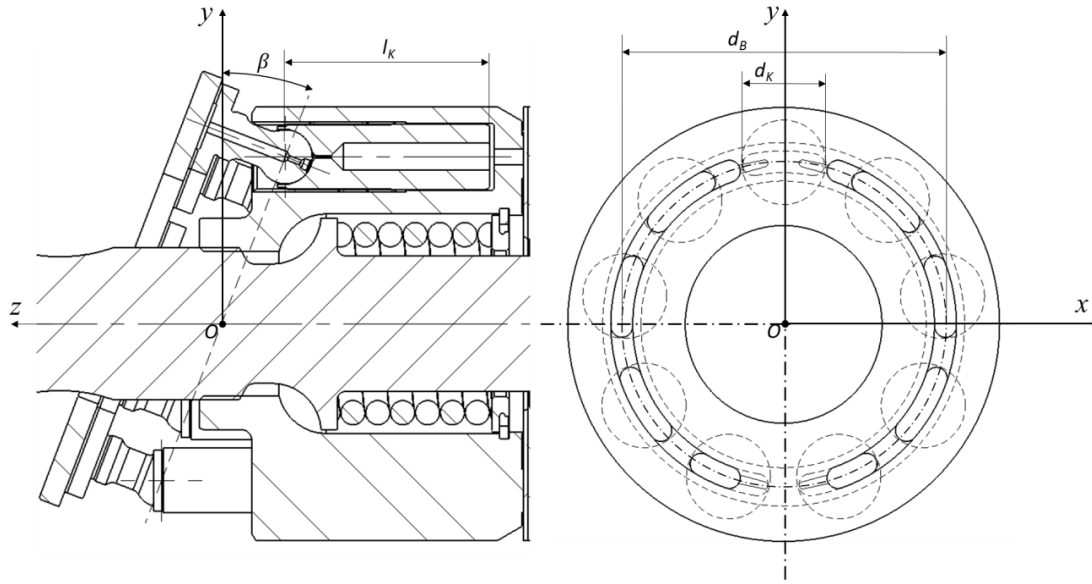


Figure 4.3. Main geometrical dimension of axial piston machines of swash plate type.

variables are calculated in an iterative process. The outer and inner cylinder block diameters depend on the shaft, the cylinder block spring, and the pitch diameter which depends on the maximum piston diameter. The piston diameter should be in a range where no physical limitations could be violated due to side forces on the piston resulting in large stresses on the solid body. The displacement angle β is the angle formed between the swash plate running surface plane and the valve plate running surface plane. The swash plate angle is a critical parameter influencing the dimensions of the machine and its performance. An advantage of axial piston machines of swash plate type with large displacement angles is their compactness. The disadvantages are resulting large side forces and moments on the piston/cylinder interface. These large side forces and moments generate issues when balancing the external loads and fluid forces in the piston/cylinder interface and generate additional stresses on the cylinder block solid. One way to reduce the moments on the piston/cylinder interface is to change the overhang length l_0 .

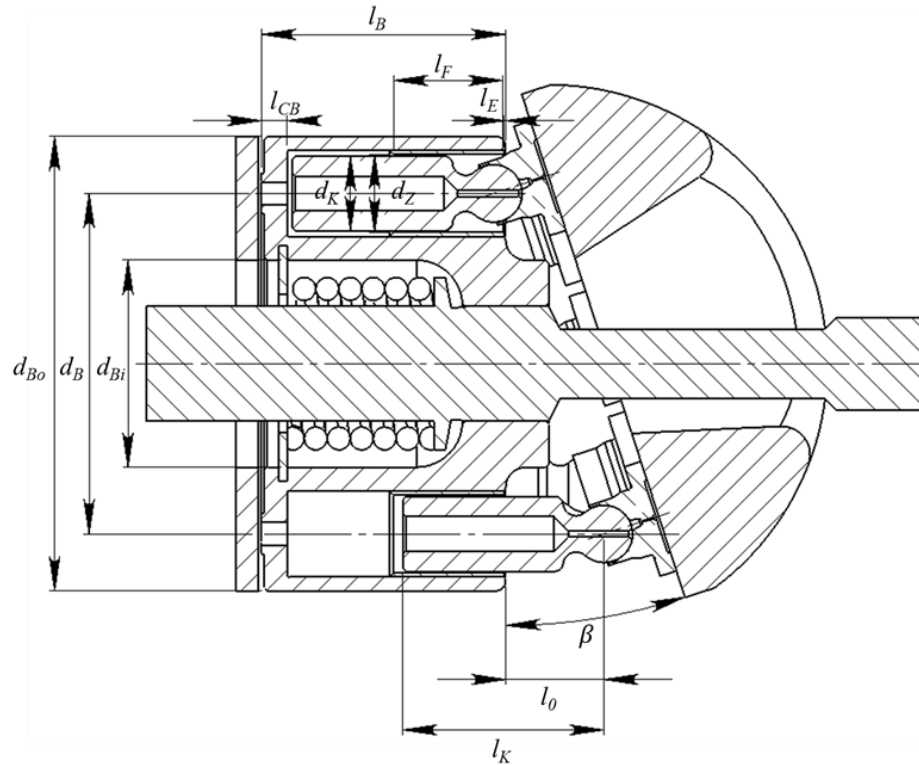


Figure 4.4. Axial piston machine main dimensions.

The geometrical dimensions for the lubricating interfaces (cylinder block/valve plate and slipper/swash plate and piston/cylinder) also need to be generated in this step within the preliminary design. Within this process, the three lubricating interfaces are assumed to have parallel gaps resulting in fixed fluid film heights. This simplification allows to find first main dimensions for the lubricating interfaces by neglecting hydrodynamic and elasto-hydrodynamic effects, i.e. considering only hydrostatic forces created in the fluid film. Because this is a simplified assumption, which on one side allows the calculation of main dimensions of these interfaces using analytical expressions, correction factors, so called balancing factors are introduced to make up for the missing hydrodynamic and elasto-hydrodynamic effects being present in a real machine. The balance factors were found in an experimental heuristic design process by manufacturers over the last five decades. Similarly, for the piston/cylinder interface the required clearance is defined assuming a centered position of the piston in the cylinder bore. More details about the preliminary design and the range of balance factors can be found in Ivantysyn and Ivantysynova (2001).

4.3 Virtual Prototyping

The virtual prototyping process for axial piston machines of swash plate type proposed in this thesis will be described in detail in this chapter. Examples for its successful application will be provided. The virtual prototyping design objectives are to achieve a design which fulfills the following:

- Stable full fluid film with enough load carrying ability to avoid metal-to-metal contact
- Lowest energy dissipation in all three lubricating interfaces in the given range of operating condition
- High volumetric efficiency
- Low flow and torque ripple
- Low moment pulsation (ΔM_x and ΔM_y)
- Low control effort on the swash plate (for variable displacement units)
- No cavitation

The goal is to use sophisticated fluid structure interaction models, which can consider all the features of the machine for the three main lubricating interfaces; part shape and dimensions, along with material and fluid properties to determine optimal final dimensions for a given preliminary design. In Figure 4.5 the virtual prototyping flowchart is depicted. The main parameters are calculated in the preliminary design phase. These design parameters are the inputs for the various numerical models utilized in the virtual prototyping process of the axial piston machine. The valve plate design is the first step since it will determine the displacement chamber pressure profile. The displacement chamber pressure will impact the design of all three lubricating interfaces.

The next step is the creation of three-dimensional CAD models. The three-dimensional CAD models are to be compliant with the base design parameters from the preliminary design phase, and they need to be stiff enough to bear the external loads imposed on them while maintaining minimal surface elastic deformations. The latter performance requirement is evaluated utilizing a FEM model to quantify stress distributions and elastic deformations. The three-dimensional CAD models need to be discretized into a three-dimensional mesh and have the boundary conditions defined to analyze it in the FEM model. The maximum surface deformation allowed is defined by the pump designer, and this is dependent on the lubricating interface sensibility to the same. The

three-dimensional CAD models need to be modified accordingly to meet all the design requirements. The parts shapes and material selection can be varied until an optimum design is found.

Finally, the lubricating interfaces design block use the following as inputs: the base parameters collected from the preliminary design phase, the valve plate design, and the solid bodies design are utilized as inputs for the thermo-elastohydrodynamic model (TEHD). The thermal model is coupled with the TEHD model. The thermal model predicts the discharge port and case volume temperatures and feeds them into the TEHD model. The TEHD model uses the updated temperatures from the discharge ports, and case volume calculated with the thermal model and the displacement chamber pressure in the displacement chamber, and the three-dimensional meshes for the cylinder block, the valve plate/end case assembly, the slipper, the swash plate, and the piston. The TEHD model will calculate, as mentioned previously, the fluid film thickness, the pressure field distribution, the temperature field distribution, surface elastic deformations, leakage flow and the energy dissipation due to viscous flow in all three lubricating interfaces. The leakage flows through all three lubricating interfaces is used as an input for the pressure module, which updates the calculation of the instantaneous pressure in the displacement chamber, the effective flow, the pressure and flow ripples, the internal leakage and swash plate moments. The energy dissipation and updated case flow are used as inputs for the thermal model to update the discharge port and the case volume temperatures. This process becomes an iterative process until the discharge flow and case volume temperatures, the case flow, and the energy dissipation in the lubricating interfaces do not change from one iteration to the next. The lubricating interfaces design process shown in the flowchart in Figure 4.5 is a general overview of the process. The methodology consists of generating a design of experiments based on Latin hypercube, full factorial or fractional factorial approach. The designs are then analyzed following the sequence described above where the pressure module, the TEHD and the thermal model are coupled.

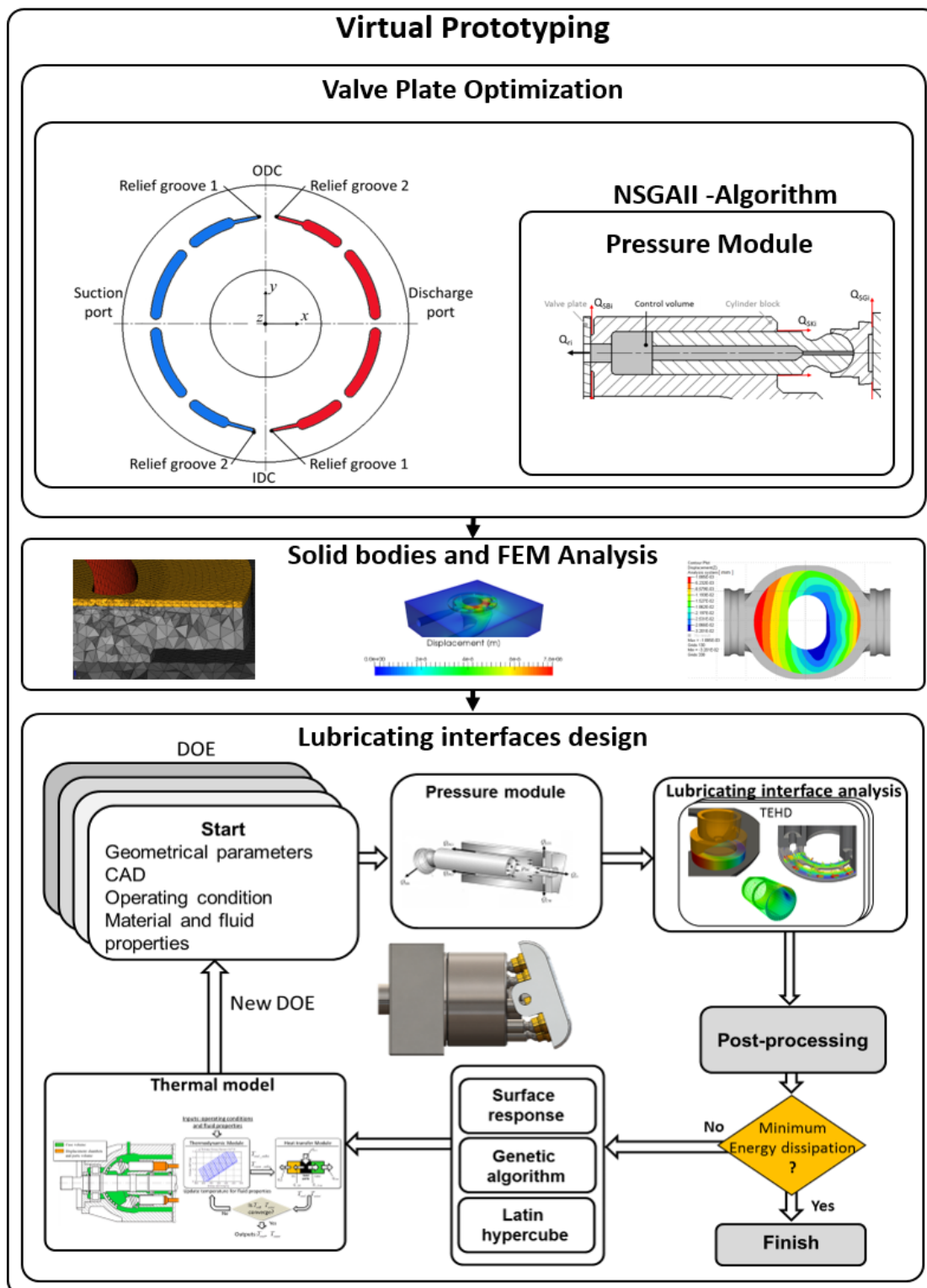


Figure 4.5. Virtual prototyping flowchart.

The block in Figure 4.5 showing the surface response, the genetic algorithm and Latin hypercube sampling is an optional step. In this optional step, a black box approach using a surface response or surrogate model (response surface method) is used to optimize the lubricating where the surrogate model replaces the TEHD model and reduces drastically the computational cost of the virtual prototyping. After, the black box approach any optimal design needs to be evaluated using the pressure module, thermal and TEHD models. The minimal energy dissipation requirements for the lubricating interfaces are set by the designer. This design process will maintain as a constraint not to allow extreme minimum fluid film thickness within the range of operating conditions.

4.4 Case Study

In this section, a case study is described which was used as an example to validate the computational based methodology proposed to design axial piston machines. The following chapters in this thesis will show examples which are based from this case study. The virtual prototype displacement volume is 24 cc per revolution. The maximum achievable swash plate angle is 21° which is relatively large typically angles are between $16\text{--}18^\circ$. This swash plate angle allows the machine to be more power dense and this due to the selection of an extended male slipper design. A cross section of the axial piston machine used as a case study is shown in Figure 4.3. The swash plate type axial piston machine prototype was specified to be able in a wide range of operating conditions. The pressure differential ranged from 0–400 bar, with max operating pressure of 450 bar. The shaft speed to be between 500–4000 rpm. The prototype's rotating group components were designed to have a variable displacement with swash plate angle range from 0– 21° . The temperature could vary from 0°C to 80°C . The main geometrical dimensions are described in Table 4.1.

5. VALVE PLATE ANALYSIS AND DESIGN OPTIMIZATION

As mentioned in the previous chapters. The valve plate it is a critical component of the axial piston machines. The valve plate performs multiple functions simultaneous. The valve plate controls how the displacement chambers connect and disconnect from the suction and delivery ports and it also constitutes part of the cylinder block/valve plate interface bearing the external loads and sealing the pressurized volumes from the case volume. The first, these connections are critical to the pressure build up in the displacement chamber. This has a direct impact on various performance parameters of the positive displacement machine:

- Displacement chamber over pressurization (spikes) or under pressurization (vapor release/cavitation).
- Volumetric efficiency due to internal leakage due to crossflow and compressibility.
- Flow ripple.
- Moments on the swash plate and rotating group.

In chapter 3, it was mentioned that the design of the valve plate through an optimization methodology is the first step in the virtual prototyping process. The main objectives in valve plate optimization are the following:

- Optimize pressure orifice in displacement chamber to avoid cavitation.
- High volumetric efficiency.
- Low flow ripple.
- Low control effort on the swash plate.
- Low moment pulsation (ΔM_x and ΔM_y).

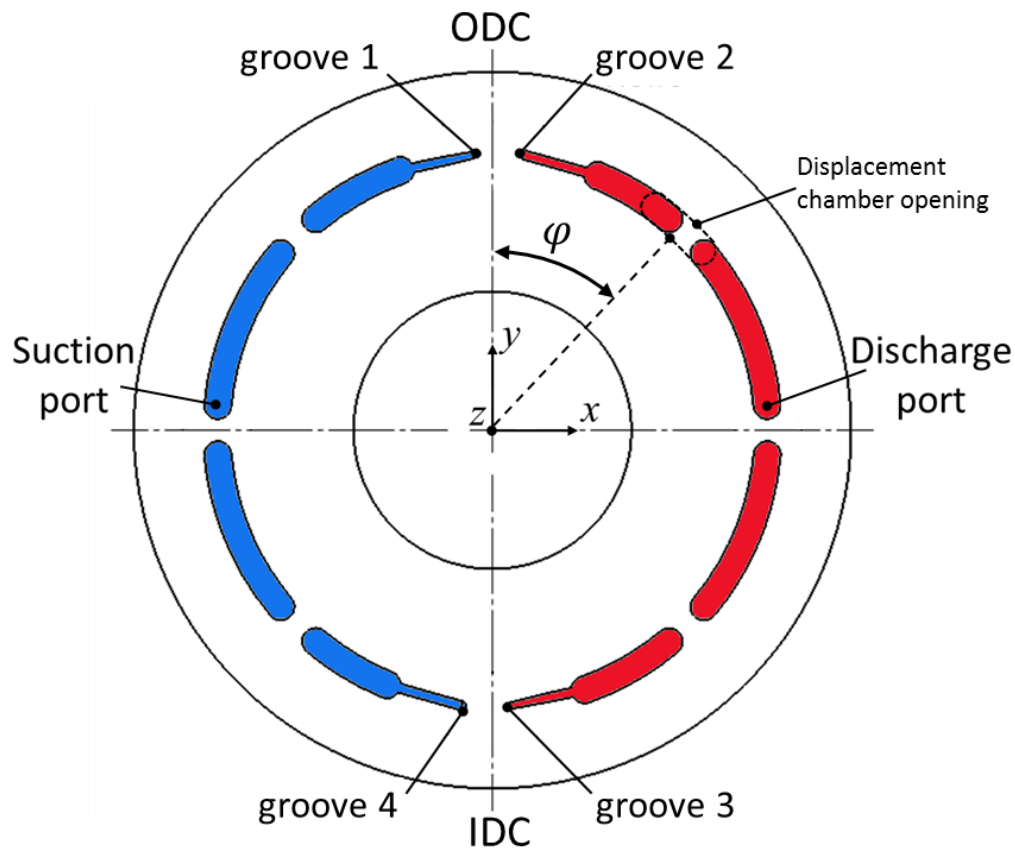


Figure 5.1. Valve plate representation.

The valve plate design parameters are those who modify how the suction and the discharge ports connect to the displacement chamber. A common design feature and the design feature utilized in this work is to add precompression and decompression grooves to the valve plate openings which help to control the amount of flow to and from the chamber, see Figure 5.1. The controlled flow through these grooves determine how the pressure rises and drops inside the displacement chamber. Figure 5.1 shows the top view of a valve plate representation. In this representation the valve plate is for a axial piston machine in a pumping operating condition. The shaft and rotating group rotation is in the clockwise direction, the kidney of the reference displacement chamber is shown in the figure, which position is a function of the shaft angle, φ . The outer dead center (ODC) which is the point where the piston is the farthest from the valve plate is in the positive y-axis and the The precompression grooves are grooves one and two. The decompression grooves are three and four.

The mathematical model used to calculate the pressure profile of the displacement chamber pressure has been explained in Chapter 0. In that model flow through a turbulent orifice is assumed. Therefore, the goal is to determine the smallest opening area of the valve plate area for each considered rotating angle of the cylinder block used in Eq. (3.2) as a function of the shaft angle. Figure 5.2 shows a representation of the opening from the valve plate port opening to the displacement chamber.

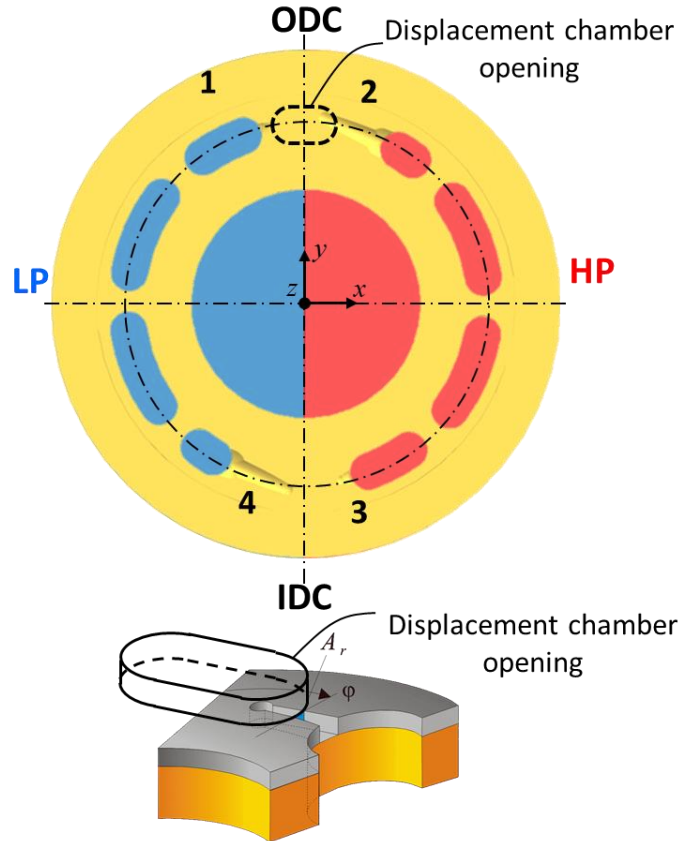


Figure 5.2: Valve plate area opening to the displacement chamber representation.

The calculation of the opening area profile for any valve plate can be performed using the following approach. First, an assembly needs to be created utilizing a commercial CAD software. Figure 5.3 shows the representation of this process where the cylinder block is positioned on top of the valve plate, concentric to each other. The reference displacement chamber should be intersected by the y-axis, shown in Figure 4.5 and Figure 5.1. The negative or fluid volume needs to be extracted from this assembly, by Boolean operations on the volumes. Afterwards the potential flow is calculated imposing a fluid velocity at the inlet on the top of the displacement chamber and a zero-pressure boundary condition on the outlet at the bottom of the valve plate port. The

minimum cross-sectional opening area is found using numerical tool called AVAS (Ivantysynova, Huang, & Christiansen, 2004). This tool automatizes the opening area profile calculation for each shaft angle the process by rotating the displacement chamber negative volume relative to the z-axis and by repeating the process for each shaft angle.

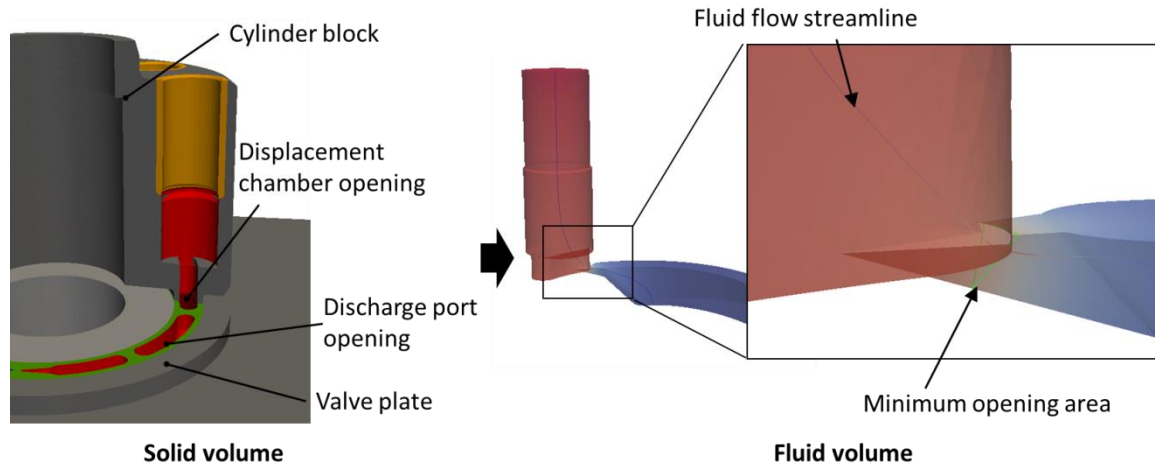


Figure 5.3. Opening area profile to the displacement chamber from the discharge and suction ports representation.

Figure 5.4 shows a representative opening area profile of a valve plate, the blue line is the opening to the discharge port and the orange line is the suction port opening.

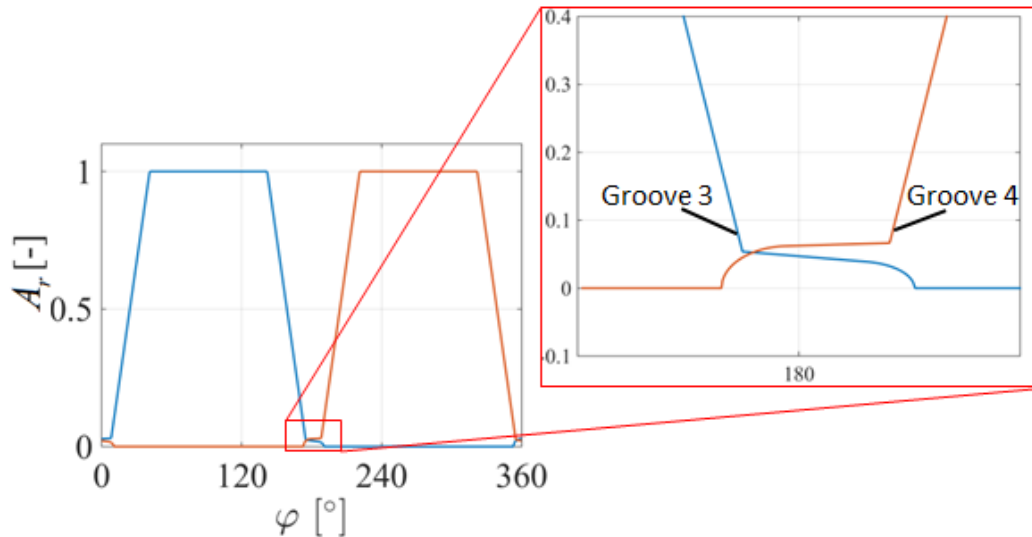


Figure 5.4. Opening area profile to the displacement chamber from the discharge and suction ports as a function of the shaft angle.

The valve plate design objectives require the use of an optimization process. The optimization algorithm utilized within the virtual prototyping process changes precompression and decompression grooves to optimize the objective functions described in the previous section. The valve plate design process relies on the pressure module and the VpOptim models coupled with a multi-objective genetic algorithm the multi-objective genetic algorithm NSGA II. It is a non-dominated sorting genetic algorithm, which offers many advantages over other optimization schemes. It can solve large globalization optimizations and generates a distributed Pareto front (Deb et al., 2002).

First, the NSGA II generates a design of experiments then this is transferred to VpOptim. VpOptim translate the DOE into inputs for the pressure module. The pressure module simulates the entire population of designs. The output from the pressure module is parsed by VpOptim into the function evaluations necessary for the NSGA II optimization algorithm. Once the Pareto front has been generated, the designer needs to choose a design based on a weighted cost function. The optimization methodology was modified based on previous work done which considered only one quadrant of operation (Kalbfleisch, 2015).

The main contribution of the work in this chapter is the augmentation of quadrants of operation for which the multi-objective genetic algorithm was used. The previous work had only focused on one quadrant of operation for the axial piston machine. Figure 5.5 shows the four quadrants of operation for which the algorithm had been modified. The cost functions are analyzed for three operating conditions at each of the quadrants of interest. This augmentation was possible through two changes to the algorithm. First, the valve plate grooves and ports are symmetrical. The symmetry is kept with a rotational shift of 180° about the z-axis, see Figure 5.1. This means the displacement chamber will open up and close, in the exact same manner as a function of the shaft angle (ϕ); this allows making the assumption that quadrants III and IV in Figure 5.5 would be identical to I and II. The symmetrical valve plate design reduces significantly the number of design variables for the valve plate optimization and computational cost. Second, the cost functions and constraints count was increased to account for the additional motoring mode.

	$p_A < p_B$	$p_A > p_B$
Forward Swash plate angle > 0	II – Motoring	I - Pumping
Reverse Swash plate angle > 0	III - Pumping	IV - Motoring

Figure 5.5. Four quadrants of operation of general swash plate type axial piston machine (shaft rotation in a single direction).

The valve plate optimization scheme proposed in this thesis is represented as a flow chart in Figure 5.6. First, the flow chart starts with required performance parameters previously defined. The population size of the initial and following generations is determined by the number of design variables and quadrants of operation being optimized for the axial piston machine operation. Second, the population is generated randomly. Third, is the function evaluation block with green background. The function evaluation block was modified based on previous work (Kalbfleisch, 2015). The new block has an augmented set of function evaluations with the adequate objective functions and constraints to accommodate for the four quadrants of operation optimization. The number of functions evaluations per valve plate design is three operating conditions per quadrant of operation.

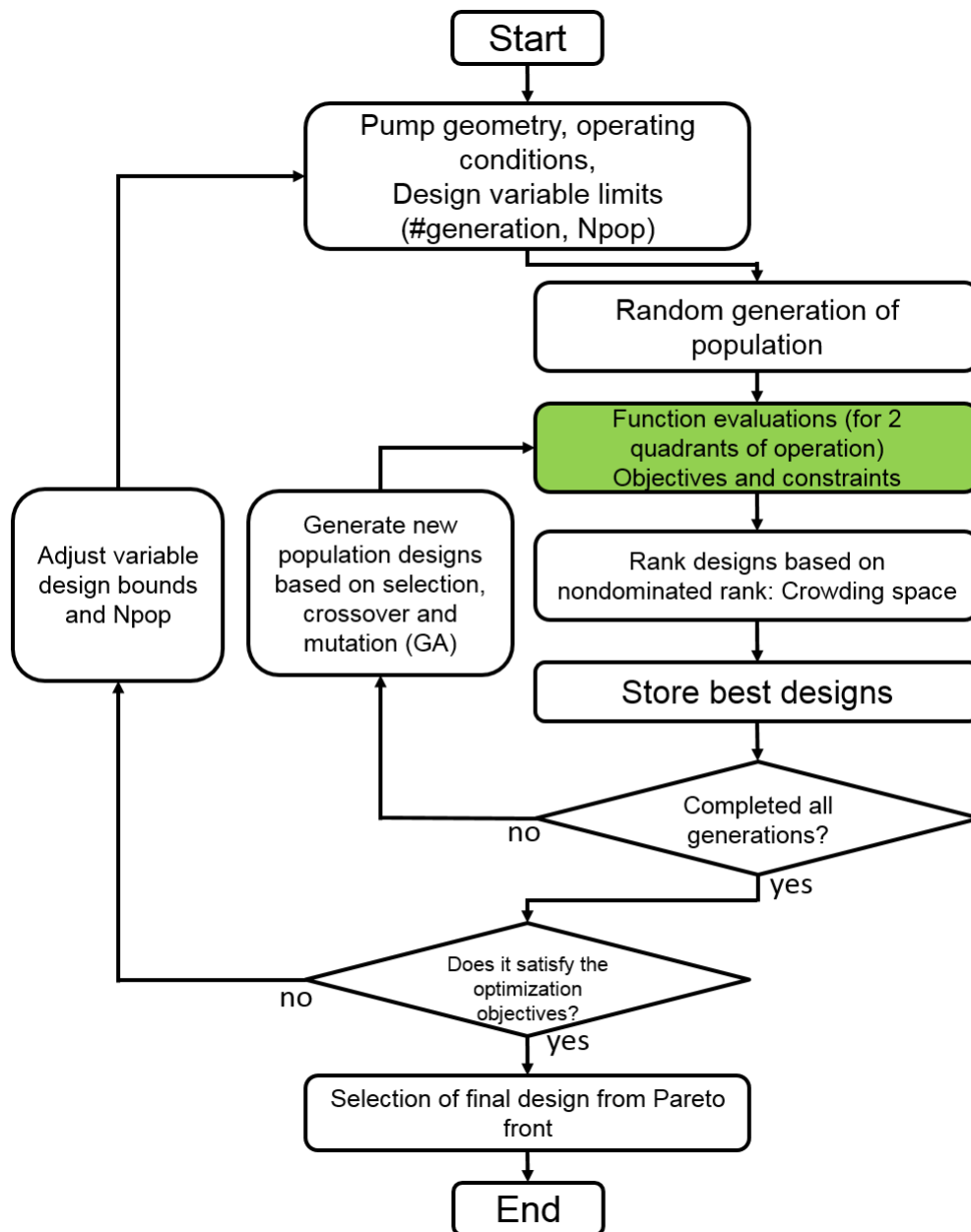


Figure 5.6. Valve plate optimization flowchart.

5.1 Objectives and constraints

The objective functions are defined in Table 5.1. The objective functions are to minimize the internal leakage, the flow ripple, ΔM_x , ΔM_y , and the mean M_x . The constraints are defined in Table 5.2. Each of the objective functions and constraints are evaluated for at least one operating condition in each of the quadrants of operation of the axial piston machine. The operating conditions are described in Table 4.3.

Table 5.1.: Objective functions for the valve plate optimization

Minimize:	Functions	OC
	$f_1(\bar{\mathbf{x}}) = \text{Leakage } [\%]$	3,6
	$f_2(\bar{\mathbf{x}}) = \Delta Q_{hp} \text{ [L/min]}$	1,2,4,5
	$f_3(\bar{\mathbf{x}}) = \Delta M_x \text{ [Nm]}$	1,2,4,5
	$f_4(\bar{\mathbf{x}}) = \Delta M_y \text{ [Nm]}$	1,2,4,5
	$f_5(\bar{\mathbf{x}}) = \overline{M_x} \text{ [Nm]}$	1,2,4,5

The effective flow out of an axial piston machine is Q_{HP} and the amplitude between the peaks of the effective flow is defined as the flow ripple. The flow ripple is the source for fluid borne noise source in axial piston machines. The swash plate moments M_x and M_y amplitude from peak to peak is the structure borne noise source. These amplitudes also referred to as ΔM_x , and ΔM_y are the objectives to be minimized. The overall reduction of ΔM_x , ΔM_y and ΔQ_{HP} minimize noise sources and increase machine reliability.

The optimization constraints are such that pump flow is at least sufficient at the operating condition for the volumetric efficiency test to build to the specified pressure and to keep the pressure spikes under a certain value at the peak test operating condition. It is desired to keep the mean moment about the x-axis (the pivoting axis of the swash plate) as close to zero to have the lowest control power requirement. The operating conditions are described in Table 4.3.

Table 5.2.: Constraints for the valve plate optimization

Constraints:

$g_1(\bar{x}) = \text{Max pressure} \leq \text{Max pressure spike [bar]}$	3,6
$g_2(\bar{x}) = \text{Min pressure} \geq \text{Min pressure spike [bar]}$	1,4
$g_3(\bar{x}) = \text{Volumetric Efficiency} \geq 1 [\%]$	1,4
$g_4(\bar{x}) = \text{Max}(\text{HP mean} - \text{set}) \leq 10 [\%]$	1,4
$g_5(\bar{x}) = \text{Min}(\text{LP mean} - \text{set}) \leq 20 [\%]$	1,4
$g_6(\bar{x}) = \overline{Mx} > 0$	2,5

5.2 Valve Plate Optimization Design Variables

The design variables utilized by the optimization algorithm define a nonlinear groove opening profile from the displacement chamber to the suction and discharge ports as a function of the shaft angle. An example of such a nonlinear opening area is shown in the following Figure 5.7. Figure 5.7 shows all the design parameters that define the groove opening profile.

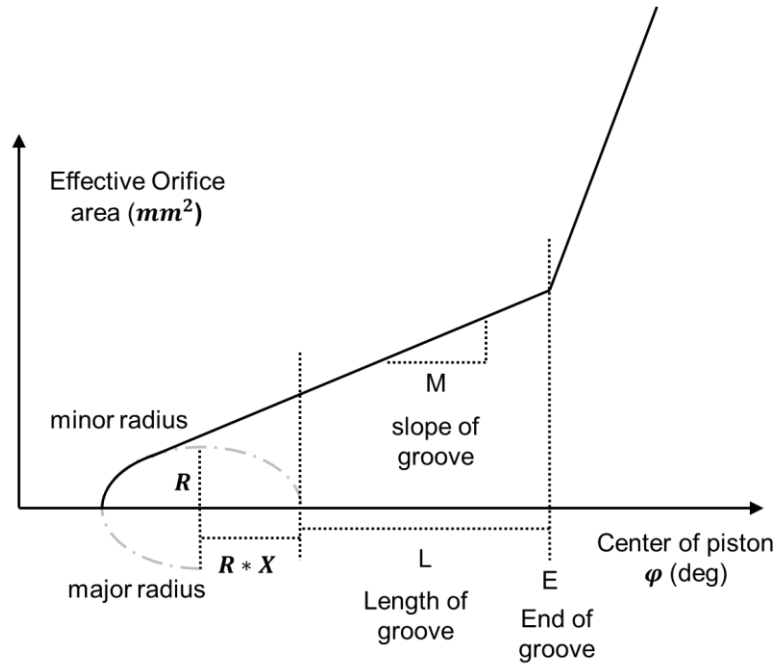


Figure 5.7: Nonlinear Groove Area Opening (Kalbfleisch, 2015).

The importance of this opening profile is due to the role it plays in the orifice equation, Eq. (3.2). The opening from the port to the suction port impacts the flow into and out of the displacement chamber which in turn impacts the pressure rise.

Operating conditions

The exemplary operating conditions defined for the valve plate optimization are shown in the following table. The operating conditions were defined in two operating quadrants; pumping and motoring. Three operating conditions are necessary per quadrant of operation. The max power (at nominal use) operating condition is where the objectives are evaluated for the optimization for the ΔM_x , ΔM_y , and ΔQ_{HP} . This operating condition corresponds to the following combination of characteristics max speed, max pressure and max displacement of the machine. The volumetric efficiency test is performed on the operating condition which corresponds to the following combination of parameters low speed, low displacement and max pressure. This specific combination of parameters creates the conditions with the highest internal. The peak test operating condition for the pumping mode is max speed, low pressure and max displacement. This is when the largest pressure spikes occur.

The other two operating conditions are mainly for constraints and to maximize the volumetric efficiency of the machine. The peak test operating condition is where the largest pressure spikes are found. The peak test evaluates the largest deviation from the max mean operating pressure and is constrained in the simulation. This operating condition corresponds to operating condition number 2 which has maximum speed, low pressure and max displacement. Similarly, the volumetric efficiency operating condition is the operating condition where the highest volumetric losses due to compressibility and internal leakage occur. This happens at low speed, max pressure and low displacement.

Table 5.3.: Operating conditions range for the axial piston machine

Operating condition	Mode []	Speed [rpm]	Δp [bar]	Displacement [%]
1	Pumping	max	max	max
2	Pumping	max	low	max
3	Pumping	low	max	low
4	Motoring	max	max	max
5	Motoring	max	low	max
6	Motoring	low	max	low

5.3 Design parameters settings

The main design parameters are taken from the preliminary phase design. The groove parameters need to be bounded by upper and lower limits. Also, the more the design space is reduced the larger number of designs closer to a desired value. In this example one of the design goals was to achieve low control effort (low mean M_x) and the value was required to be negative such that the swash plate would adjust towards zero displacement in case of a failure in the control system. The mean M_x objective allows for the design space to be reduced, since it is largely dependent on the location where the groove finishes. As mentioned in the previous sections for the 24 cc example a symmetric valve plate was utilized which means that only parameters for two different grooves are optimized. This reduces the population size for the genetic algorithm optimization leading to the boundaries described in Table 5.4.

Table 5.4.: Valve plate optimization variable boundaries

Variable	Lower Bound	Upper Bound	Units
e1	-15	-5	[deg]
e2	5	15	[deg]
l1	0	30	[deg]
l2	0	30	[deg]
r1	0	2	[mm ²]
r2	0	2	[mm ²]
x1	1	15	[unit less]
x2	1	15	[unit less]
m1	0.01	0.1	[mm ² /deg]
m2	0.01	0.1	[mm ² /deg]

5.3.1 Valve plate optimization example

The purpose of this section is to demonstrate the feasibility of virtual prototyping by using the methodology proposed in the previous sections. A sample 24 cc axial piston machine unit was utilized as canvas to feature this methodology's capabilities. The operating conditions on which this sample machine will operate are described in Table 5.5.

Table 5.5.: Operating conditions range for the axial piston machine

	Speed [rpm]	Δp [bar]	Displacement [%]
Min	500	30	20
Max	4000	430	100

5.3.1.1 Valve plate optimization example results

The simulation results from the NSGA II generate an evenly distributed Pareto front for the objective functions evaluated. The valve plate optimization realized for the 24 cc machine had the following characteristics (main parameters of the case study are described in section 4.4):

Table 5.6.: Valve plate optimization result parameters

Parameter	Value
Population size	3720
Number of generations	47
Total number of valve plates	174,840
Total function evaluations	1,049,040

All the objective functions are important in the valve plate optimization, but they might have a different degree of importance based on the designer's objectives. This is also highly dependent on which operating conditions the machine is going to be operated mostly.

In this optimization, a weighted sum was realized in the post processing phase to choose a final design. Figure 5.8 and Figure 5.9 show the objective values for the last 3720 valve plate designs of generation 47. Both figures are showing the evaluation of the objective functions for operating conditions 1 (max power) and 3 (volumetric efficiency).

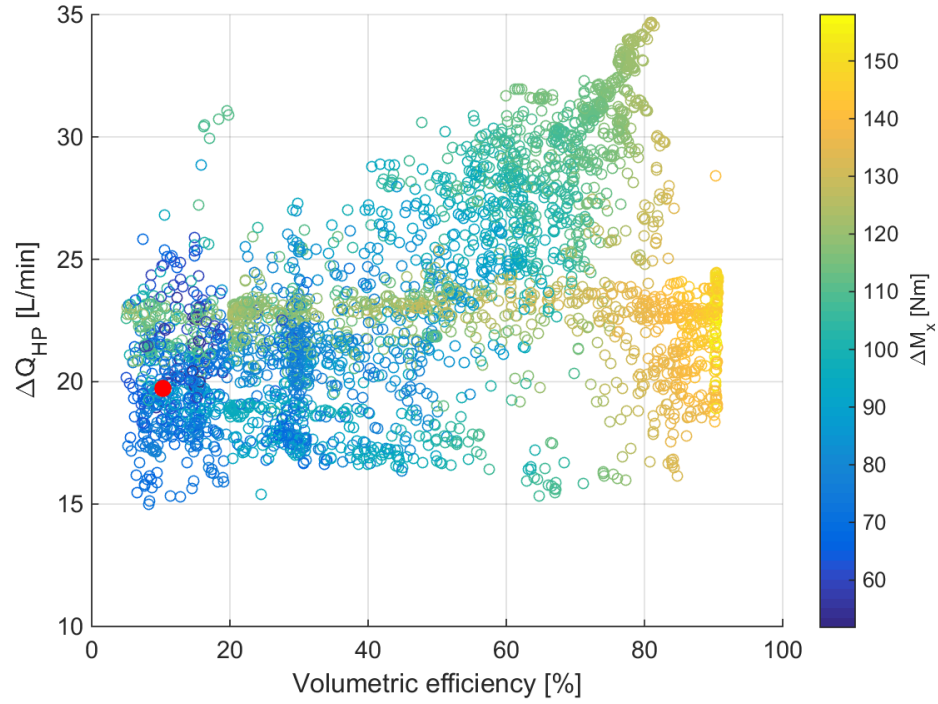


Figure 5.8. Valve plate optimization results, Vol. efficiency vs ΔQ_{hp} (OC1).

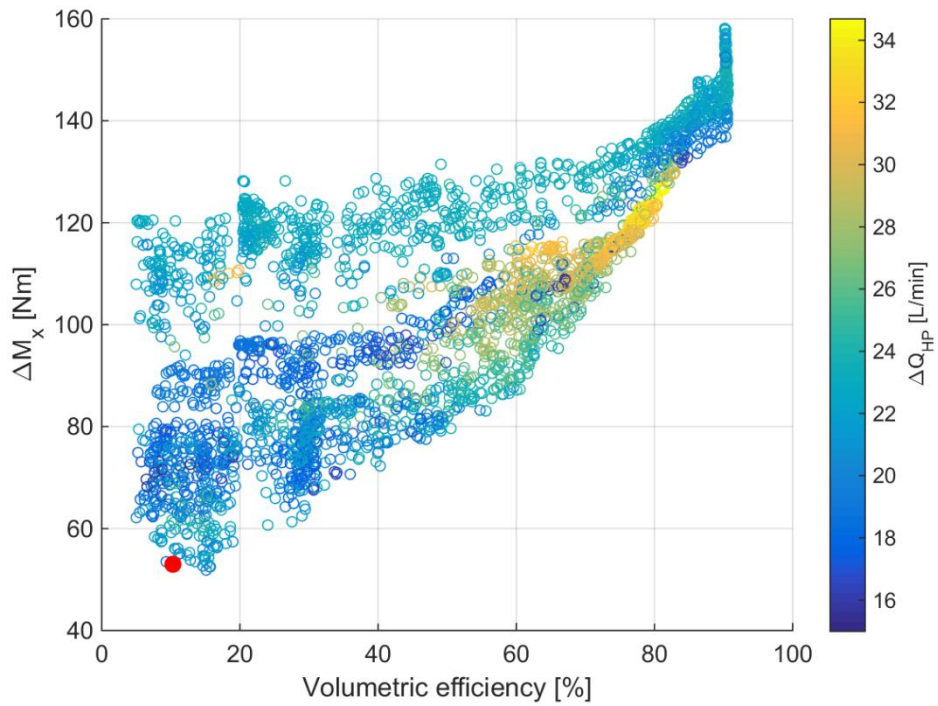


Figure 5.9. Valve plate optimization results, Vol. efficiency vs ΔM_x (OC1).

Figure 5.8 shows the volumetric efficiency plotted against the ΔQ_{hp} with the color representing the ΔM_x . It is shown that ΔQ_{hp} is all over the plot with respect to the volumetric efficiency, there is not a high correlation between the two. Figure 5.8 and Figure 5.9 show as high correlation between the volumetric efficiency and the ΔM_x . The lowest values for ΔM_x are only possible by compromising the volumetric efficiency of the axial piston machine at the volumetric efficiency operating condition. Both this figures also depict the recommended design out of this optimization with a red filled circle. It can be observed that it only has about 10% volumetric efficiency at the volumetric efficiency operating condition, but it performs good for both the ΔM_x and ΔQ_{HP} . Table 5.7. displays a summary of the simulation results that were discussed in the previous figures. It shows a total of four different valve plate designs. The first valve plate design has the highest volumetric efficiency of the four but it also has the highest values for ΔM_x and ΔQ_{HP} which coincides with Figure 5.8 and Figure 5.9. The second valve plate has the lowest flow ripple (ΔQ_{HP}) which has the lowest volumetric efficiency at the pumping mode. The third valve plate has the lowest ΔM_x which has a low volumetric. Finally, the recommended valve plate design shown in Table 5.7 compromises with the 16 objective functions and is within the constrain bounds in the optimization.

Table 5.7.: Valve plate optimization simulation results

Pumping								
	Vol Eff [%]	ΔQ_{HP} [L/min]	ΔM_x [Nm]	ΔM_y [Nm]	mean Mx [Nm]	ΔQ_{HP} [L/min]	ΔM_x [Nm]	ΔM_y [Nm]
Best vol eff	90.64	23.65	145.25	10.46	-7.64	17.55	85.86	5.62
Best ΔQ_{HP}	8.27	15.00	73.30	9.97	-9.35	4.73	35.82	8.01
Best ΔM_x	15.15	19.72	51.82	11.03	-4.78	10.07	24.88	7.85
Recommended	10.33	19.74	52.98	10.85	-4.82	10.63	30.19	9.87
Motoring								
	Vol Eff [%]	ΔQ_{HP} [L/min]	ΔM_x [Nm]	ΔM_y [Nm]	mean Mx [Nm]	ΔQ_{HP} [L/min]	ΔM_x [Nm]	ΔM_y [Nm]
Best vol eff	7.12	21.97	102.87	8.12	-26.14	17.70	86.92	5.72
Best ΔQ_{HP}	44.45	9.74	49.32	7.17	-28.26	4.26	29.14	4.76
Best ΔM_x	45.66	12.00	53.88	9.25	-24.92	9.84	25.94	8.16
Recommended	44.96	11.83	54.77	9.26	-24.95	9.58	27.16	8.03

As a last step after selecting a valve plate design based on a weight function. The valve plate design will be run for a large spread of operating conditions to observe how the valve plate performs over the entire range of operating conditions. Figure 5.10-Figure 5.13 show the simulation results for the exemplary recommended valve plate in Table 5.7

for the entire range of operating conditions in pumping mode. Figure 5.10 shows the volumetric efficiency of the valve plate with the lowest volumetric efficiencies for the max pressure. Additionally, the volumetric efficiency reduces with displacement and speed. Figure 5.11 shows the flow ripple (ΔQ_{HP}) with the flow ripple being highly dependent on the operating pressure. Figure 5.12 shows the amplitude of the moment M_x (ΔM_x) being pressure and displacement dependent, there is not a clear speed dependence. Finally, Figure 5.13 shows the mean M_x with most of the values being kept as a negative value, there are some which cross over to the positive domain because of the inertial forces of the piston/slipper assembly at high speeds and low operating pressures.

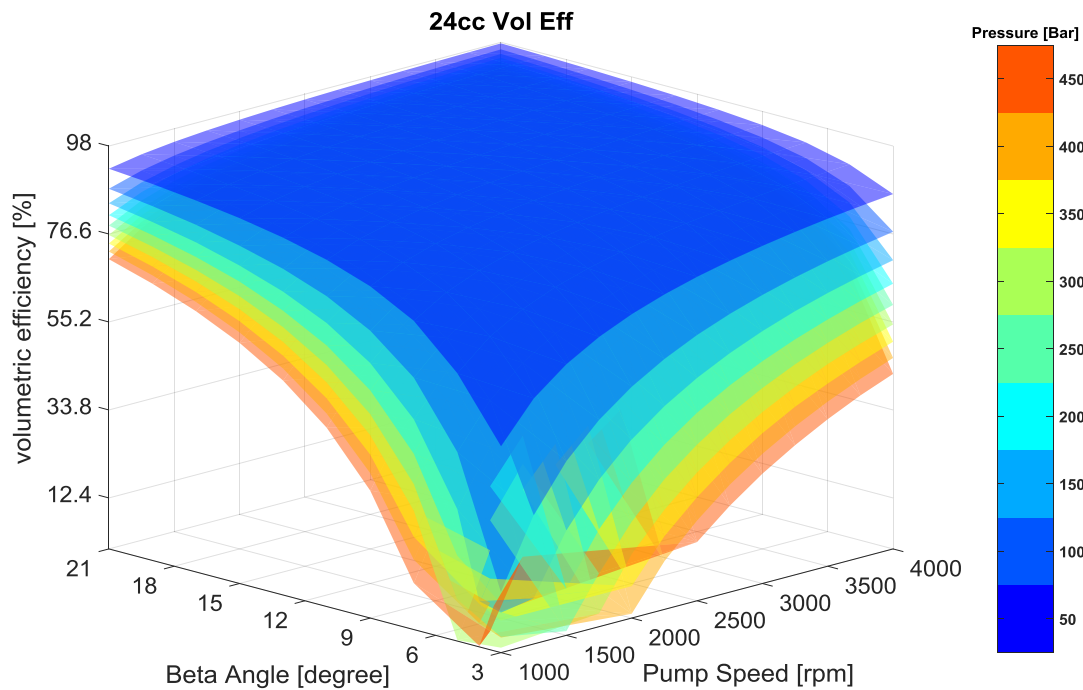


Figure 5.10. Recommended valve plate volumetric efficiency.

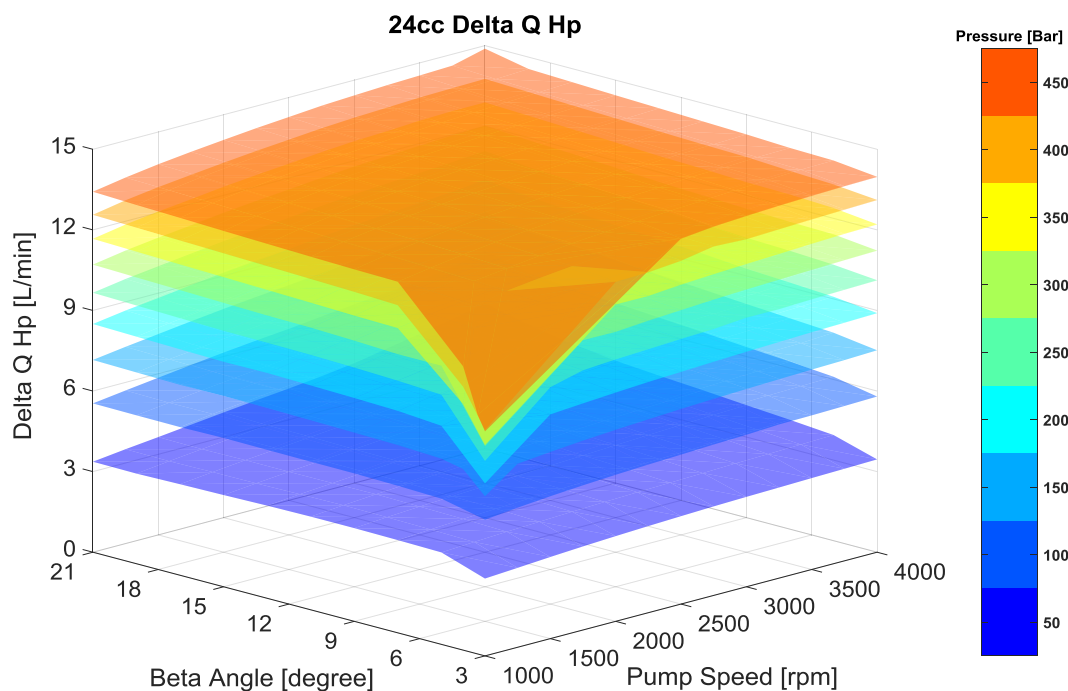


Figure 5.11. Recommended valve plate ΔQ_{HP} .

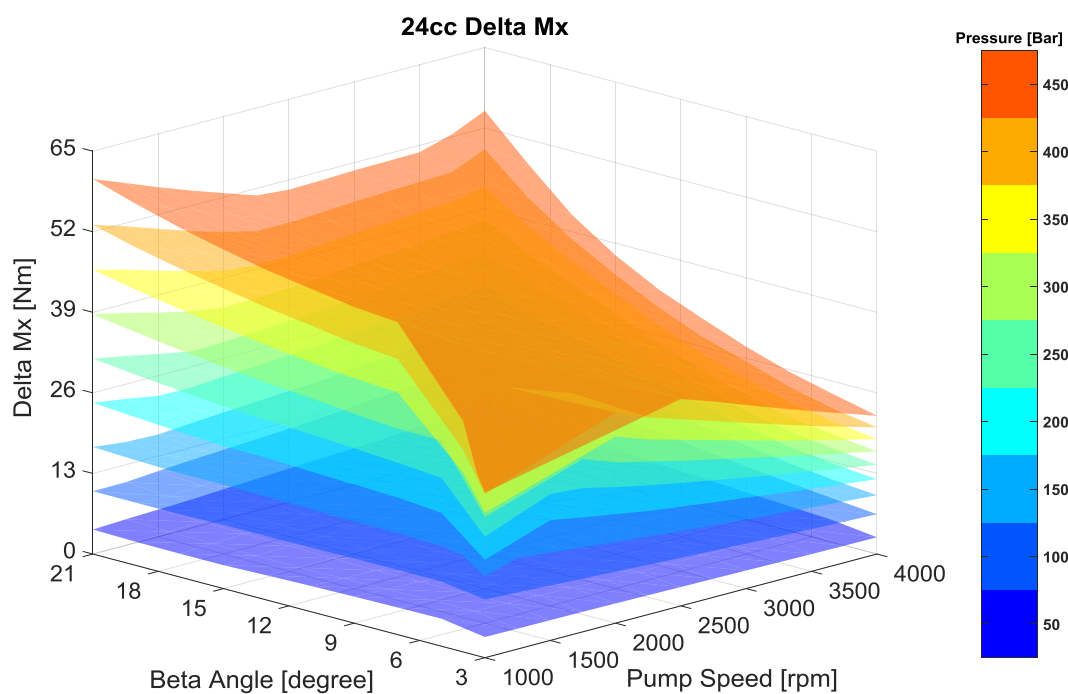


Figure 5.12. Recommended valve plate ΔM_X .

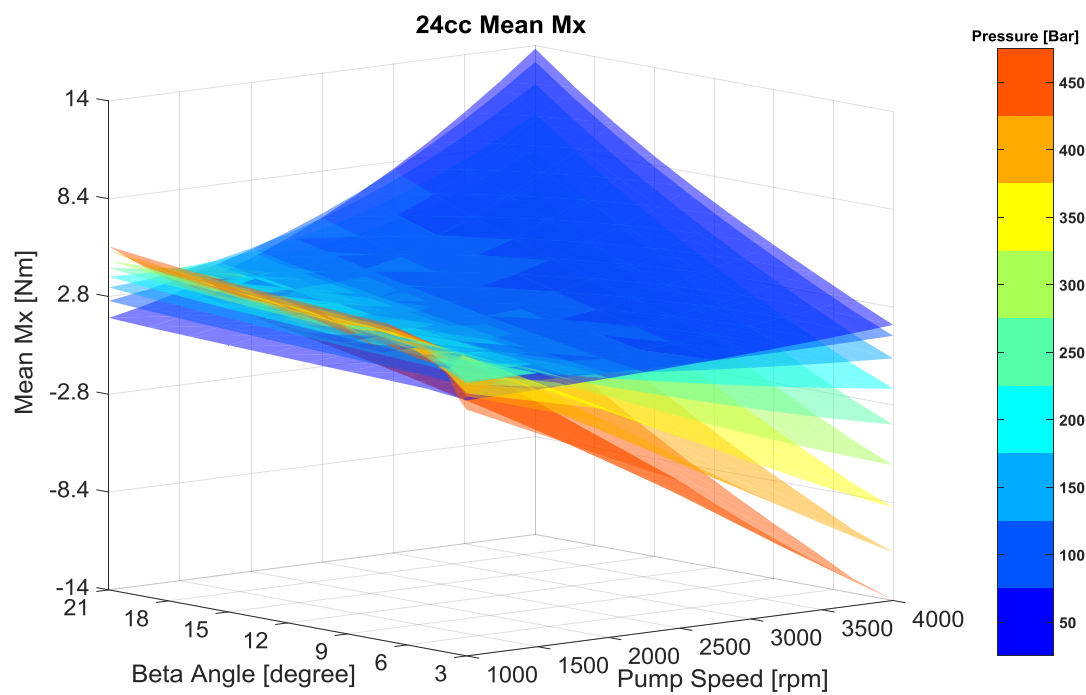


Figure 5.13. Recommended valve plate $\overline{M_x}$.

6. SOLID BODIES DESIGN AND FEM ANALYSIS

The solid bodies mechanical properties are of critical importance for the lubricating interfaces' design. The elastic deformations of the parts directly influence the performance of the lubricating interface. As an example of the impact of the elastic deformation of solid parts on the lubricating interfaces is shown in Figure 6.1. Figure 6.1 shows the fluid film between the cylinder block and the valve plate. The three-dimensional representation represents the scaled fluid film thickness in the order of microns. The color scale reflects the film thickness value in the lubricating interface. Figure 6.1 depicts three regions of extreme low fluid film thickness with the labels A, B, and C. The fluid film behavior is influenced by the elastic deformations of the cylinder block and valve plate/end case assembly. The low fluid film thickness is due to the large surface deformation of the valve plate due to pressurized delivery port and an inadequate geometrical design of the port.

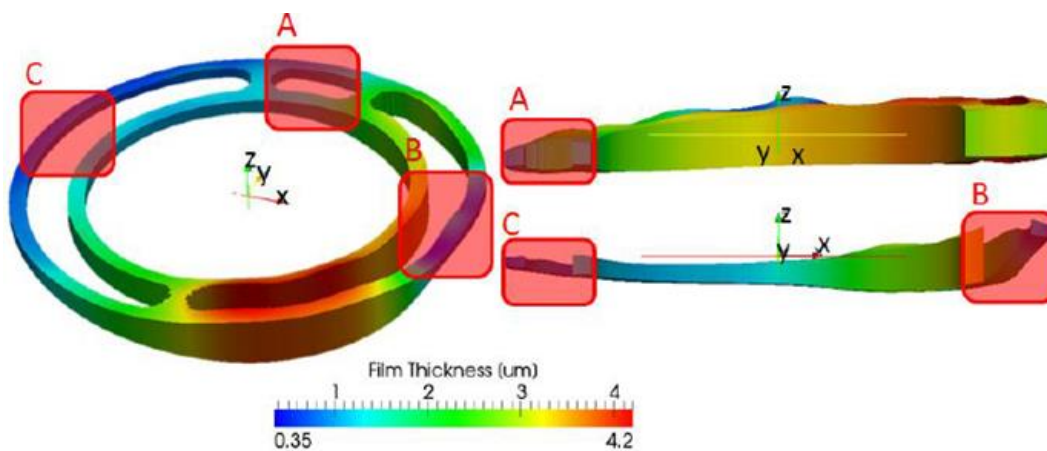


Figure 6.1. Cylinder block/valve plate interface fluid film thickness.

Figure 6.2 shows the corresponding surface deformations on the cylinder block and Figure 6.3 shows the surface deformation for the valve plate/end case assembly. The elastic deformations on the cylinder block aid to generate additional pressure through hydrodynamic effects resulting in larger load carrying ability and thus a more robust design. The valve plate/end case assembly large deformation impacts the lubricating interface in a negative manner, it results in excessive hydrodynamic pressure generation tilting the cylinder block towards the low-pressure (LP) side. The cylinder block tilt causes the low film thickness in the C region and the large deflection causes

the low film thickness in the B region. The low film thickness in the B region is uneven because of the surface deformation shape.

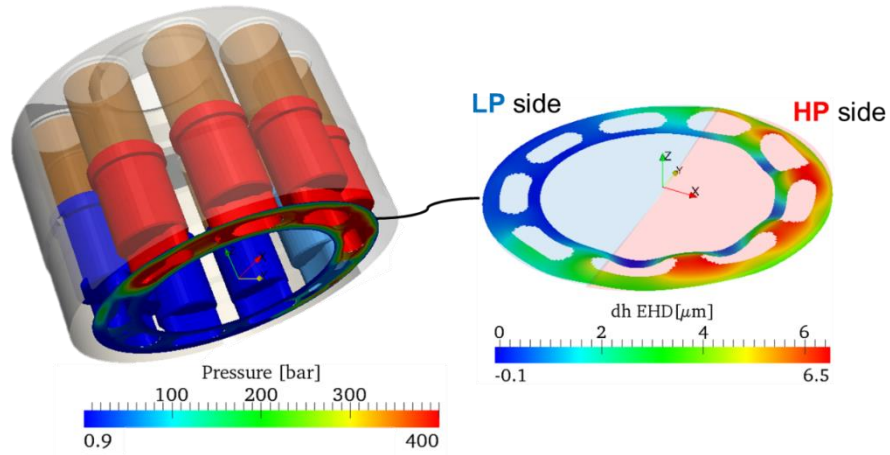


Figure 6.2. Cylinder block surface elastic deformation.

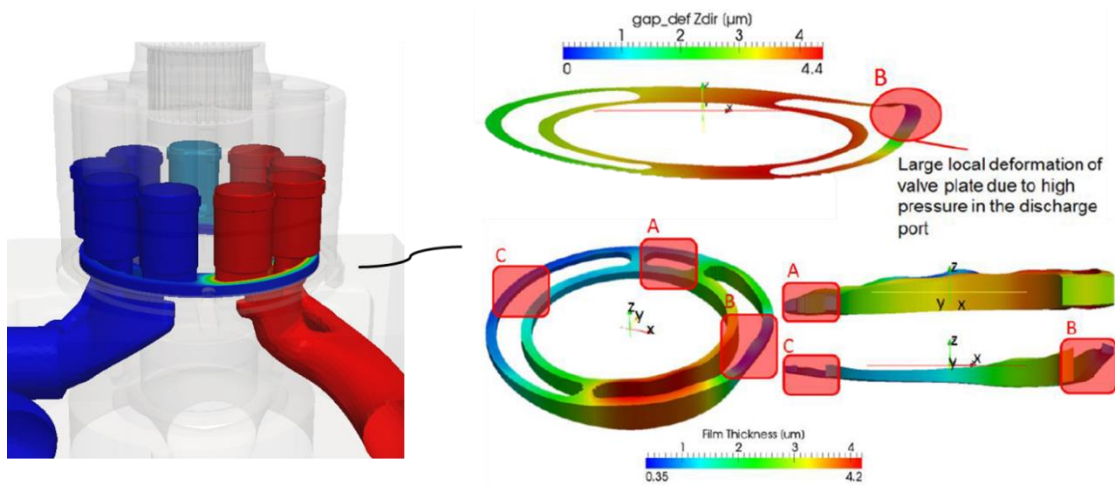


Figure 6.3. Cylinder block/valve plate elastic deformation.

6.1 Impact if the elastic deformation of the end case valve plate assembly

As already explained in the previous section, the end case design influences the behavior of the cylinder block/valve plate interface. To further investigate this, a case study was conducted by analyzing results from distinctive designs. Two distinct designs will be compared here. The case study was realized on a 24 cc axial piston machine swash plate type described in section 4.4. Figure 6.4 shows the valve plate volume and the suction and discharge ports surfaces for both designs. The first end case design has no ribs on the end case structure. The second has a distinctive structural addition a rib on the end case with ~8.6 mm in depth.

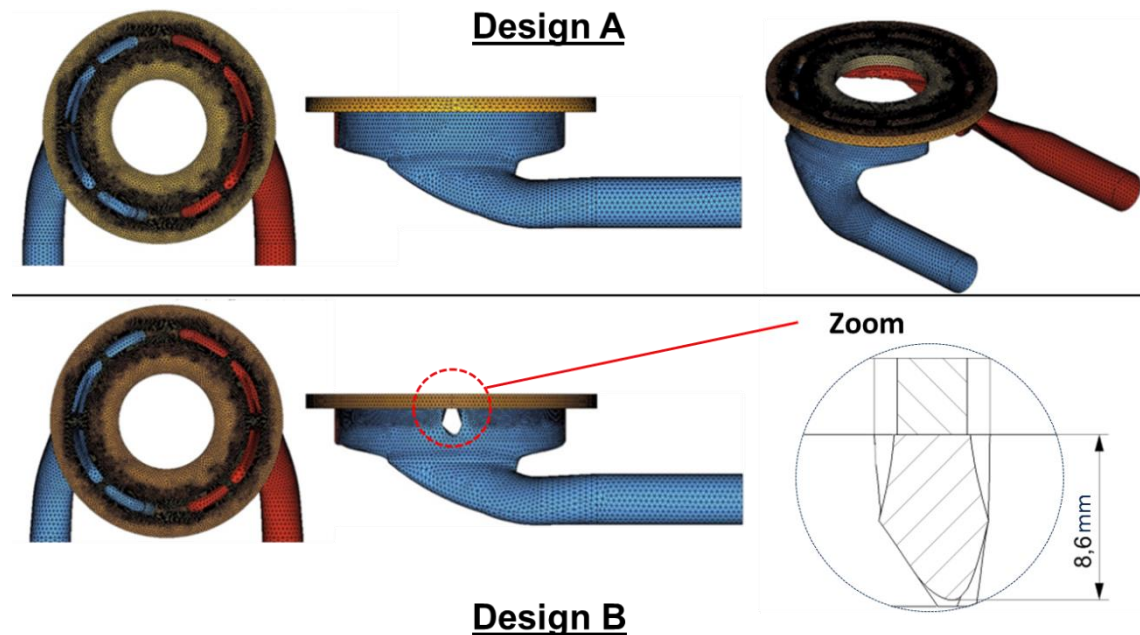


Figure 6.4. End case designs rib less and rib design shown in top and bottom, respectively..

The pressure boundary conditions on the cylinder block and end case/valve plate parts are defined as shown Figure 6.5. The gap surface is loaded with the pressure field calculated in the non-isothermal gap module. The suction and delivery ports labeled HP and LP are loaded with the pressures in the ports calculated in the pressure module. The displacement chambers in the cylinder block (DCi) are loaded with the pressure in the displacement chamber as a function of the shaft angle which is calculated in the pressure module.

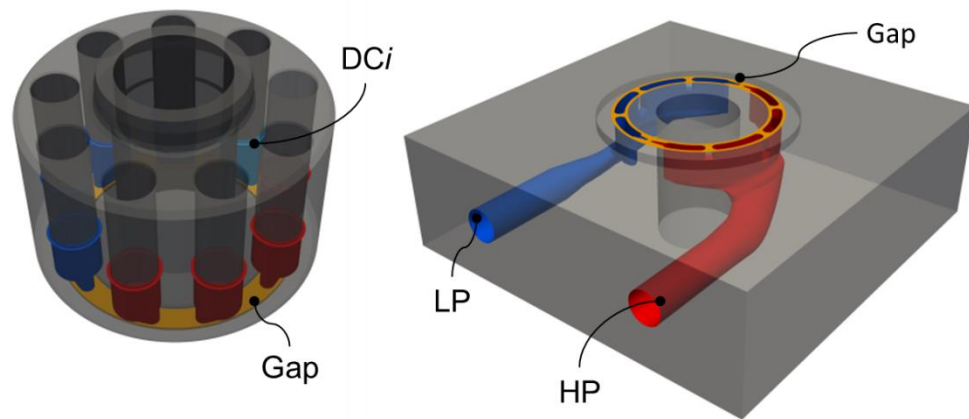


Figure 6.5. Pressure boundary conditions for the cylinder block valve plate interface.

Figure 6.6 shows the elastic deformations deformation of the valve plate running surface in z-direction due to pressure and thermal effects for a single operating condition (2500 rpm 350 bar at full displacement) for the two. This figure shows the elastic deformations for the design A on the top and for the design B on the bottom. The elastic deformations can be separated into the deformation due to pressure and thermal effects. The pressure deformation effects are labeled on the left as EHD deformation and thermal deformation in the middle section of the figure. The magnitude of the deformation is shown but what is more important for the lubricating interface is the relative deformation in the z-direction. This figure also shows that the biggest differences (circled in red) on the valve plate running surface deformation come from the pressure deformation of the solid bodies.

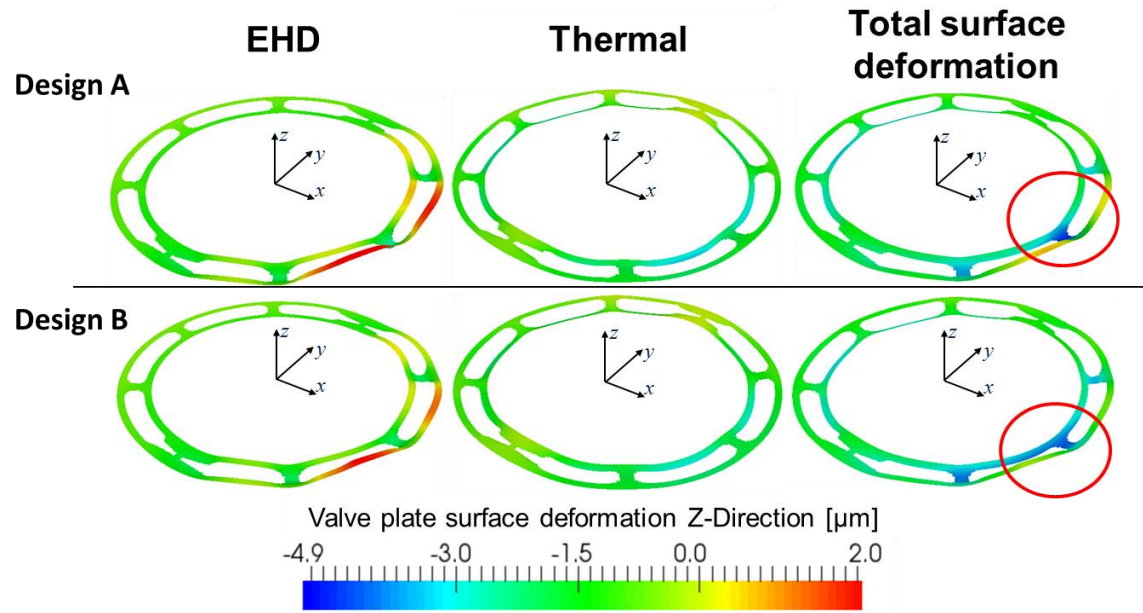


Figure 6.6. Valve plate surface deformation (2500 rpm 350 bar at full displacement).

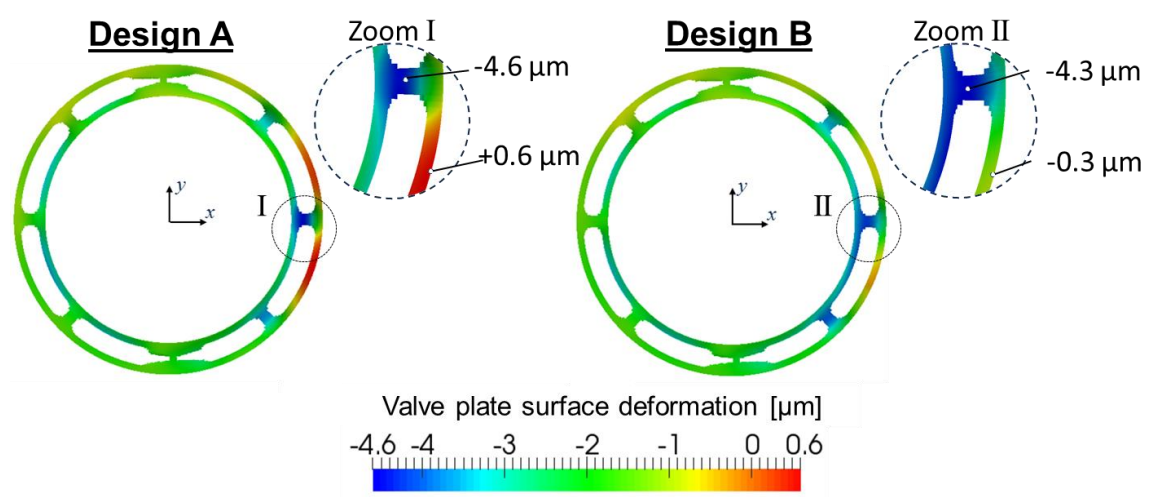


Figure 6.7. Valve plate surface deformation enlarged comparison (2500 rpm 350 bar at full displacement).

Figure 6.7 shows the same total elastic deformation of the valve plate running surface in z-direction due to pressure and thermal effects for the operating condition (2500 rpm 350 bar at full displacement) as in Figure 6.6 but now with a detail view of the areas with the largest differences between the two designs. The figure shows the deformation for design A on the left (a) and design B on the right (b). The zoom region for design A and design B are also shown. The deformation of the valve plate surface for design B is similar in the other areas, i.e. largest changes are only in the zoom area. The change in surface deformation is in the order Figure 6.8 shows the resulting 3D fluid film between cylinder block and valve plate for one selected angle of rotation for the same operating condition for design A and B. Design B shows an overall thicker fluid film than design A.

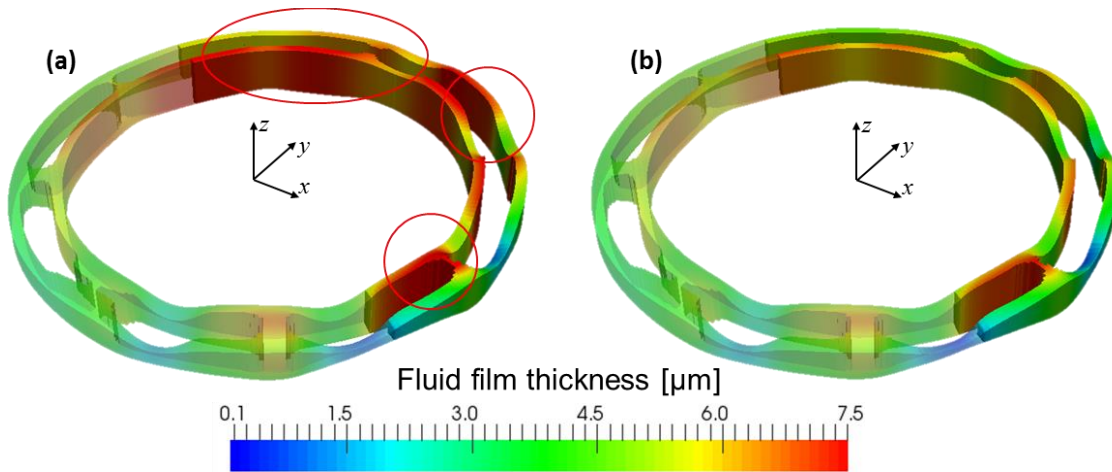


Figure 6.8. Cylinder block/valve plate fluid film thickness design A (a) and design B (b) (2500 rpm 350 bar at full displacement).

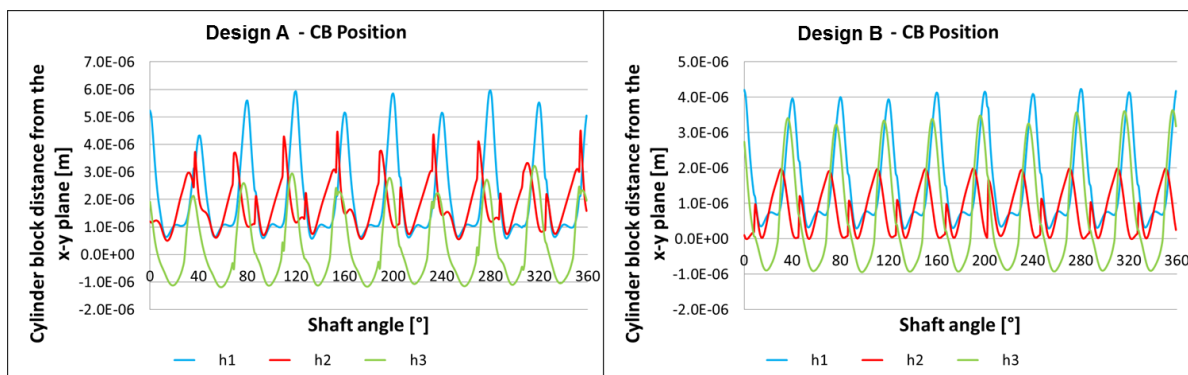


Figure 6.9. Fluid film thickness design A (left) and design B (right) (2500 rpm 350 bar at full displacement).

Figure 6.9 displays the position of the cylinder block throughout a full revolution with respect to the x-y plane for three reference points, P1, P2 and P3 as shown in Figure 2.6. The position of the block shows that the performance of the cylinder block/valve plate interface is unstable for design A, on the left of Figure 9. The unstable condition of the fluid film is due to the imbalance of external loads and fluid forces. Figure 6.8 (a) shows areas of thick film thickness regions circled. The imbalance surges from a larger component of hydrodynamic pressure from the wedge effect due to larger relative surface deformation ($\sim 2 \mu\text{m}$). Figure 7a shows a larger deformation on the high-pressure side of the valveplate which corresponds to the instability of the fluid film. The low fluid film thickness could also lead to metal-to-metal contact and excessive wear on the valve plate and cylinder block surfaces.

Figure 6.10 shows the simulation results for the calculated leakage flow, power loss due to viscous friction and total energy dissipation for the cylinder block/valve plate interface for both studied designs. The graph shows the differences between the two designs in terms of leakage flow and torque loss, where leakage flow for the second design decreased $\sim 20\%$ with respect the first and torque loss is increased by $\sim 7\%$. The decrease in leakage flow corresponds to the reduction in regions of high fluid film thickness shown in Figure 6.8 (b). These simulation results point towards completely different performance of the lubricating film.

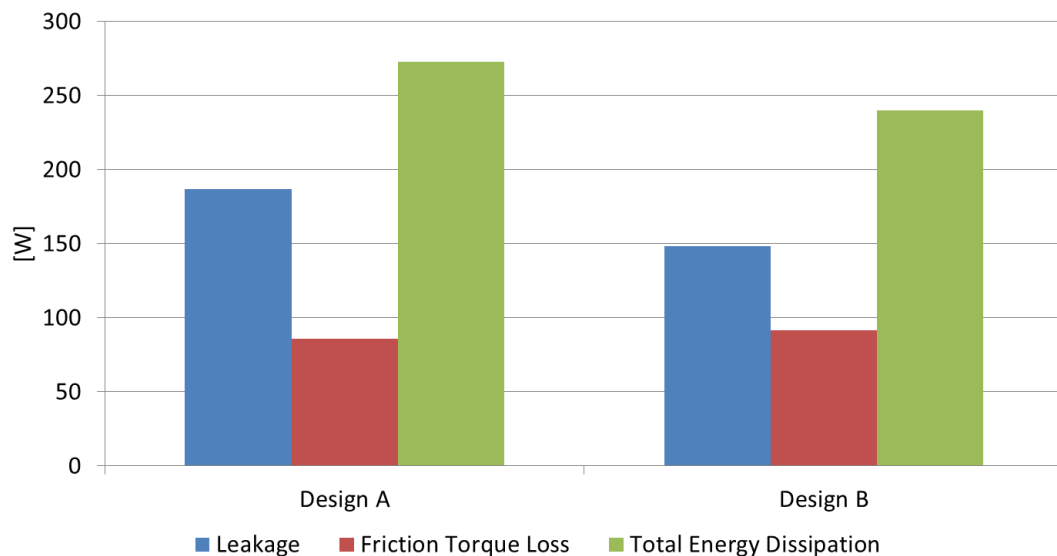


Figure 6.10. Simulation results (2500 rpm 350 bar at full displacement).

Figure 6.11 and Figure 6.12 shows similar simulation results for the two remaining operating conditions but here the effects from elastic deformation on the performance of the cylinder block/valve plate interface are reduced. Figure 6.12 shows the simulations results for operating condition 2500 rpm 350 bar at 50% displacement which shows a similar trend as 2500 rpm 350 bar at full displacement percentage wise these effects are less.

The simulation results showed better performance for design B in terms of fluid film stability and a thicker fluid film overall which ensures full fluid film lubrication therefore avoiding possible metal-to-metal contact leading to wear or machine failure. Structural designs and material properties on the valve plate/end case assembly which lead to a high stiffness are desired to allow for stable and reliable performance of the cylinder block/valve plate interface.

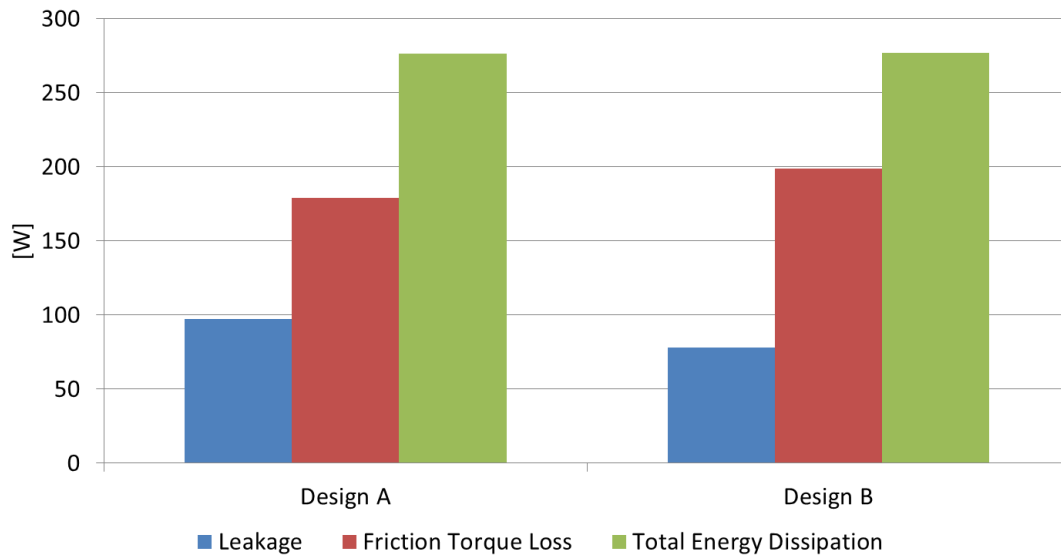


Figure 6.11. Simulation results (1000 rpm 100 bar at 50% displacement).

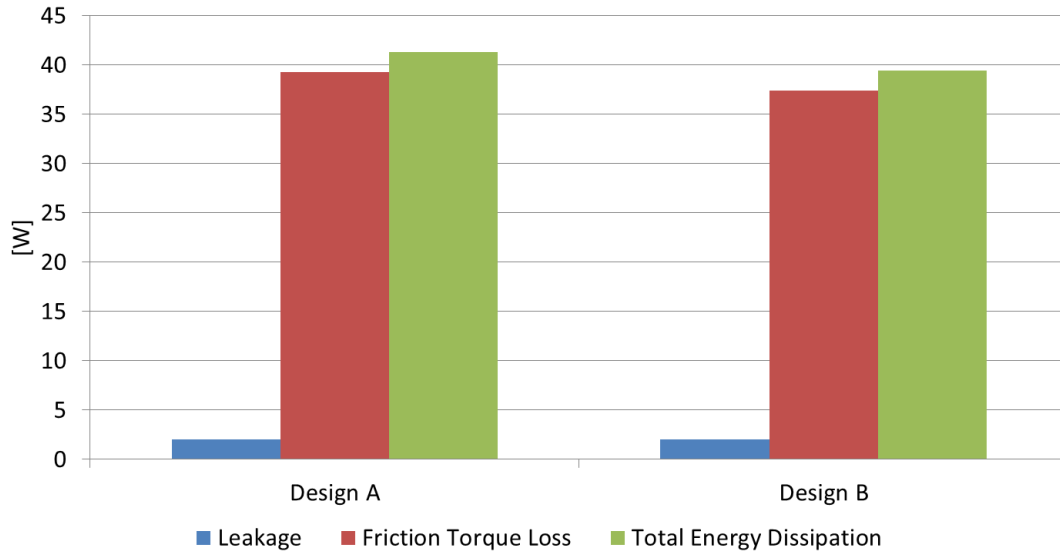


Figure 6.12. Simulation results (2500 rpm 350 bar at 50% displacement).

6.2 Solid bodies design methodology

The goal of this section is to describe the methodology proposed to design the components impacting the three lubricating interfaces. As previously mentioned the elastic deformations impact the lubricating interfaces. Also, the axial piston machine in virtual prototyping is designed to be as compact as possible, without compromising performance due to the lack of structure stiffness. Therefore, the machine parts are designed while considering the impact they have on the lubricating interfaces and size.

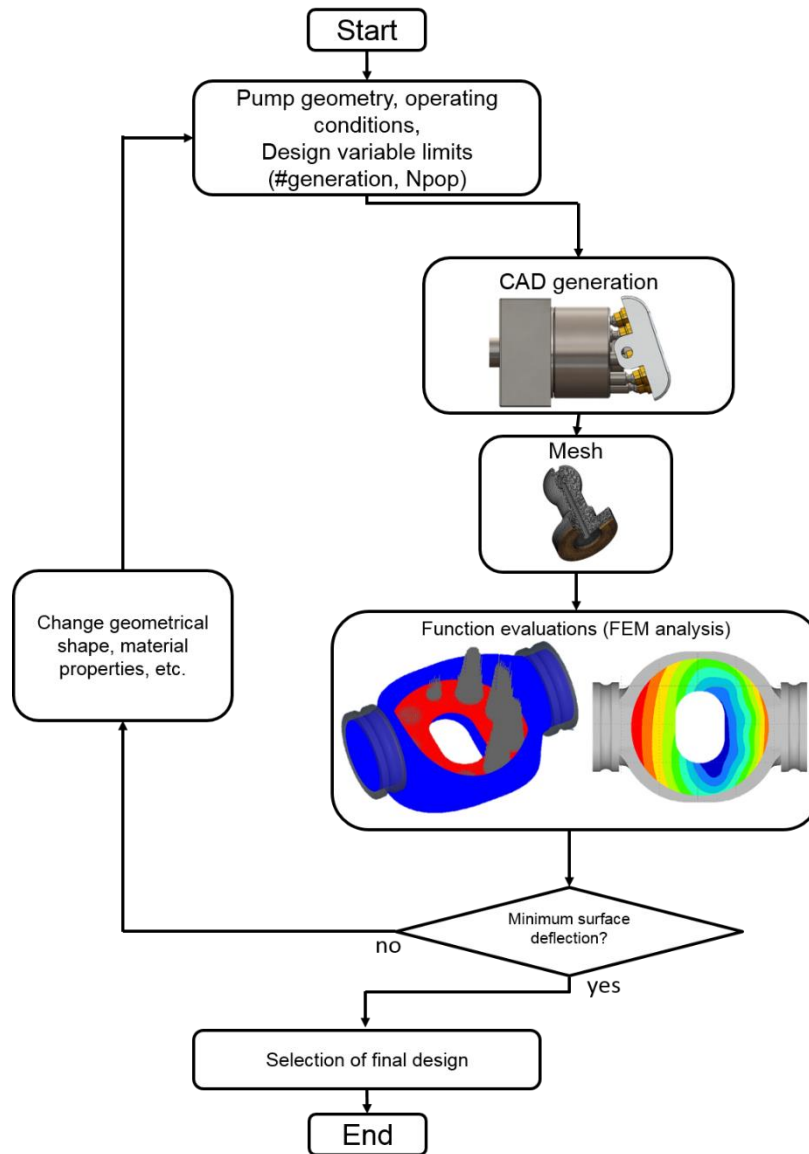


Figure 6.13. Solid body design methodology.

Figure 6.13 shows the flowchart for the proposed solid bodies design methodology. The process starts with the initial three-dimensional CAD models generated using the preliminary design base. In a second step the parts are to be discretized into three-dimensional meshes using a commercial software. As third step the mesh is assigned the corresponding boundary conditions on the solid part surfaces. The boundary conditions are set in similarly as it is described in Chapter 2 for the in-house FEM model. The pressure fields are extracted from the lubricating interfaces non-isothermal gap module by considering rigid bodies and a fixed parallel fluid film, an example of such a pressure field for the slipper/swash plate interface is shown in Figure 6.14. This pressure field is then applied to the sliding surface of the component as shown in Figure 6.15. Additionally,

the solid bodies are constrained to avoid rigid motion. These constraints are set by utilizing either zero Dirichlet constraint condition or inertia relief constraint method. Figure 6.15 shows the FEM analysis set up for the swash plate using the pressure calculated in the TEHD model and using zero Dirichlet constraints on the rolling bearing surfaces. The swash plate and valve plate/end case assembly utilize the zero Dirichlet constraint method since in the physical world they are mechanically constrained by the housing. The cylinder block, slipper and piston assembly are not mechanically constrained in the axial piston machine so an inertia relief method is applied.

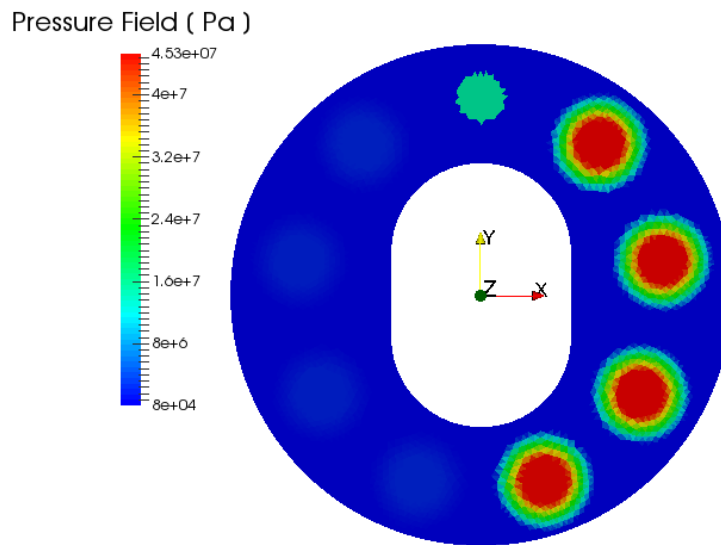


Figure 6.14. Example of swash plate pressure field calculated in the TEHD model.

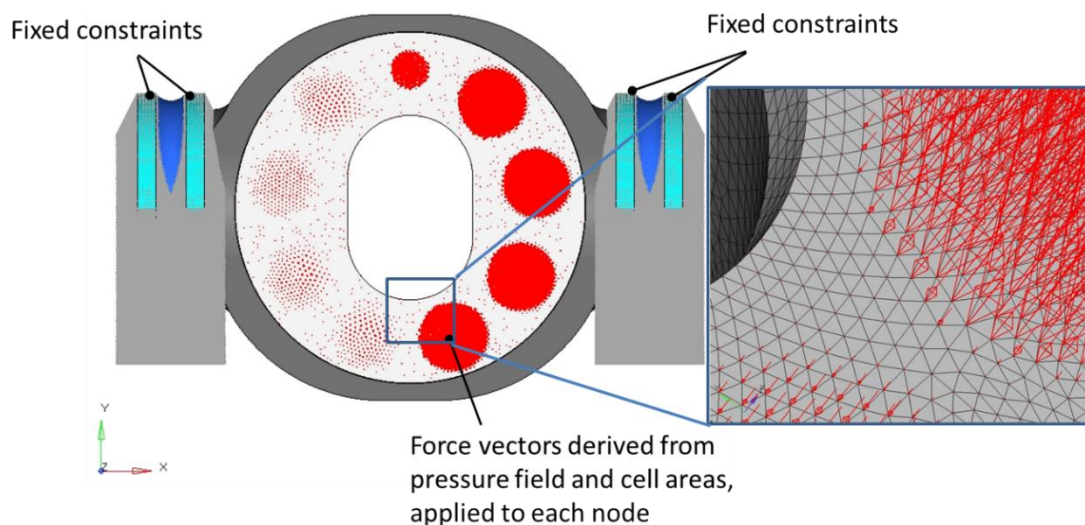


Figure 6.15. An example of the swash plate pressure boundaries applied to the three-dimensional mesh.

Once all the boundary conditions and constraints have been set to mimic the real mechanical system. The FEM analysis is conducted using a commercial software (in the example shown in Figure 6.15 Altair RADIOSS was utilized). The maximum relative deformation in the lubricating sliding surface is evaluated. The mechanical properties of the part need to be considered such as keeping the maximum stress below the material's yielding point. The relative surface deflection is the cost function because it is what impacts the lubricating interface, not the total deformation. The algorithm then compares the maximum relative deformation against the maximum relative deformation allowed defined by the designer. Figure 6.16 shows the von Mises stress distribution obtained from the FEM analysis in Altair, is important to maintain the stress magnitude below the yield strength of the selected material. Figure 6.17 shows the swash plate's sliding surface deflection in the z-direction due to the pressure loading imposed by the fluid film between the slipper and the swash plate. The maximum surface deflection is compared against the previous design and against the designer's requirements. If the design doesn't satisfy the conditions of being the smallest deflection and being below a specific value, the geometry or material selection are modified accordingly. An example of a geometrical design is adding geometrical features such as the rib in the previous section which added stiffness to the end case for the cylinder block/valve plate interface. Once the design has achieved the desired relative surface deflection the design can then be used in the following steps of virtual prototyping. This process might need to be repeated if in the following step the maximum relative deformation is found to be not sufficiently low.

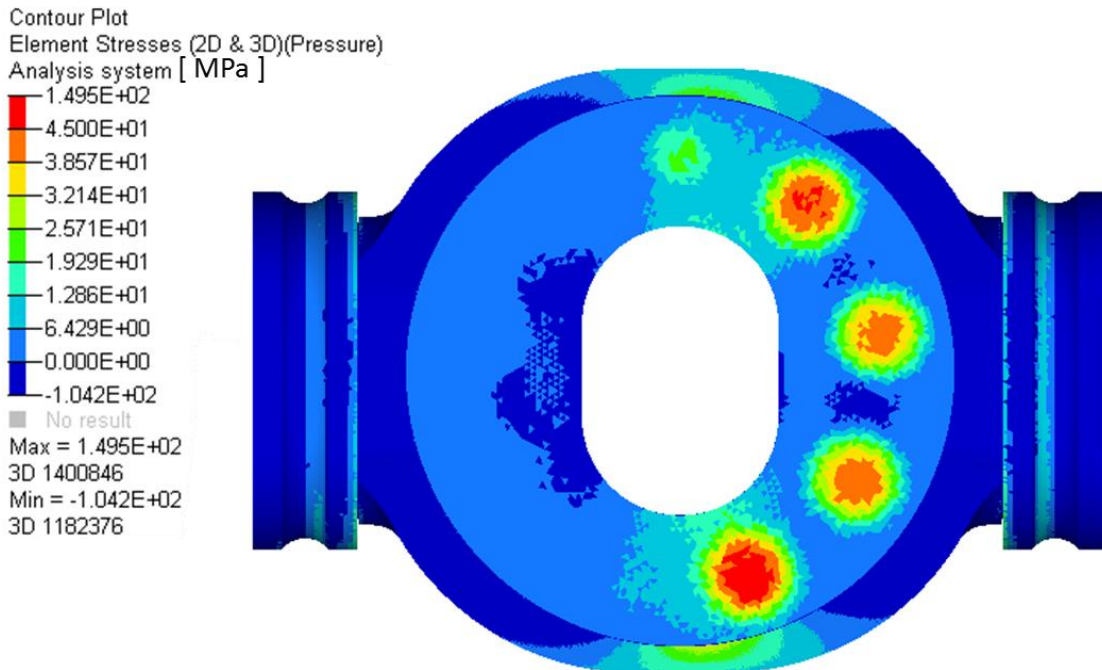


Figure 6.16. Example of swash plate von Mises stress distribution.

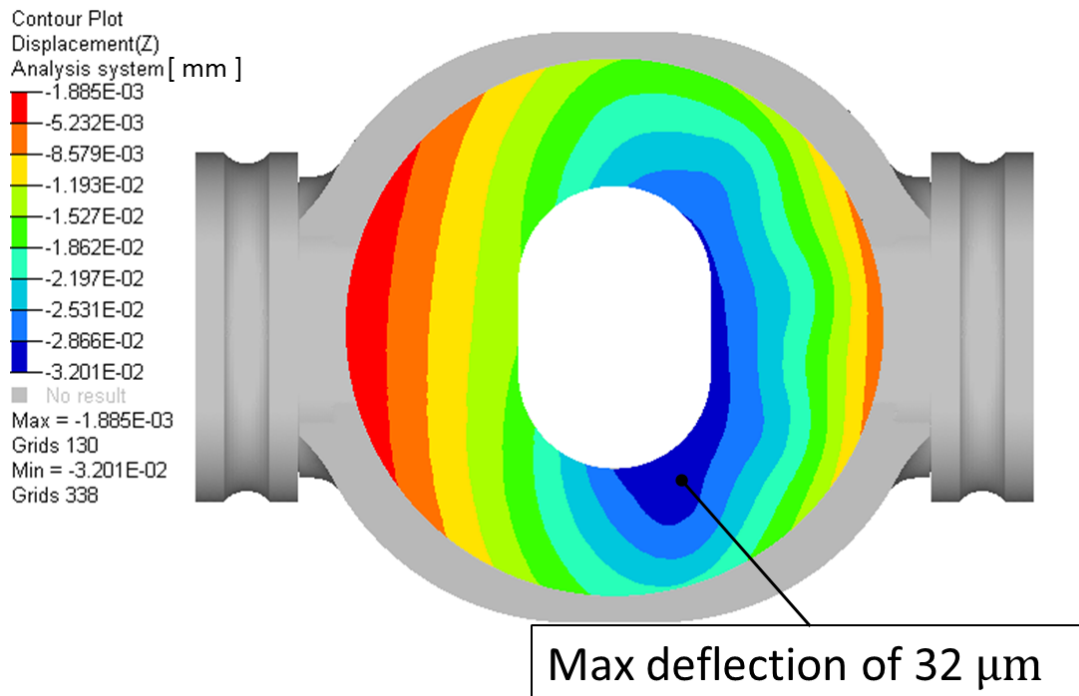


Figure 6.17. Example of swash plate sliding surface deformation in the z-axis.

7. VIRTUAL PROTOTYPING FOR LUBRICATING INTERFACES

The main contribution of this dissertation is the proposed methodology for the design of the main lubricating interfaces described in this section. The objectives during the design process of the lubricating interfaces is to ensure load carrying ability to avoid mixed lubricating and to maximize overall efficiency by minimizing leakage flow and viscous friction. These objectives are quantified over the desired range of operating conditions. Figure 7.1 shows a flowchart which details the methodology proposed in this thesis for the design of the lubricating interfaces. As mentioned in the previous section the preliminary design phase needs to occur before starting the virtual prototyping of the lubricating interfaces. After, As mentioned in section 4.1, the following parameters will be calculated:

- Fluid film thickness between the piston and the cylinder bore, the cylinder block and the valve plate, and the slipper and the swash plate.
- Pressure fields in the fluid film in the lubricating interfaces.
- Leakage flows in all three lubricating interfaces.
- Energy dissipation due to viscous flow in all three lubricating interfaces.
- Temperature distributions in the fluid film and main pump parts (cylinder block, piston, valve plate, slipper, swash plate, and end case).
- Surface deformations of cylinder block, piston, valve plate, slipper, and swash plate due to pressure and thermal loading of these parts.

After the preliminary design analysis of all three lubricating interfaces, the lubricating interface design process described in Figure 7.1 can be started. The lubricating interface design process starts with the definition of: the materials utilized for the cylinder block, the valve plate and end case assembly, the slipper, the swash plate and the piston; the operating conditions which will be used for the function evaluations of the objectives and constraints; the fluid properties as a function of pressure and temperature; and the variable bounds for the design of experiments.

The next step is to generate a design of experiments (DOE). The design parameters to be varied are different for each of the lubricating interfaces and will be discussed in more detail later. Once,

the design parameters have been selected the DOE is generated. For the DOE generation, there are multiple options: full factorial, fractional factorial, Latin hyper cube sampling, etc. The selection of the DOE method will depend on the number of design variables and operating conditions being treated at a time and the computational power at hand. The following step is to generate the new CAD models based on the design parameters populated by the DOE.

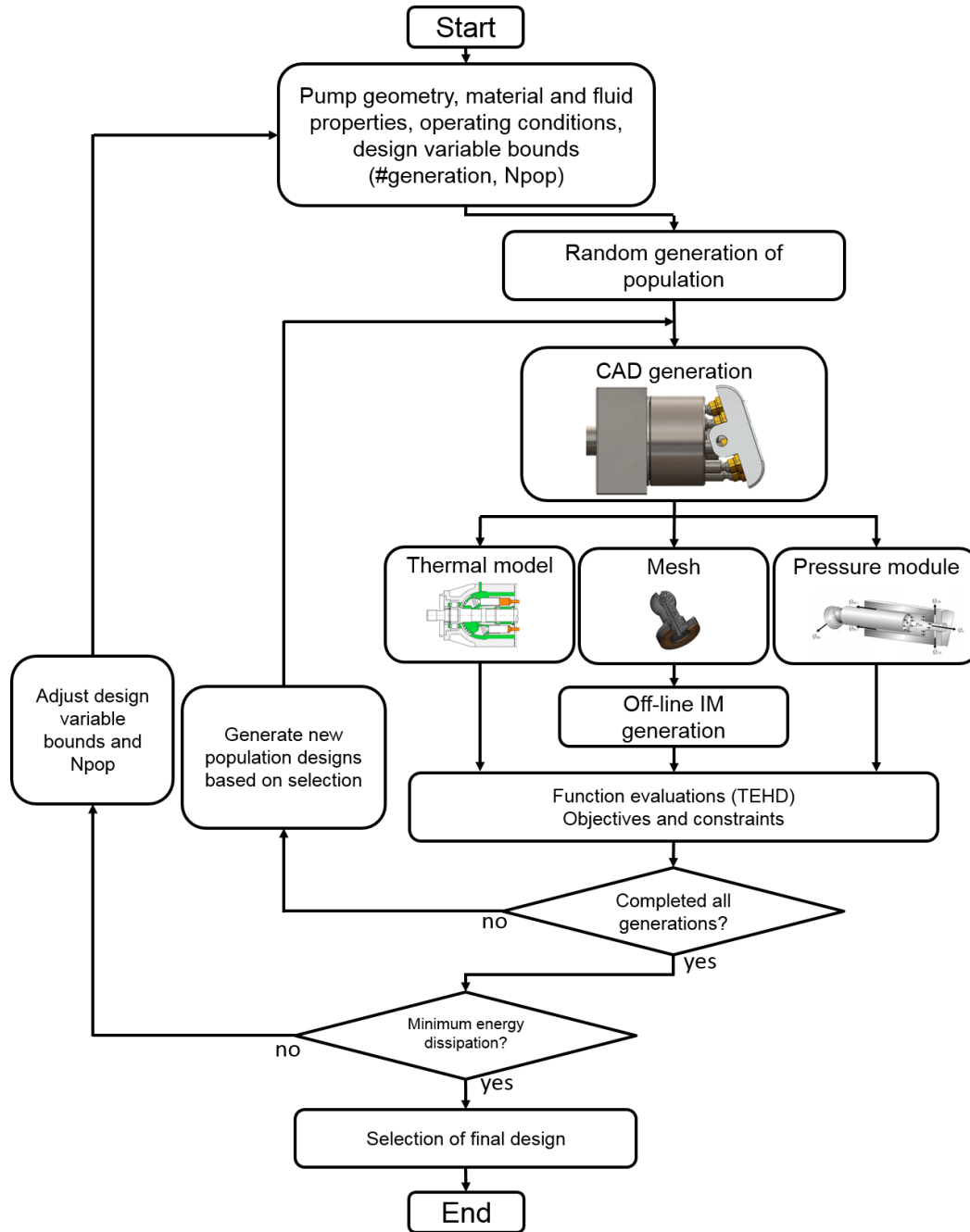


Figure 7.1: Lubricating interfaces general design methodology.

The following step makes use of the computational models described in Chapter 2. The instantaneous pressure in the displacement chambers is calculated in the pressure module. The CAD models are meshed to be utilized in the pressure and thermal deformations, as well as for the calculation of the temperature distribution in the solid bodies. The three-dimensional CAD models are discretized into three-dimensional mesh utilizing tetrahedral elements in commercial software. Once the mesh has been generated the corresponding influence matrix needs to be calculated off-line to be able to predict elastic surface deformations due to pressure in the fluid film. The thermal model is utilized to predict the discharge port and the case volume temperatures, utilizing the information from the operating conditions, the pressure module and the TEHD if it is not the first iteration.

Next, the DOE for the lubricating interfaces are evaluated by running simulations using the thermo-elastic hydrodynamic model (TEHD). The simulation results yield the fluid film thickness, pressure field distributions, temperature field distributions, leakage flows, surface deformations due to pressure and thermal effects, and the energy dissipation due to viscous flow for all three lubricating interfaces. The energy dissipation is the cost function to be minimized and the constraint is to maintain functionality by limiting the allowed areas of minimum fluid film thickness which can result in metal-to-metal contact, therefore failure of the prototype.

The selected design parameters can be optimized by a variety of optimization schemes on a case by case scenario. A response surface or surrogate model method is recommended since it reduces the count of function evaluations significantly. The function evaluations of the lubricating interfaces are of high computational cost. Therefore, a response surface approach coupled with a genetic algorithm reduces the time spent on the virtual prototyping. A sequential approximate method can be coupled with the surrogate model approach. This method will refine the area near the optimum design space. For this design refinement, the lower and upper bounds for the DOE are adjusted and the function evaluations are analyzed using the TEHD model and a second surrogate model is generated. Once the response surface method has finalized the function evaluation for the optimal design should be rerun using the TEHD to validate the surrogate model simulation results. Also, if the number of design variables is small a full factorial design approach is feasible and it doesn't require any additional optimization schemes. The minimum energy

dissipation design is compared against the desired minimum energy dissipation desired for the axial piston machine. If the design achieves the desired performance, the design process is completed successfully.

7.1 Material selection

The material selection of the following components: cylinder block, the valve plate and end case, the slipper, the swash plate and the piston are critical for the behavior of the lubricating interfaces. The virtual prototyping methodology enables the designer to evaluate and analyze the impact on the lubricating interface. The physical properties of the materials impacting the function evaluations of the lubricating interfaces are shown in Table 6.1. The physical properties of the material are important because this change how the components will deflect under pressure and thermal loadings. The TEHD model described previously, accounts for elastic deformation of the solid bodies when it evaluates the performance of the lubricating interfaces. The elastic deflections will result in a modified thin fluid film geometry with additional or a diminished hydrostatic/hydrodynamic fluid pressure. The computational based methodology presented in this dissertation allows for the exploration of a larger design space. New materials can be considered to replace the traditional steel alloys, gray iron or brass materials. The material selection and the FEM analysis phase described in section 6.2 allows for materials which were considered inappropriate for testing to be evaluated in the virtual prototyping framework.

Table 7.1.: Material properties influencing the lubricating interfaces' behavior

Description	Symbol	Unit
<i>Young's modulus</i>	E	[Pa]
<i>Poisson's ratio</i>	ν	[-]
<i>Density</i>	ρ	[kg/m ³]
<i>Thermal conductivity</i>	λ	[W/mK]
<i>Coefficient of linear thermal expansion</i>	α	[-]

Figure 7.2 shows an example of a typical material selection for valve plates of brass with steel backing and the end case material is ductile iron. Additionally Figure 7.3 shows another bimetal component, in this case the material composition of an example slipper, which is made of steel with a layer of brass for the sliding surface, these Figures show the materials selected for the case study described in section 4.4.

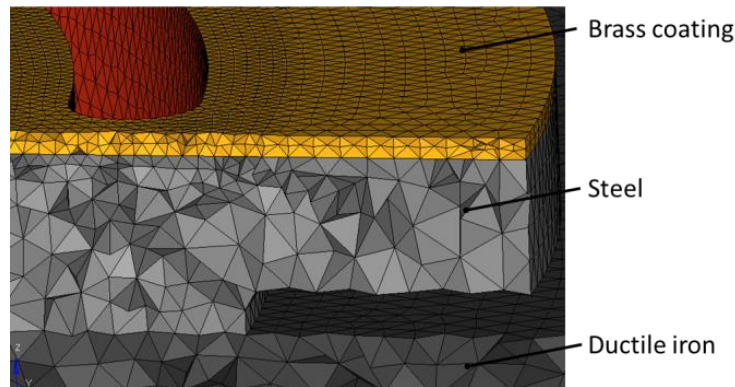


Figure 7.2. Cross section of bimetal valve plate mesh.

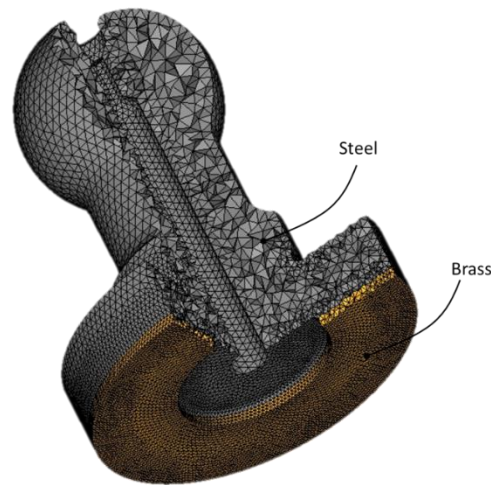


Figure 7.3. Cross section of bimetal valve plate mesh.

7.2 Operating conditions

Axial piston machines normally operate in a broad range of operating conditions. The decision of which operating conditions are required for a machine is made at the beginning of the design process. The selection of the operating conditions which will be evaluated for the design of the lubricating interfaces is of paramount importance to minimize the computational effort while considering the crucial operating condition points for all three lubricating interfaces. The computational cost is directly proportional to the number of operating conditions which will be considered. The critical operating conditions are not all the same for the three lubricating interfaces, the cylinder block/valve plate, slipper/swash plate and piston/cylinder interface behave differently at different operating conditions. The cylinder block/valve plate and the slipper/swash plate interfaces have difficulties to carry the external loads exerted on the sliding components at low

pressure operating conditions, since both have a high hydrostatic component. The piston/cylinder interface critical operating condition is at low relative sliding velocities at high pressures, which correspond to low displacements and low rotating speeds. The corner operating conditions are critical and must be evaluated to approve a final design. The lubricating interfaces are designed for maximum performance at max power operating condition (max pressure, max speed and full displacement) and at the operating conditions on which are the most critical for each individual interface. The max power operating condition represents the highest energy dissipation from the three lubricating interfaces. Nominal operating conditions at which the axial piston machine operates most frequently should be added into the design process. An example of a possible set of operating conditions to be utilized for the function evaluations in the virtual prototyping process is described in Table 7.2. This table includes the eight corner operating conditions and in additions there are two extra operating conditions at more moderate conditions. The last ones can be varied depending on the application of the axial piston machine.

Table 7.2. Operating conditions

Operating condition	Speed [rpm]	Δp [bar]	Displacement [%]
1	max	max	max
2	max	max	min
3	max	min	min
4	max	min	max
5	min	max	max
6	min	max	min
7	min	min	min
8	min	min	max
9	min	max	moderate
10	moderate	max	max

7.3 Cylinder Block/Valve Plate Interface Design Variables within Virtual Prototyping

The cylinder block/valve plate interface is shown in Figure 7.4. This section describes the design variables considered within the virtual prototyping framework.

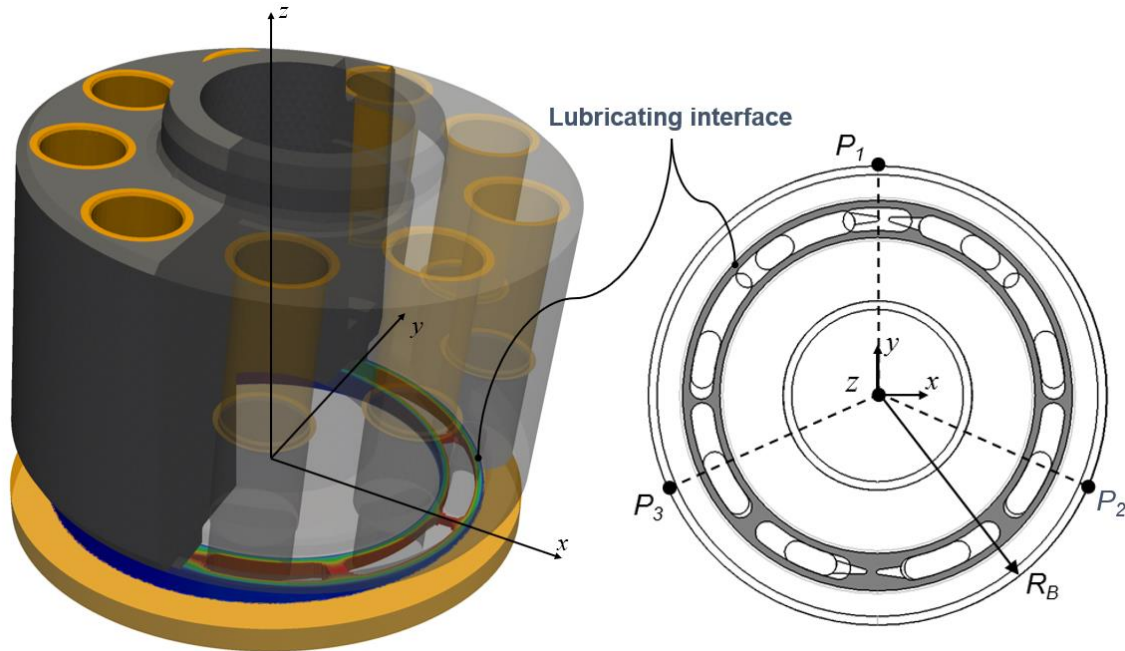


Figure 7.4. Cylinder block/valve plate interface schematic.

The design parameters that are considered for the cylinder block/valve plate interface are the sealing land dimensions, cylinder block length ($length_B$), cylinder block channel length ($length_{CanalB}$), end case design, and material selection. Figure 7.5 shows the cylinder block length ($length_B$) and the length ($length_{CanalB}$).

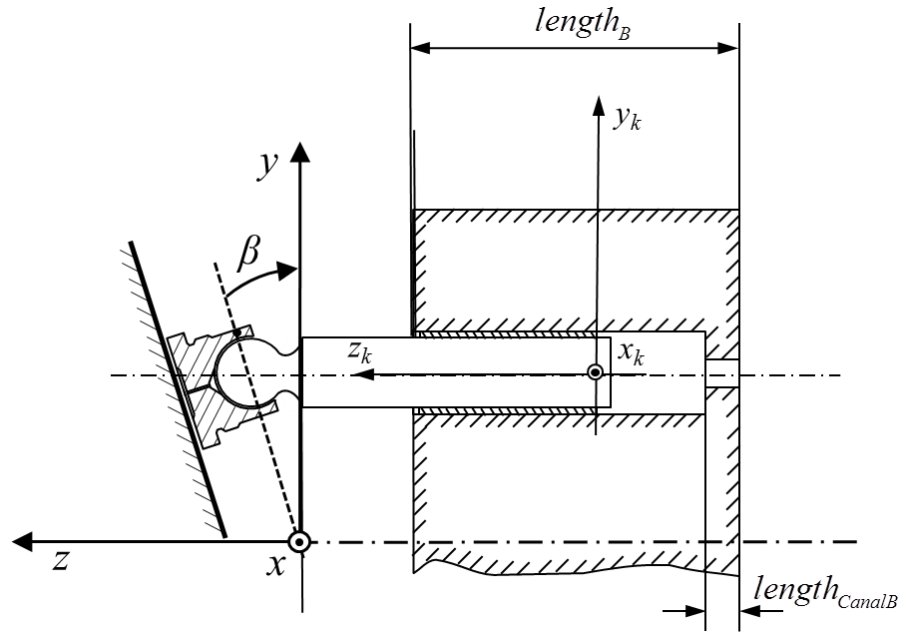


Figure 7.5. Cylinder block length and canal length representation.

The sealing land dimensions for the cylinder block/valve plate are the inner D1, inner port opening D2, outer port opening D4, and outer sealing D5 diameters as shown in Figure 7.6.

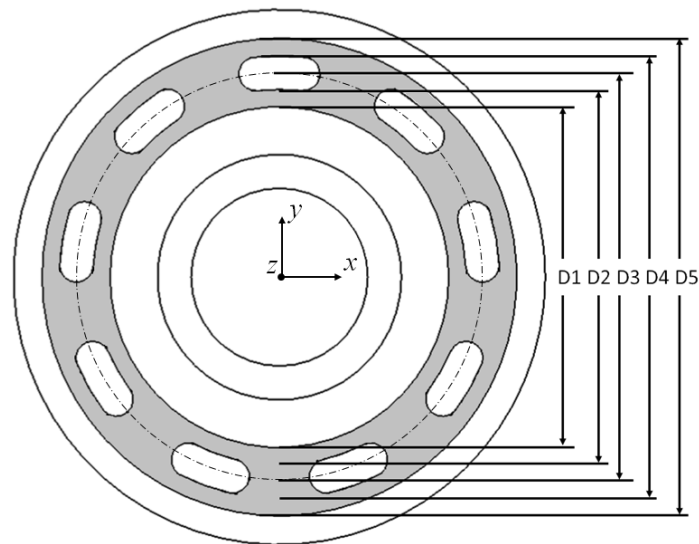


Figure 7.6: Cylinder block's bottom view and sealing land design parameters.

In previous section 6, it was shown that different geometrical designs of the end case can have a significant impact in the performance of the lubricating interface. The end case design can also be parametrized. An example of such a design example is shown in Figure 7.7. Figure 7.7 shows the two different end cases, the baseline is design A in the top has thickness $T1$ and the second it's rib

is thicker by a variable amount x (in this example ~ 6 mm) than the one originally assigned to the baseline design.

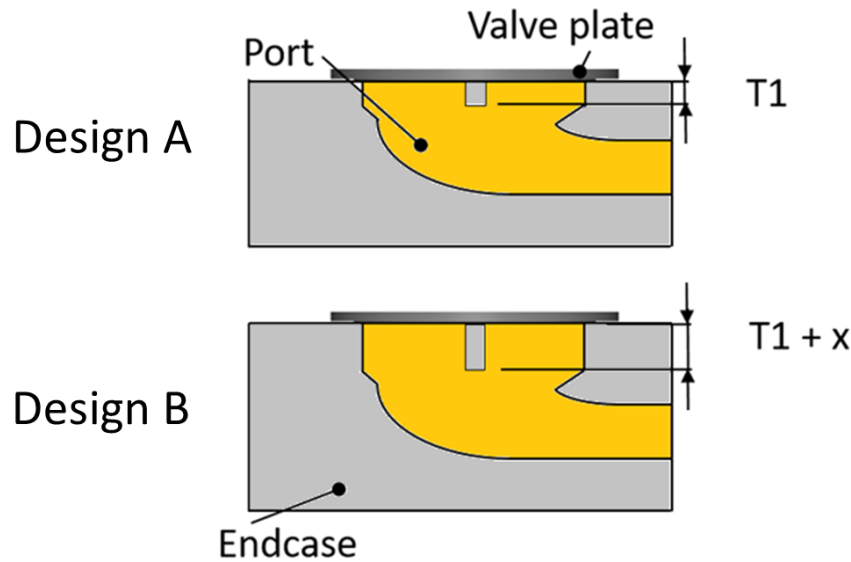


Figure 7.7. Endcase designs.

7.4 Cylinder Block/Valve Plate Interface Design Prototyping Example

In this section, the simulation results obtained for the case study 24 cc axial piston machine described previously on section 4.4 are shown and discussed. In this case study, a design of experiments (DOE) of 13 unique designs were created by varying the inner and outer diameter, simultaneously by 0.1 mm. The inner diameter is reduced (D1) and the outer diameter (D5) is increased. The end case design was also varied, utilizing the end case design examples shown in Figure 7.7. The material selection of the valve plate was varied as well. Two valve plate material compositions were utilized; one made entirely of steel and the second with a steel base and a thin layer of brass, shown in Figure 7.2.

Figure 7.8 through Figure 7.10 show the simulation results for the case study that was described in the previous sections. There are three main plots the total energy dissipation, power loss due to viscous friction and leakage flow from the cylinder block/valve plate interface. Each line represents a different end case and valve plate material composition. The bimetal design A corresponds to the green line which is the bimetal valve plate with end case design letter A. The

steel design A corresponds to the red line with a valve plate made of steel only and it has the end case design A. The steel design B is similar to the previous design with the only difference being the end case design. The x-axis corresponds to the design number where the inner diameter of the sealing land decrease and the outer diameter of the sealing land increase from left to right by 0.1 mm each.

The following figures show the energy dissipation, leakage flow and viscous friction for the maximum operating condition ($n=4000$ rpm, $\Delta p=450$ bar and full displacement). The figures demonstrate the impact of the different design modifications on the performance of the interface. The most significant effect can be observed as the lubricating interface area increases changing the hydrostatic balance factor and how the hydrodynamic effects interact in the interface. The expansion of lubricating area increases the load carrying ability of the interface resulting in a thicker fluid film thickness. The viscous friction diminishes due to the thicker fluid film but the leakage flow increases more significantly, since the leakage has a cubic relationship with film thickness. The dramatic increase in leakage flow increases the energy dissipation, especially after design 6 where the interface energy dissipation becomes dominated by the leakage flow. The endcase design doesn't show a significant effect on the energy dissipation. These simulation results indicate that design A is sufficiently stiff, and not more material is necessary to add more structural stiffness to the valve plate/end case assembly. The largest difference is of 5 percent and this is at a point where the sealing land geometrical parameters are certainly not optimal.

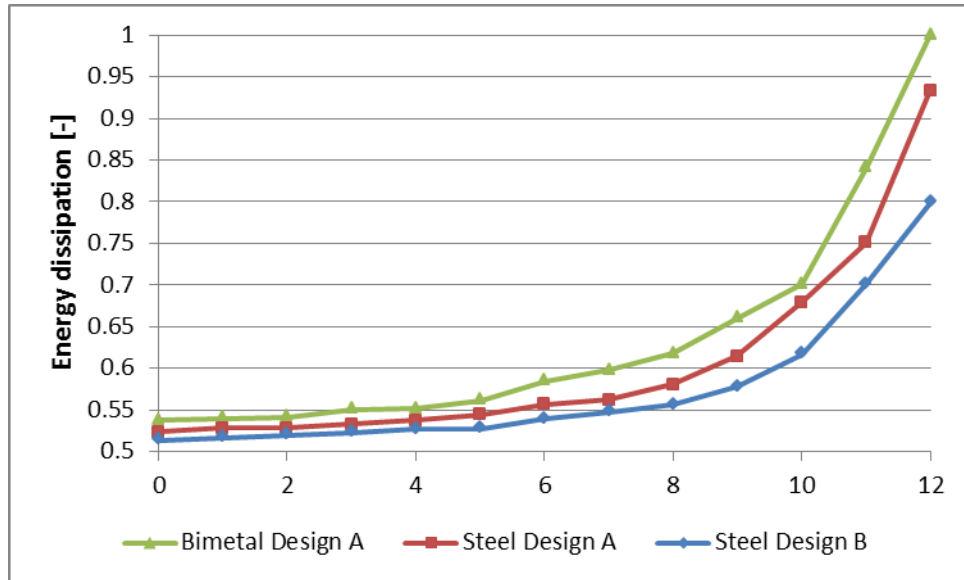


Figure 7.8. Energy dissipation in the cylinder block/valve plate interface ($n=4000$ rpm, $\Delta p=450$ bar and full displacement).

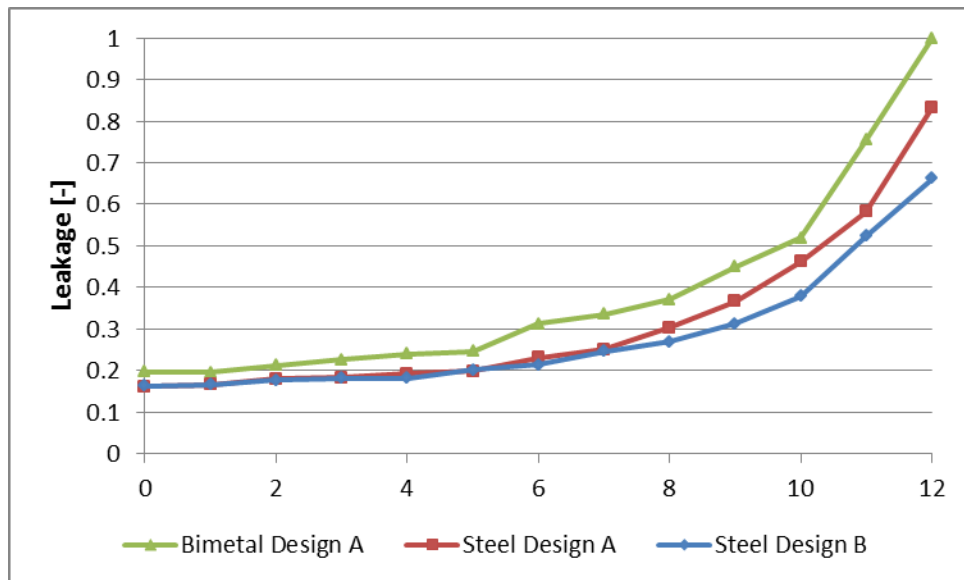


Figure 7.9. Leakage flow from the cylinder block/valve plate interface ($n=4000$ rpm, $\Delta p=450$ bar and full displacement).

The sealing land parameters design study show the lowest energy dissipation design is the first design, which corresponds to the largest inner diameter and smallest outer diameter of the sealing land for the cylinder block. Although, the energy dissipation is the lowest this design is certainly not the best design since its load carrying ability is not adequate. The load carrying ability of the lubricating interface must be such that it can balance the external loads exerted on the rotating

group, otherwise this could lead to mixed lubrication regime. Figure 7.10 shows the velocity correction for the cylinder block/valve plate interface which is necessary to keep the numerically calculated fluid film thickness above the surface roughness. This value is directly correlated to the load carrying ability of the lubricating gap. The velocity correction magnitude decreases as the lubricating area of the interface increases. From this figure, we could choose design number 8 as good compromise between energy dissipation and load carrying ability.

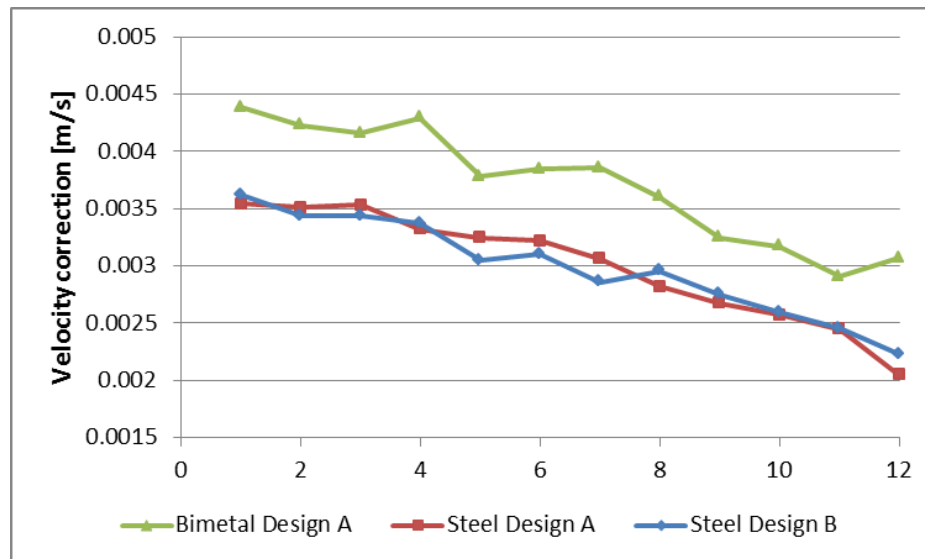


Figure 7.10. Velocity correction ($n=4000$ rpm, $\Delta p=450$ bar and full displacement).

From the previous three figures the design with the bimetal valve plate and end case design A was chosen. Figure 7.11 shows the total energy dissipation in Watts against and the number of possible contacts over one shaft revolution over the 13 designs of the sealing land. Design number 0 is the underbalanced, design number 4 is the recommended and design number 12 the overbalanced design shown in Figure 7.12. Design number 4 is the recommended design because it has a low energy dissipation while maintaining a reduced number of possible points of contact through an entire shaft revolution.

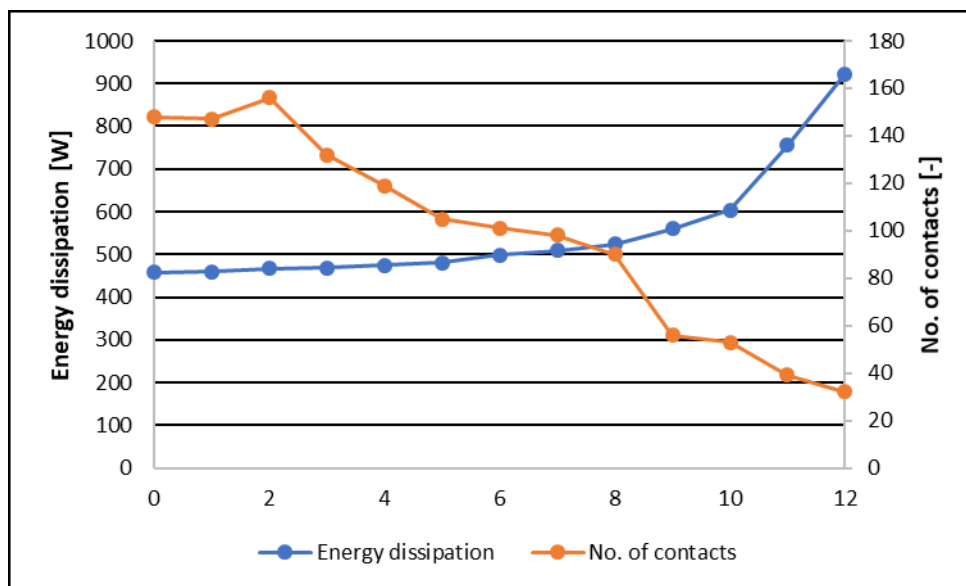


Figure 7.11. Energy dissipation and number of contacts predicted from the cylinder block/valve plate interface ($n=4000$ rpm, $\Delta p=450$ bar and full displacement).

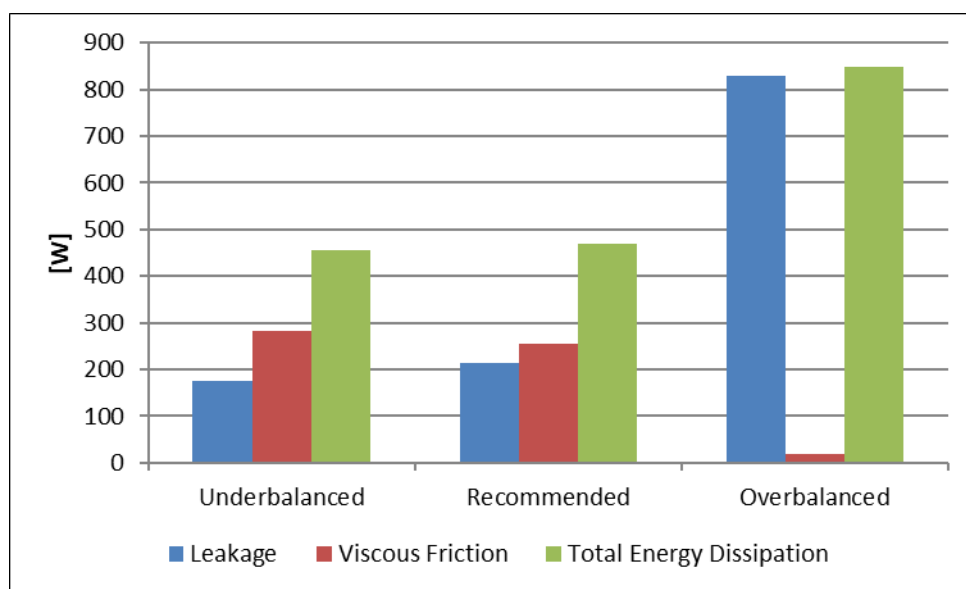


Figure 7.12. Underbalance, recommended, and overbalanced designs comparison breakdown by leakage, viscous friction, and total energy dissipation.

Figure 7.13 and Figure 7.14 are the three-dimensional representations of the fluid film in between the cylinder block and valve plate for the same three different designs selected from the thirteen designs with the Bimetal Design A configuration. These figures show an underbalanced design on the left, the recommended (optimal) design on the middle and a largely overbalanced design on the right. The corresponding energy dissipation is displayed in kilowatts as well. The operating

condition is the same as for Figure 7.8 through Figure 7.10 ($n=4000$ rpm, $\Delta p=450$ bar and full displacement). This representation is exemplary of having too low of a fluid film thickness and the energy dissipation being marginally better than the one of a thicker more stable fluid film (recommended design). It is also clear that overbalanced designs have grossly larger energy dissipation due to the thick film thickness observed on the design on the right which results in high leakage flow through the lubricating interface. The recommended design is analyzed over the entire range of specified operating conditions.

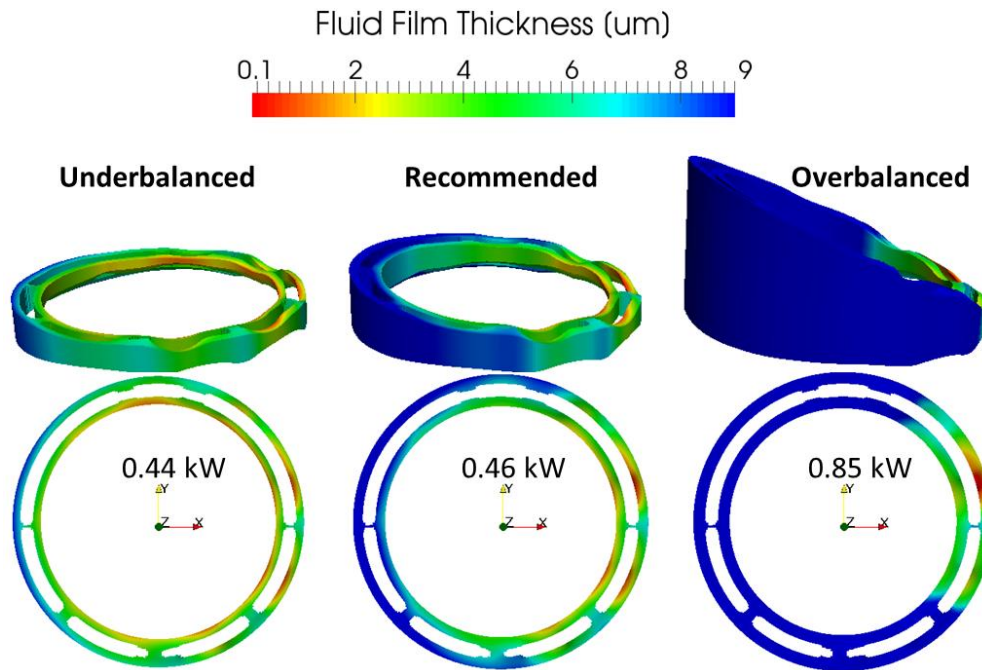


Figure 7.13. Three-dimensional representation of the fluid film, color scale fluid film thickness ($n=4000$ rpm, $\Delta p=450$ bar and full displacement).

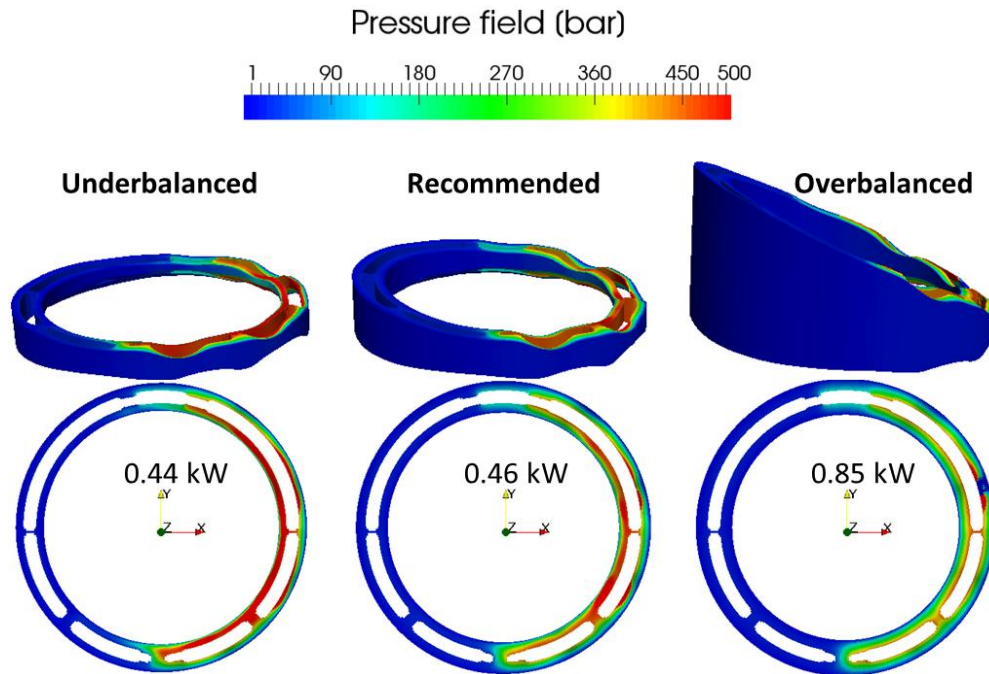


Figure 7.14. Three-dimensional representation of the fluid film, color scale pressure ($n=4000$ rpm, $\Delta p=450$ bar and full displacement).

7.5 Slipper/Swash Plate Interface Design within Virtual Prototyping

The slipper/swash plate interface design process follows the methodology described in Figure 7.1. The slipper swash plate interface is represented in Figure 7.15 which shows a finite amount of slipper sliding on the swash plate's running surface.

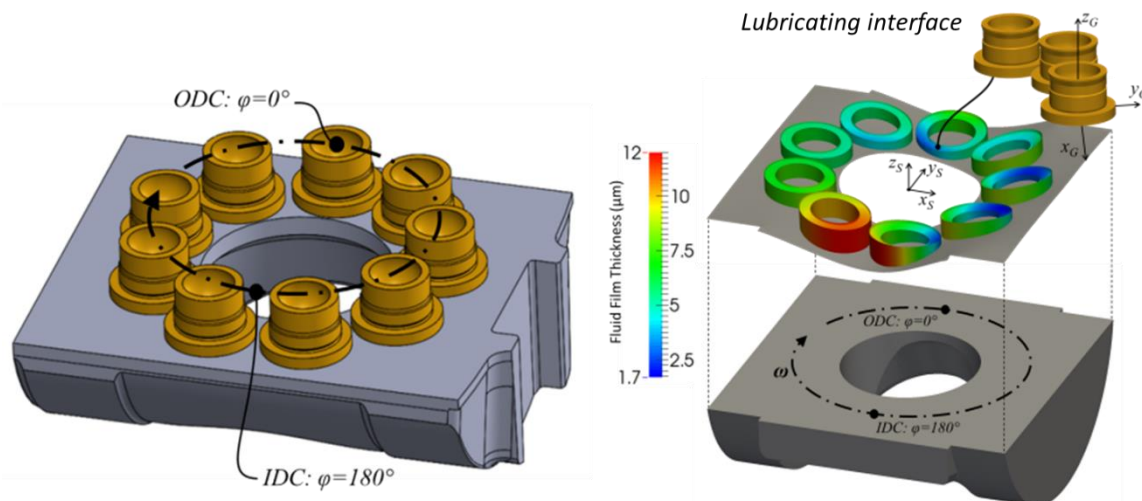


Figure 7.15. Slipper/swash plate interface schematic.

The design parameters for the slipper/swash plate interface are shown in Figure 7.16. The slipper sealing land dimension are the inner and outer sealing land diameters, d_{inG} and d_{outG} shown in as well. Similarly, as in the cylinder block/valve plate interface, the elastic deformation of the slipper and swash plate will have an impact on the lubricating interface. Therefore, the slipper and swash plate geometrical shape and material selection is also a part of the design parameters.

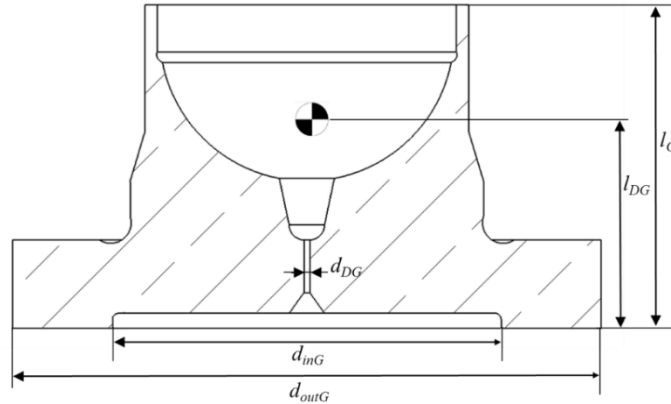


Figure 7.16. Slipper design dimensions.

7.6 Slipper/Swash Plate Interface Design Prototyping Example

The slipper/swash plate interface of the 24 cc axial piston machine case study described in section 4.4 is designed using the virtual prototyping methodology. The inner and outer sealing land diameters, d_{inG} and d_{outG} shown in Figure 7.16 define the slipper's sealing land. The case study used design of experiments (DOE) of 40 different designs which were generated by varying the inner diameter d_{inG} only based on a full factorial approach. The inner diameter parameter modifies the effective lubricating area of the interface which has an important effect on the load carrying ability of the lubricating interface.

Figure 7.17 show the energy dissipation and leakage flow over one shaft revolution for the five operating conditions. The figures demonstrate the impact of the sealing land design modifications on the performance of the interface. The increase of lubricating area increases the load carrying ability of the interface resulting in a thicker fluid film thickness therefore increasing the leakage flow as shown in Figure 7.17. The viscous friction diminishes due to the thicker fluid film but the leakage flow increases more significantly, since the leakage has a cubic relationship with film thickness. The dramatic increase in leakage flow increases the energy dissipation, especially after

design 25 where the interface energy dissipation becomes dominated by the leakage flow. The optimal design region between the leakage flow and energy dissipation is found in the design region 20-25. This area has been shaded in Figure 7.17.

It's important to note that the simulation results before design 20 don't show a clear trend. The reason for this is the slipper hydrostatic area being too small and the slipper/swash plate interface being underbalanced, results in a collapsed fluid film areas between the slipper and the swash plate. All the simulations before design 20 break the design constraint of maintaining a full fluid film lubrication therefore are disregarded from the design process. The design algorithm would then update the design bounds based on this function evaluations, setting as a lower bound. For this case study, a single iteration of the design process to demonstrate the feasibility of the virtual prototyping methodology is shown.

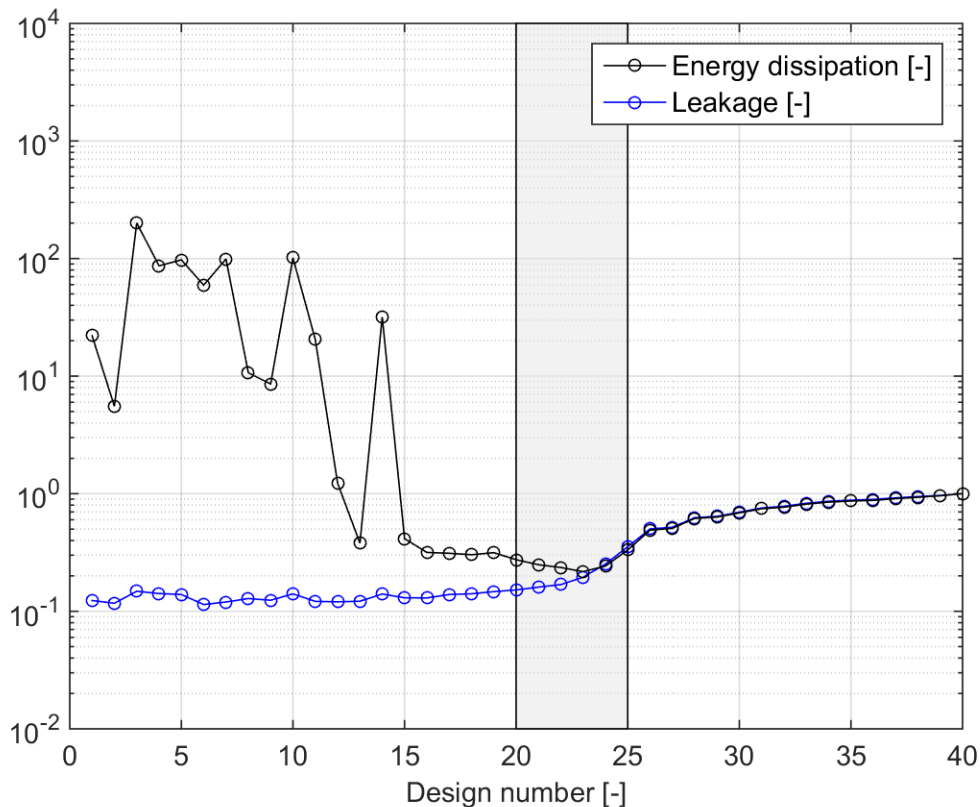


Figure 7.17. Energy dissipation in the slipper/swash plate interface ($n=4000$ rpm, $\Delta p=450$ bar and full displacement).

The three-dimensional representation of the fluid film thickness between the slipper and the swash plate is shown in Figure 7.15. Similarly, Figure 7.19 shows a three-dimensional representation of the fluid film thickness where the color scale represents the pressure field distribution in the fluid film (at shaft angle 50°). The design on the left corresponds to design number twenty the one with the lowest hydrostatic balance factor without resulting in a collapsed fluid film, the one in the middle is the recommended design and the one on the right is the grossly overbalanced design. Both figures show simulation results for the same operating condition than the one shown in Figure 7.17. Figure 7.18 shows a completely collapsed fluid film on the left most slipper fluid film representation on the negative direction on the x-axis. The negative direction in the slipper/swash plate interface represent the trailing edge of the slipper. The fluid film collapse is due to the insufficient pressure generation in the gap to balance the external loads and achieve full fluid film lubrication. The recommended design, in this case design number twenty-five, has a good compromise between low energy dissipation and low amount of possible contacts.

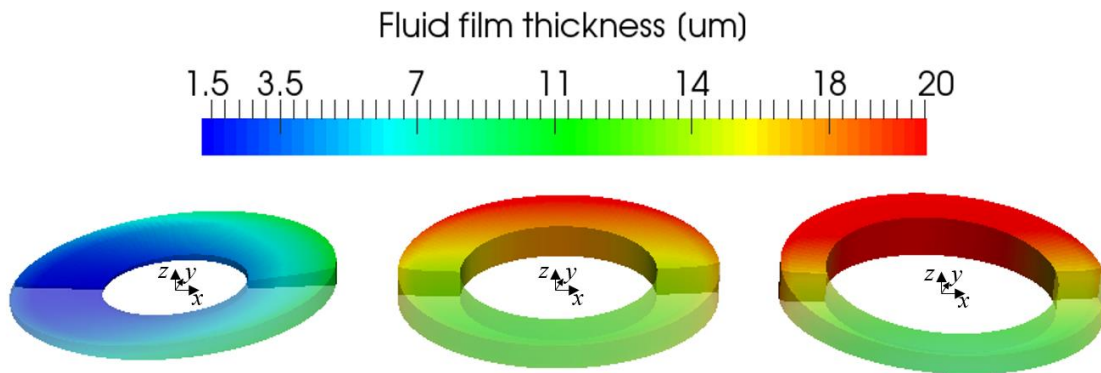


Figure 7.18. Fluid film thickness ($n=4000$ rpm, $\Delta p=450$ bar and full displacement).

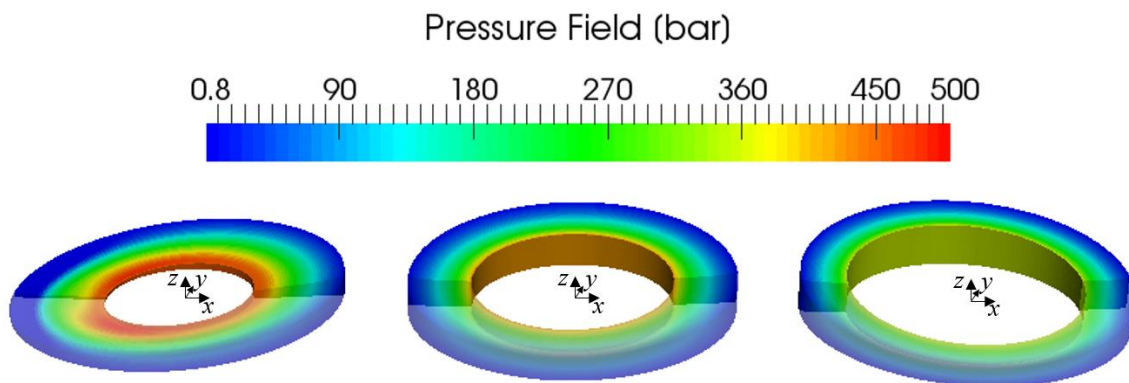


Figure 7.19. Fluid film thickness and pressure field in color ($n=4000$ rpm, $\Delta p=450$ bar and full displacement).

7.7 Piston/Cylinder Interface Design within Virtual Prototyping

A representation of the piston/cylinder interface is depicted in Figure 7.20; the color scale is representing the pressure field. The main design parameters for the piston/cylinder interface are shown in Figure 7.21. The diameter of the piston d_K and the diameter of the bore d_z are the most critical dimensions since these together define the clearance which impacts the fluid flow through the gap and viscous friction. The length of the piston l_K and the length of the bore l_f are important as well as they define the rest of the lubricating interface geometry. The piston/cylinder interfaces performance is influenced by elastic deformations of the solid bodies. Therefore, the solid bodies may need to be redesigned as shown in section 6.2. For the 24cc design example refer to Busquets (2018).

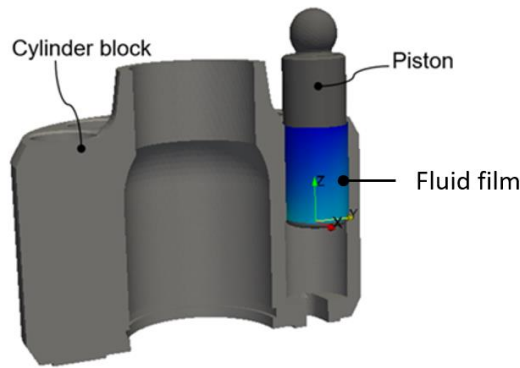


Figure 7.20. Piston/cylinder interface schematic.

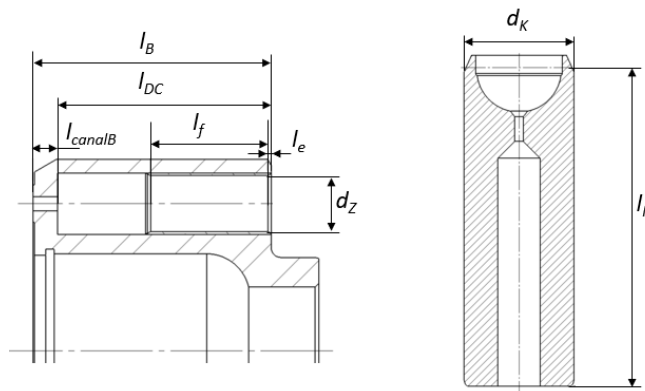


Figure 7.21. Piston/cylinder interface main dimensions.

8. PHYSICAL PROTOTYPE AND EXPERIMENTAL SETUP

In order to validate the proposed virtual prototyping methodology on this dissertation, the first ever axial piston machine of swash plate type designed utilizing the methodology with no baseline working design case study described on section 4.4 was built and tested. The physical prototype pictures are shown in Figure 8.1. The axial piston machine's displacement is 24 cc per revolution. The machine has a fixed swash plate angle of 21° . It has nine pistons. For the physical prototype, the housing and end case were machined from solid parts of steel not casted due to monetary and time cost limitations. Figure 4.6 shows the cross-sectional views of the computational model of the axial piston machine. Figure 8.1 shows the physical prototype pictures of the disassembled components and the partially assembled machine. The experimental tests covered the main performance parameters of the pump such as volumetric and mechanical efficiencies. Other performance parameters such as noise emission and flow and pressure ripple were not part of this paper in the interest of maintaining a reasonable length.

The swash plate type axial piston machine prototype was specified to be able in a wide range of operating conditions. The pressure differential ranged from 0–400 bar, with max operating pressure of 450 bar. The rotating shaft speed between 500–4000 rpm. The prototype's rotating group components were designed to range from 0– 21° . The temperature could vary from 0 °C to 80 °C. The physical prototype was tested on a wide range of operating conditions to prove that this pump could operate in the complete range that it was intended to. The operating conditions are described in Table 8.1.

Table 8.1. Operating conditions range.

Description	Specification
Pressure differential	50, 100, 200, 300, 400 [bar]
Speed	1000, 2000, 3000 [rpm]
Displacement	100 [%]
Temperature	42, 52, 72 [°C]

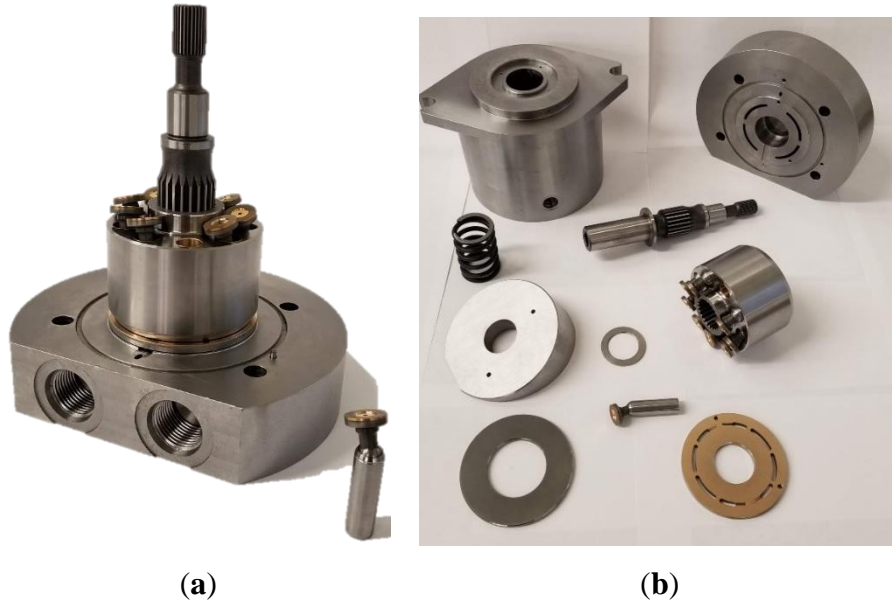


Figure 8.1. Axial piston machine of swash plate type physical prototype.

8.1 Component Inspection

The components were received and inspected utilizing CMM and depth micrometers from Purdue's Mechanical Engineering metrology department as shown in Figure 8.2.



Figure 8.2. CMM inspection of components.

The components were also measured using a surface profilometer to collaborate if the specified surface finish and the micro-surfacing shape was correct. The piston was given a barrel shape in order to be able to minimize the clearance and minimize the total energy dissipation of the

lubricating interface. The piston surface shape was optimized by Busquets (2018) due to tolerances the optimal was not used. A similar profile to the one exemplified in Ivantysyn and Ivantysynova (2001) was utilized. The piston/slipper assembly was sourced from Takako.

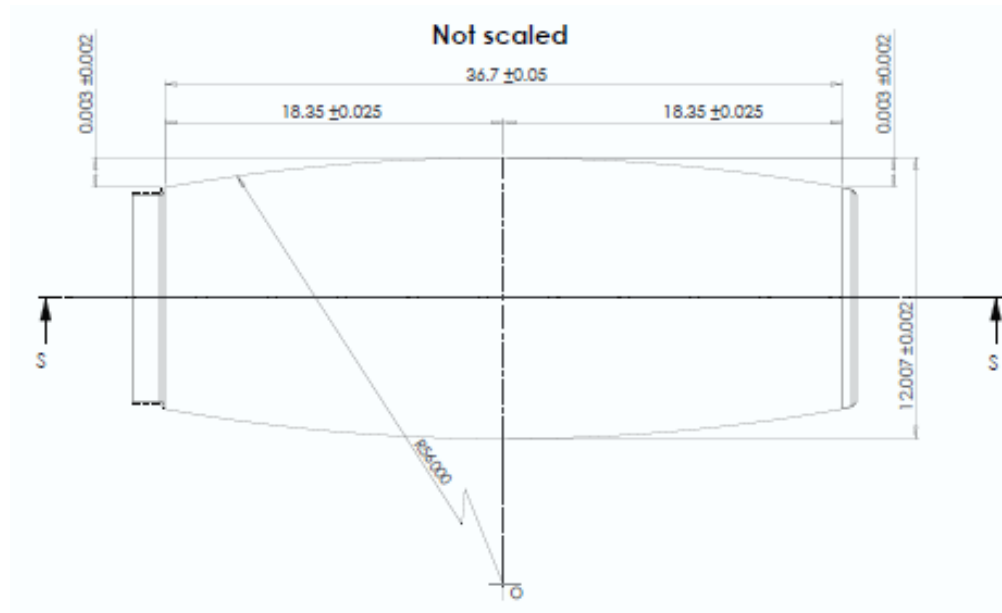


Figure 8.3. Piston dimensions and tolerances.



Figure 8.4. Piston/slipper assembly prototype.

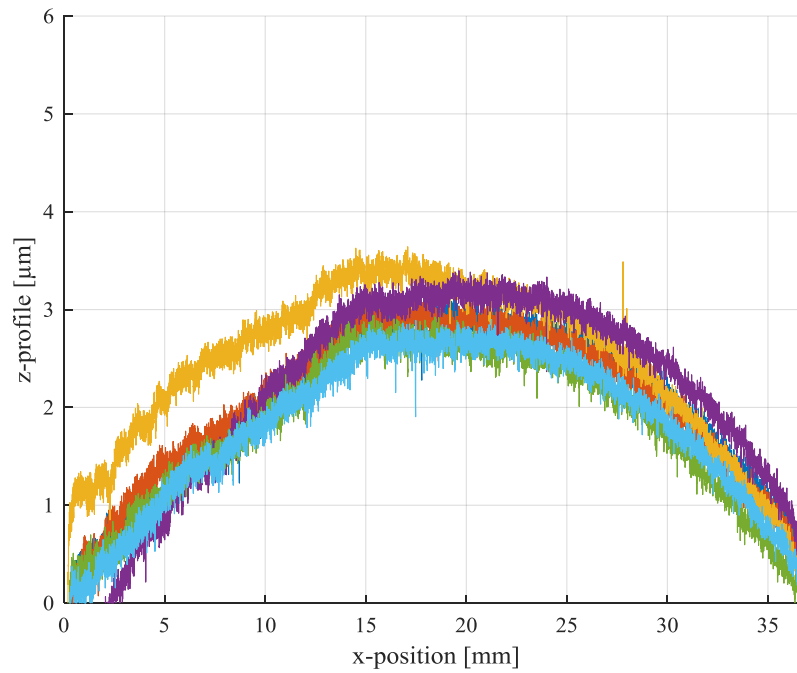


Figure 8.5. Three profilometer traces across the barrel piston surface.

Similarly, the slipper was optimized to have an optimal surface shape. The slipper had a wedge added on the inner and outer edges. These wedges contribute to additional hydrodynamic pressure generation which increases the load carrying ability of the interface while reducing energy dissipation.

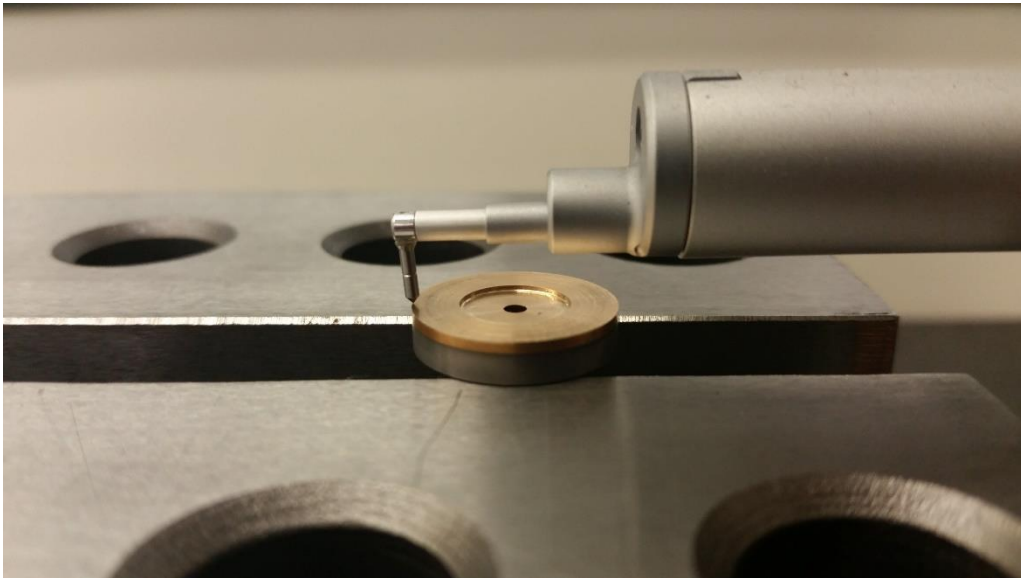


Figure 8.6. Slipper profilometer trace.

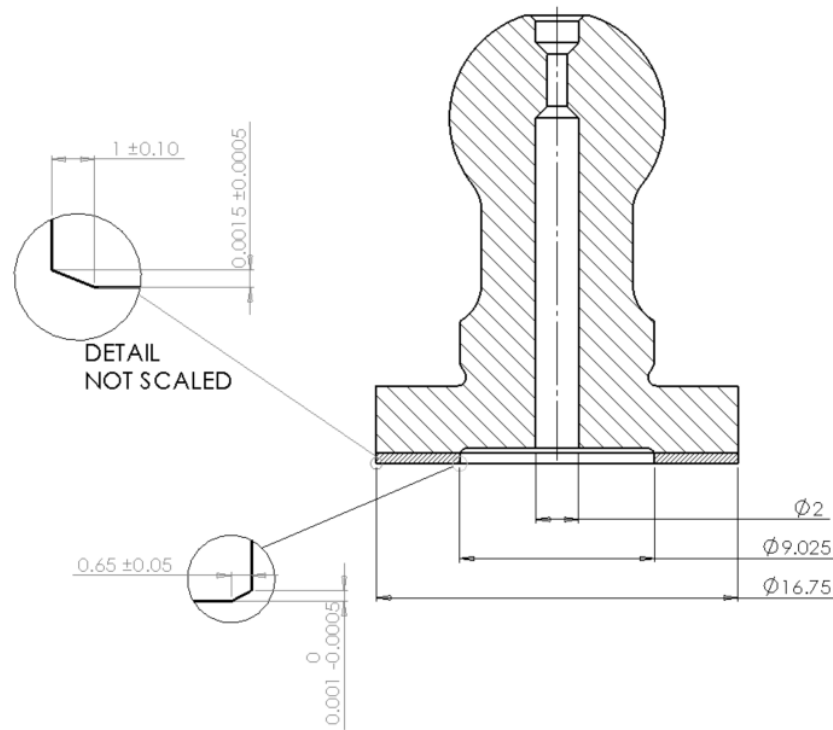


Figure 8.7. Slipper leading edge dimensions.

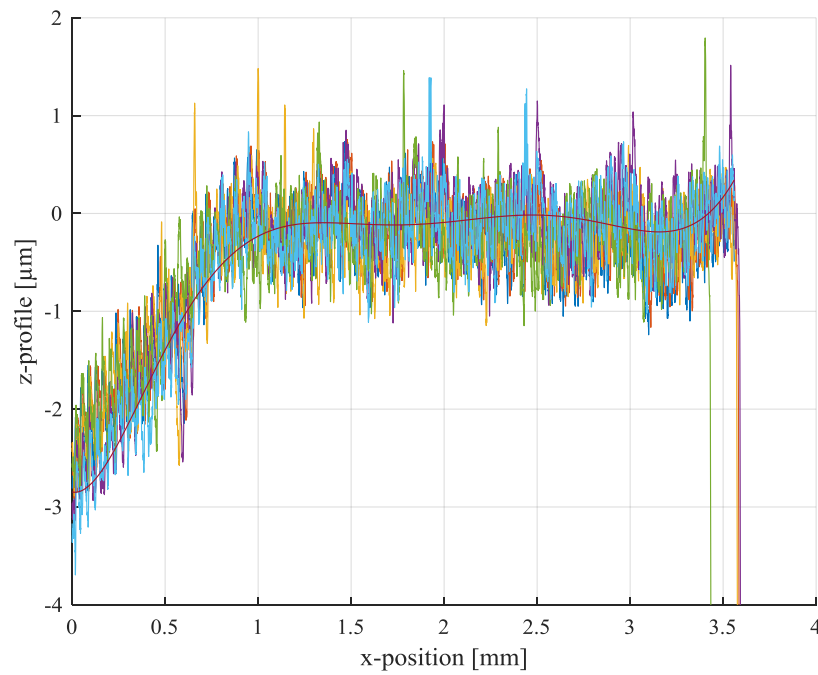


Figure 8.8. Slipper leading edge profilometer traces.

8.2 Axial Piston Machine Assembly

The components were assembled at the Maha Fluid Power Research Center. An exploded view of the assembly is shown in Figure 8.9. A total of 28 different parts were utilized in the physical prototype. The bill of materials (BOM) with assigned part number, description, quantity and supplier is shown in Appendix A. Figure 8.10 shows a cross-section of a part of the assembly here is clearly represented how the cylinder block barrel is compressed in between the shaft and a retainer ring on the cylinder block. The design and build of special fixtures for the successful assembly were done in the research center as well. Figure 8.11 shows an image of the special fixture that was built to compress the spring while holding the snap ring compressed.

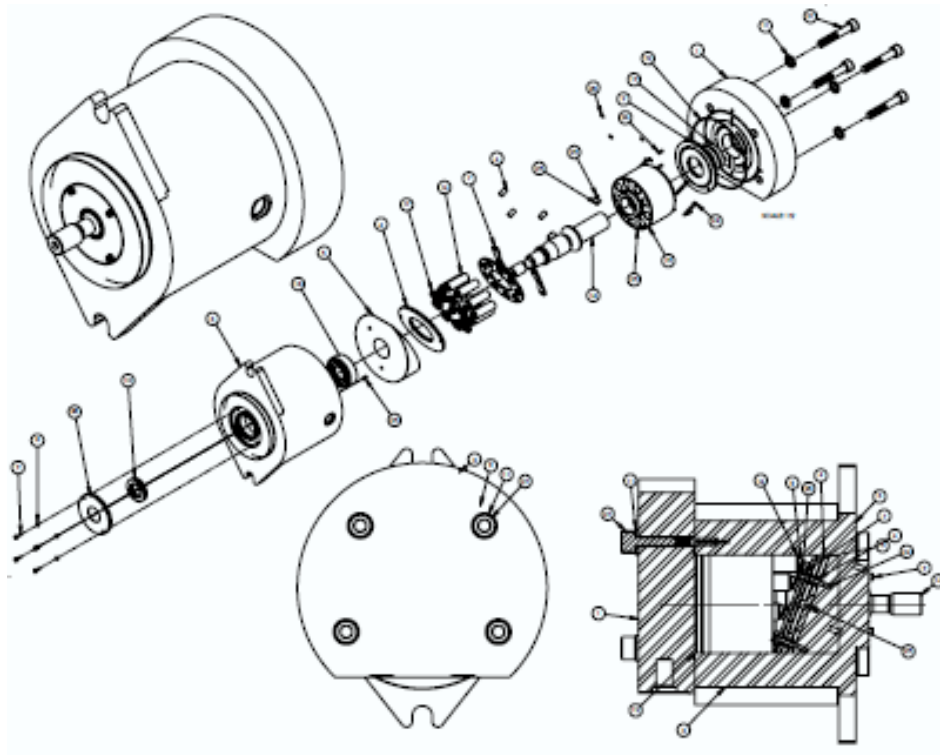


Figure 8.9. Axial piston machine of swash plate exploded view.

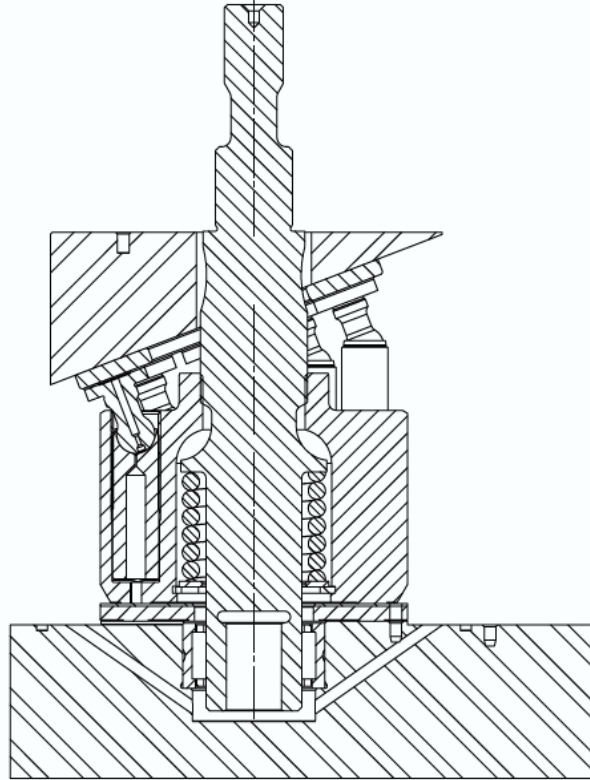


Figure 8.10. Assembly cross-section.



Figure 8.11. Fixture to install cylinder block spring and snap ring.

8.3 Test Stand

A 225-kW test stand at the Maha Fluid Power Research Center was utilized to drive the axial piston machine, shown in Figure 8.12. The ISO hydraulic circuit of the test stand is detailed in Figure 8.13. The drive is an electric motor (1) connected to the pump via couplings and a torque cell (2,3). The inlet of the pump (4) is supplied by a power supply at a constant pressure of 20 bar. The outlet of the pump goes to a flowmeter (9) and then the pressure relief valve (13) which is

acting as the load in this test rig setup. The test rig was instrumented with some transducers to record critical performance data from the positive displacement machine such as thermocouples on the inlet, outlet, and drain lines. Pressure transducers were also present in the inlet, outlet, and drain lines. Table 8.2 describes all the components utilized in this experimental setup. It includes the data acquisition (DAQ) cards from National Instruments (Austin, TX) that were utilized to record the signals coming from all the transducers. An ISO 32 fluid was utilized for these experiments. Figure 8.12 shows a picture of the test rig set up.



Figure 8.12. Steady state test rig with 24 cc prototype mounted.

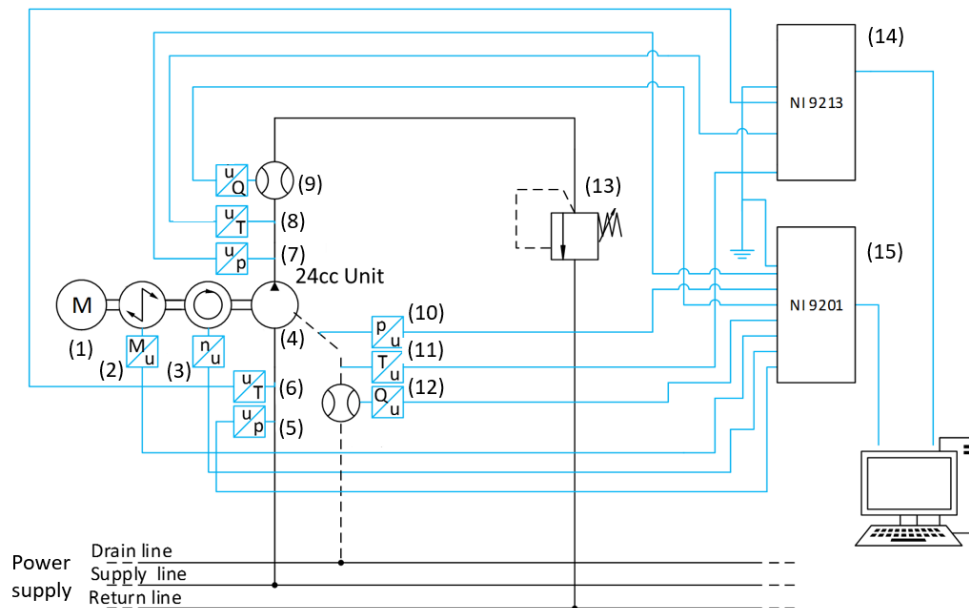


Figure 8.13. ISO schematic of the steady-state test rig.

Table 8.2. Test rig set up components.

ID	Description	Specification
1	Electric drive	Max power: 225 Kw, Max torque 615 Nm @3500 rpm
2, 3	Staiger Mohilo torque cell	0–500 Nm range, error $\pm 0.2\%$ of full scale
4	Closed circuit pump	24cc, fixed displacement, max torque 160 Nm @ $\Delta p = 400$ bar
5	Pressure transducer	WIKA S-10, 0–100 bar, 0.125% BFSL
6, 8, 11	Thermocouple	Omega K-type Thermocouple, 2.2 °C error limit
7	Pressure transducer	HYDAC HAD 4445, 0.5% BFSL
9	Flowmeter	VSE VS 10 Gear type, 1.2–250 L/min, 0.3% accuracy
10	Pressure transducer	WIKA S-10, 0–25 bar, 0.125% BFSL
12	Flowmeter	VSE VS 0.2 Gear type, 0.02–18 L/min, 0.3% accuracy
13	Pressure relief	Max flow 350 L/min
14	DAQ	NI cDAQ , NI 9213
15	DAQ	NI cDAQ , NI 9201

9. EXPERIMENTAL RESULTS

The experimental results of the 24cc axial piston machine are shown in this section. A total of forty-five operating conditions at steady state conditions were performed. The total amount of hours the axial piston machine was ran on the test stand was ~30 hours. The figures shown in this section are for fifteen out of the forty-five because the results were very similar in its trends. The recorded data shown was after an initial break in of 2 hours. The pump was cycled over a large variety of operating conditions until the drain flow and the drain temperature stabilized. Figures 8.1 – 8.3 shows the performance data of the steady state measurements taken of the 24 cc axial piston machine prototype. The measurements are shown for 15 operating conditions only since the measurements follow very similar across the two additional temperature of 42 °C and 72 °C. The total efficiency of the machine fluctuates from 60 to 82 %. The results vary with speed and pressure. It is clear from these measurement results that the axial piston machine has lower efficiencies at the 1000 rpm condition. The low efficiency can be explained due to high internal leakage due to the valve plate design. Previous research by Kim et al. (2014) shows similar results in simulation.

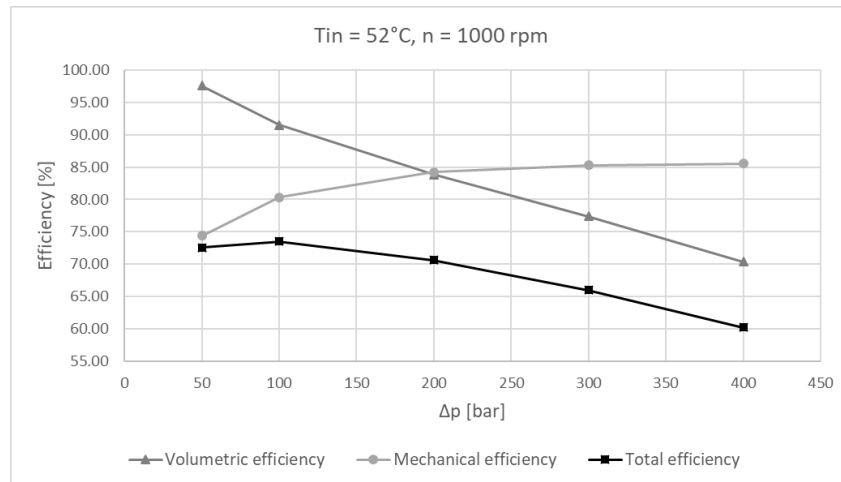


Figure 9.1. Prototype efficiencies at $n = 1000$ rpm, $T = 52$ °C, and $\Delta p = 50$ –400 bar.

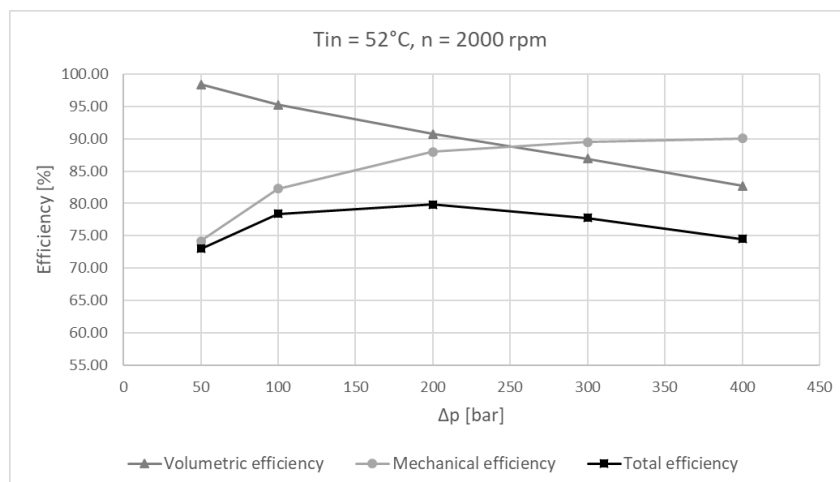


Figure 9.2. Prototype efficiencies at $n = 2000 \text{ rpm}$, $T = 52^{\circ}\text{C}$, and $\Delta p = 50\text{--}400 \text{ bar}$.

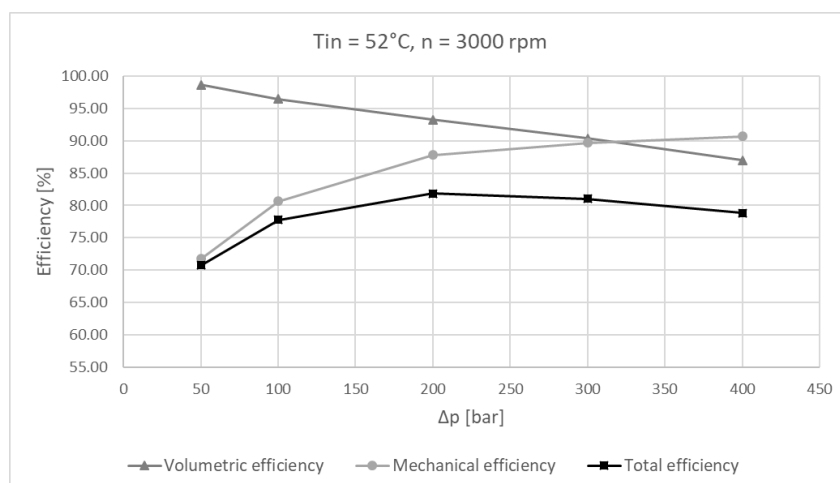


Figure 9.3. Prototype efficiencies at $n = 3000 \text{ rpm}$, $T = 52^{\circ}\text{C}$, and $\Delta p = 50\text{--}400 \text{ bar}$.

9.1 Experimental Results and Simulation Comparison

This section shows a comparison of the measurements against the simulation results. The measured operating conditions (speed, temperatures, and pressures) were utilized as inputs for the numerical models to simulate as close as possible the measurements realized on the test stand. Figures 9.4 – 9.6 show the volumetric efficiency of the machine. The volumetric efficiency was modelled in the pressure module described in section 3.1. The pressure module uses the shaft speed, port temperatures, port pressures, the drain flow, geometry, fluid properties, etc. as inputs to calculate the effective outlet flow and the pressure in the displacement chambers. Another important parameter is given to the orifice equation inside the pressure module. This parameter is the discharge coefficient α shown in Equation (2). The simulations shown in this work utilized a discharge coefficient of 0.8. The simulation results match closely the measured volumetric efficiency.

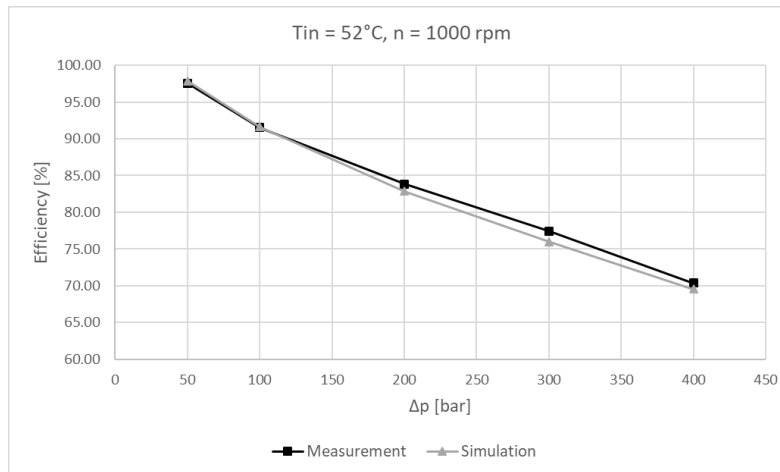


Figure 9.4. Volumetric efficiency measured compared against simulated at $n = 1000 \text{ rpm}$, $T = 52^{\circ}\text{C}$, and $\Delta p = 50\text{--}400 \text{ bar}$.

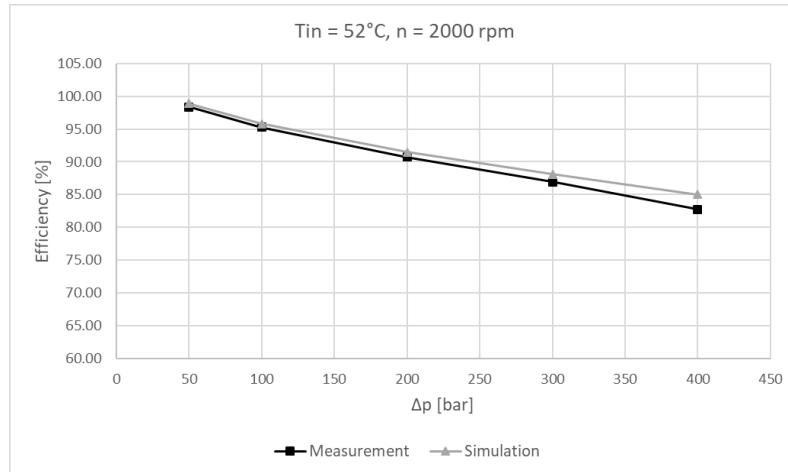


Figure 9.5. Volumetric efficiency measured compared against simulated at $n = 2000$ rpm, $T = 52$ °C, and $\Delta p = 50$ – 400 bar.

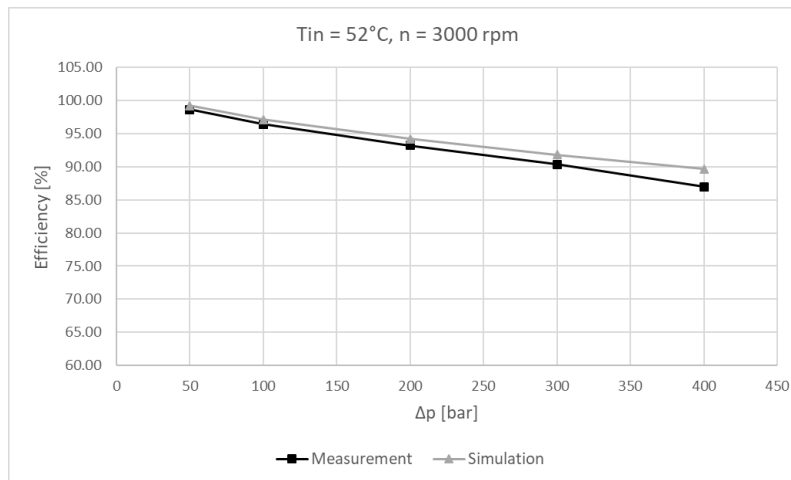


Figure 9.6. Volumetric efficiency measured compared against simulated at $n = 3000$ rpm, $T = 52$ °C, and $\Delta p = 50$ – 400 bar.

The measured and simulated mechanical efficiency comparison for three operating conditions is shown in Figures 9.7 – 9.9. The function evaluations from TEHD model followed the trends but not the values. The mechanical efficiency differences are discussed in section 9.2.

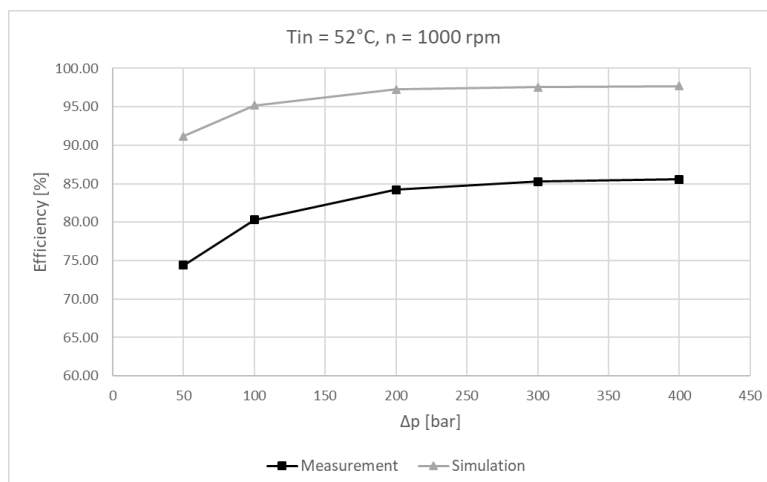


Figure 9.7. Mechanical efficiency measured compared against simulated at $n = 1000$ rpm, $T = 52^\circ\text{C}$, and $\Delta p = 50\text{--}400$ bar.

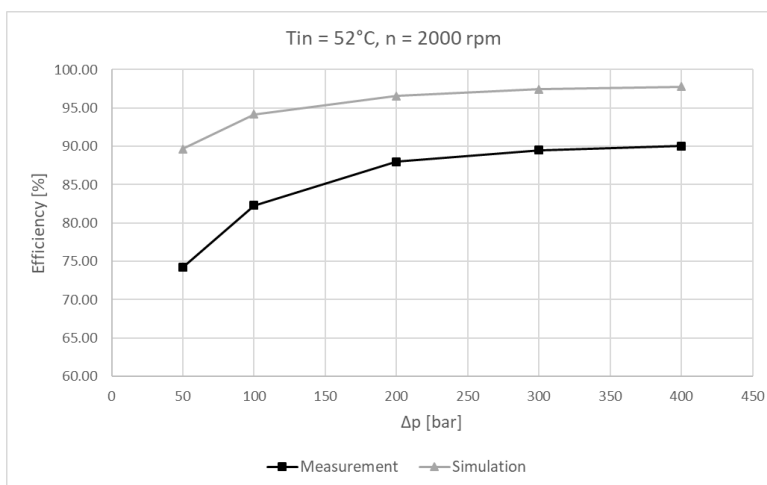


Figure 9.8. Mechanical efficiency measured compared against simulated at $n = 2000$ rpm, $T = 52^\circ\text{C}$, and $\Delta p = 50\text{--}400$ bar.

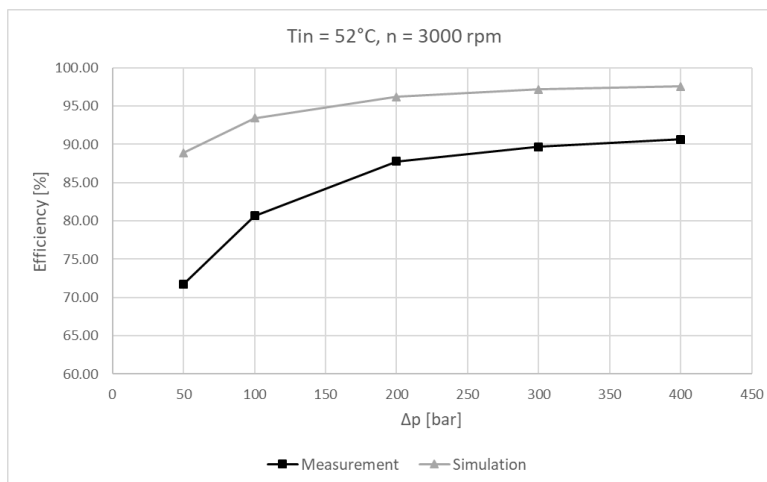


Figure 9.9. Mechanical efficiency measured compared against simulated at $n = 3000$ rpm, $T = 52^\circ\text{C}$, and $\Delta p = 50\text{--}400$ bar.

Also, a comparison of the drain flow measured against the simulated external leakage through the lubricating interfaces is shown in Figures 9.10 – 9.12. In the case of fixed displacement axial piston machines, the drain flow only comes from the external leakage through the lubricating interfaces from the pressurized fluid volumes in the ports and displacement chambers to the case volume. The drain flow contributes to the energy dissipation but it also has an important function of rejecting the heat of machine. The simulation results extracted from the TEHD models match closely with the measured drain flows.

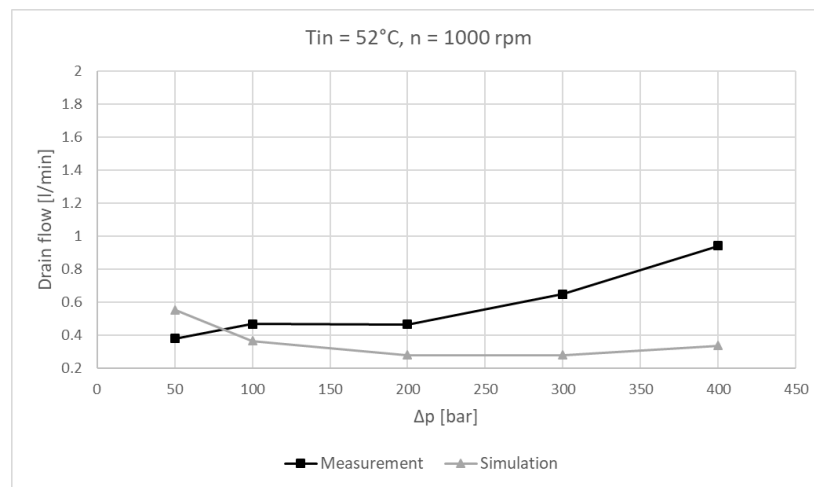


Figure 9.10. Drain flow comparison at $n = 1000$ rpm, $T = 52$ °C, and $\Delta p = 50$ –400 bar.

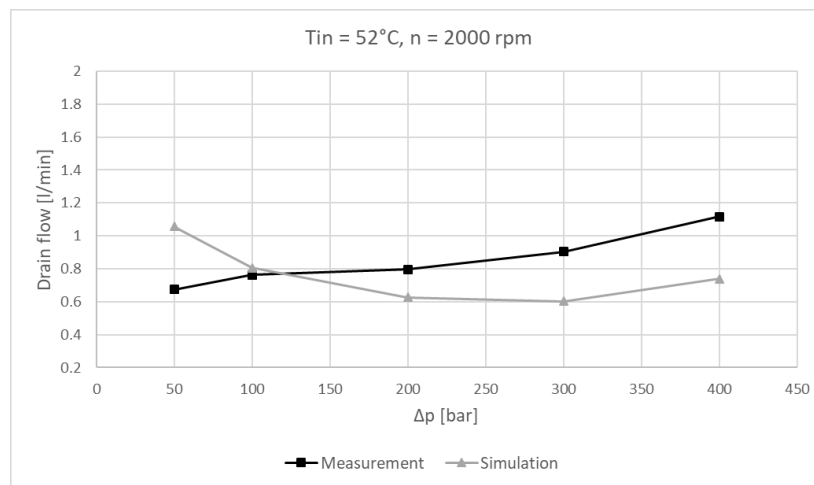


Figure 9.11. Drain flow comparison at $n = 2000$ rpm, $T = 52$ °C, and $\Delta p = 50$ –400 bar.

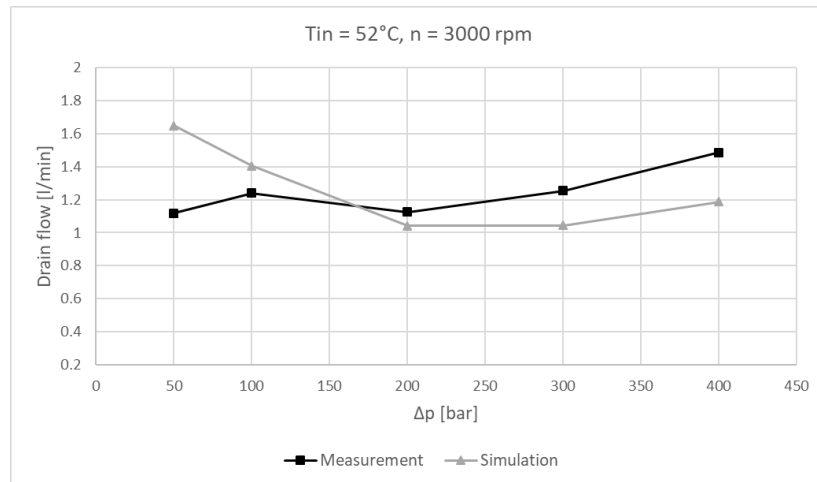


Figure 9.12. Drain flow comparison at $n = 3000 \text{ rpm}$, $T = 52^{\circ}\text{C}$, and $\Delta p = 50\text{--}400 \text{ bar}$.

9.2 Discussion

The mechanical efficiency measurement results comparison against simulation results are significantly different. The measured mechanical efficiency was not as high as those predicted from the simulation tool. The root cause of this discrepancy is the slipper retainer system which did not form part of the three main lubricating interfaces on which this work focused on. The slipper retainer system produced unanticipated torque loss is the friction between the slipper retainer plate sliding and the fixed hold-down mechanism. After testing the prototype was disassembled and wear was discovered as shown in Figure 9.13. Other factors may have contributed to the torque loss such as shaft bearings and churning losses. This dissertation focused on the design of the components influencing the performance of the three lubricating interfaces only. The slipper retainer mechanism is necessary for the correct functioning of an axial piston machine but out of the scope of this work. Future research on these machines should take into consideration this interface between slipper retainer plate and the bracket. The author believes the measurement against simulation comparison in section 9.1 is valid despite the discrepancy in magnitudes because the TEHD models closely matches the drain flow. The drain flow can only be calculated if the fluid film thickness is accurately predicted in the models and the drain flow is derived from the fluid film's fluid velocity field and fluid film's gap thickness.



Figure 9.13. Worn slipper retainer plate after measurements.

10. CONCLUSIONS

A novel methodology to design swash plate type axial piston machines based on a computationally based approach was presented. The methodology enables virtual prototyping of axial piston machines of swash plate type. The virtual prototyping methodology reduces significantly the time and cost of the design process while producing an efficient and robust design. The use of advanced numerical models and optimization schemes enables the exploration of new geometrical features and materials. The virtual prototyping methodology focuses on the design of the valve plate, cylinder block, piston/slipper assembly, swash plate and end case. The first step is the valve plate optimization, second is the FEM analysis and solid bodies design, and finally the lubricating interfaces design.

The valve plate optimization refers to the optimization of the port timing. The valve plate controls the connection of the displacement chamber to the ports. The objective functions are to maximize the volumetric efficiency, minimize structure-borne noise sources, swash plate moment amplitudes ΔM_x and ΔM_y , fluid-borne noise source flow ripple ΔQ_{HP} , and control effort of the axial piston machine's swash plate (mean M_x).

The lubricating interfaces are optimized for maximum efficiency while minimizing the operating of the machine in the mixed lubrication regime. A multi-domain numerical model is utilized in the which includes the calculation of the instantaneous pressure in the displacement chamber, the temperature prediction of the delivery port and case volume and a novel thermo-elastohydrodynamic model (TEHD). The main design parameters modifying the sealing land dimensions and clearance ratios are varied to minimize the energy dissipation to achieve the highest efficiency design. The design simultaneously needs to maintain a full fluid film between the cylinder block and valve plate, piston and cylinder bore, and the slipper and swash plate by balancing the external loads imposed on the rotating parts due to the kinematics of the machine.

The methodology proposed in this work was validated via the design and build of the first ever axial piston machine within a virtual prototyping framework. The prototype is a 24 cc axial piston machines of swash plate type prototype. The experimental measurement results showed a total

efficiency ranging from 60 to 82 % which is lower than expected from what the simulations showed. The prototype can be in the market with some minor changes around the slipper retaining mechanism, which was out of the scope of this dissertation this would improve the mechanical efficiency. The volumetric efficiency can be improved lower operating speeds by modifying the cost functions that were formulated in the valve plate optimization phase. The tested prototype was the product of a single iteration of the virtual prototyping methodology.

APPENDIX

ITEM NO.	PART NUMBER	DESCRIPTION	QTY.	Supplier
1	24-008-AHO-0004,000	End case	1	ISSI
2	24-001-AVP-0001,000	Valve plate	1	CAMCRAFT
3	24-008-AHO-0003,000	Housing	1	ISSI
4	24-011-ASW-0001,000	Trust plate	1	CAMCRAFT
5	24-003-ASW-0003,000	Fixed swash plate (full displacement)	1	ISSI
6	24-SFA-ASW-0001,000	Slipper hold-down spacer	4	ISSI
7	24-009-AHD-0002,000	Slipper hold-down bracket	2	ISSI
8	24-WAS-AHO-0001,000	M2.5 Washer	4	McMaster
9	24-SFA-AHO-0001,000	M2.5 Screw, 8mm L	4	McMaster
10	24-SFA-ASH-0001,000	Shaft Lip seal	1	TREUBLEBORG
11	24-WAS-AHO-0003,000	M10 Washer	4	McMaster
12	24-ORC-AHO-0003,000	O-Ring Bung-N 107mm ID, 2mm Wide	1	McMaster
13	24-009-AHD-0001,000	Slipper hold-down plate	1	ISSI
14	24-002-ASH-0001,000	Rotating shaft	1	ISSI
15	24-AB8-001-0000,000	Cylinder block	1	CAMCRAFT
16	24-006-API-0001,000	Female piston	9	Takiko
17	24-007-API-0001,000	Male slipper	9	Takiko
18	24-BEF-ASH-0001,000	Shaft bearing (front)	1	SKF
19	24-BER-ASH-0001,000	Shaft bearing (rear)	1	SKF
20	24-SRG-AB8-0001,000	Snop ring cylinder block spring	1	McMaster
21	24-WAS-AB8-0001,000	Cylinder block spring washer	1	ISSI
22	24-SPE-AB8-0001,000	Cylinder block spring	1	Myers Spring
23	24-WAS-AHO-0004,000	M3 Washer	4	McMaster
24	24-SCR-AHO-0005,000	M8 Screw Fully threaded, 22mm L	4	McMaster
25	24-PIN-ASW-0001,000	Dowel Pin Swashplate, 3mm	4	McMaster
26	24-PIN-AVP-0001,000	Dowel Pin Swashplate, 3mm	4	McMaster
27	24-SCR-AHO-0006,000	M10 Screw, 60mm L	4	McMaster
28	24-023-AHO-0003,000	Housing cap	1	ISSI

REFERENCES

- Becker, R. J. (1970). Quieting Hydraulic Systems and Components. In *SAE Technical Paper*. Milwaukee, WI, USA: SAE International. <https://doi.org/10.4271/700711>
- Berge, M. (now Ivantysynova, M.). (1983). *An investigation of viscous flow in lubricating gaps*. SVST.
- Deb, K., Pratap, A., Agarwal, S., & Meyarivan, T. (2002). A fast and elitist multiobjective genetic algorithm: NSGA-II. *IEEE Transactions on Evolutionary Computation*, 6(2), 182–197. <https://doi.org/10.1109/4235.996017>
- Edge, K. A., & Darling, J. (1986). Cylinder Pressure Transients in Oil Hydraulic Pumps with Sliding Plate Valves. *Proceedings of the Institution of Mechanical Engineers, Part B: Management and Engineering Manufacture*, 200(1), 45–54.
- Fang, Y., & Shirakashi, M. (1995). Mixed lubrication characteristics between the piston and cylinder in hydraulic piston pump-motor. *Journal of Tribology*, 117(1), 80–85. Retrieved from www.scopus.com
- Harrison, K. A., & Edge, K. A. (2000). Reduction of axial piston pump pressure ripple. *Proceedings of the Institution of Mechanical Engineers, Part I: Journal of Systems and Control Engineering*, 214(1), 53–64.
- Hashemi, S., Friedrich, H., Bobach, L., & Bartel, D. (2017). Validation of a thermal elastohydrodynamic multibody dynamics model of the slipper pad by friction force measurement in the axial piston pump. *Tribology International*, 115, 319–337. <https://doi.org/10.1016/J.TRIBOINT.2017.05.013>
- Hashemi, S., Kroker, A., Bobach, L., & Bartel, D. (2016). Multibody dynamics of pivot slipper pad thrust bearing in axial piston machines incorporating thermal elastohydrodynamics and mixed lubrication model. *Tribology International*, 96, 57–76. <https://doi.org/10.1016/J.TRIBOINT.2015.12.009>
- Helgestad, B. O., Foster, K., & Bannister, F. K. (2007). Pressure Transients in an Axial Piston Hydraulic Pump. *Proceedings of the Institution of Mechanical Engineers*, 188(1), 189–199. https://doi.org/10.1243/pime_proc_1974_188_021_02
- Huang, C., & Ivantysynova, M. (2003). A new approach to predict the load carrying ability of the gap between valve plate and cylinder block. In *Bath Workshop on Power transmission and Motion Control PTMC* (pp. 225–239).
- Ivantysyn, J., & Ivantysynova, M. (2001). *Hydrostatic Pumps and Motors, Principles, Designs, Performance, Modelling, Analysis, Control and Testing*. New Dehli, India: Academia Books International.

- Ivantysyn, R. (2011). *Computational design of swash plate type axial piston pumps a framework for computational design*. Retrieved from <http://search.proquest.com/docview/905253083?pq-origsite=gscholar>
- Ivantysynova, M. (1999). A new approach to the design of sealing and bearing gaps of displacement machines. In *Proceedings of the JFPS International Symposium on Fluid Power* (Vol. 1999, pp. 45–50). The Japan Fluid Power System Society.
- Ivantysynova, M., Huang, C., & Christiansen, S.-K. (2004). Computer Aided Valve Plate Design - An Effective Way to Reduce Noise. In *SAE Technical Paper*. SAE International. <https://doi.org/10.4271/2004-01-2621>
- Ivantysynova, M., Seeniraj, G. K., & Huang, C. (2005). Comparison of Different Valve Plate Designs Focusing. In *The Ninth Scandinavian International Conference on Fluid Power* (pp. 1–16). Linköping, Sweden.
- Johansson, A. (2005). *Design principles for noise reduction in hydraulic piston pumps : simulation, optimisation and experimental verification*. Linköping University.
- Johansson, A., Andersson, J., & Palmberg, J.-O. (2002). Optimal design of the cross-angle for pulsation reduction in variable displacement pumps. In *BATH WORKSHOP ON POWER TRANSMISSION AND MOTION CONTROL* (pp. 319–334). Bath, England, United Kingdom: Professional Engineering Publishing.
- Jouini, N., & Ivantysynova, M. (2008). Valve plate surface temperature prediction in axial piston machines. In *5th FPNI PhD Symposium*. Cracow, Poland.
- Kalbfleisch, P. K. (2015). *Computational valve plate design*. Purdue University. Retrieved from http://docs.lib.purdue.edu/open_access_theses
- Kim, D. A. (2012). *Contribution to digital prototyping of axial piston pumps/motors*. Purdue University.
- Kim, T., Kalbfleisch, P., & Ivantysynova, M. (2014). The effect of cross porting on derived displacement volume. *International Journal of Fluid Power*, 15(2), 77–85. <https://doi.org/10.1080/14399776.2014.923605>
- Kleist, A. (1997). Design of Hydrostatic Bearing and Sealing Gaps in Hydraulic Machines--a new Simulation Tool. In *Fifth Scandinavian International Conference on Fluid Power. SICFP* (Vol. 97, pp. 157–169).
- Klop, R. (2010). *Investigation of Hydraulic Transmission Noise Sources*. Purdue University.
- Manring, N. D. (2000). Tipping the Cylinder Block of an Axial-Piston Swash-Plate Type Hydrostatic Machine. *Transactions of the ASME*, 122(March), 216–221.

- Manring, N. D., & Dong, Z. (2004). The impact of using a secondary swash-plate angle within an axial piston pump. *TRANSACTIONS-AMERICAN SOCIETY OF MECHANICAL ENGINEERS JOURNAL OF DYNAMIC SYSTEMS MEASUREMENT AND CONTROL*, 126(1), 65–74.
- Olems, L. (2000). Investigations of the Temperature Behaviour of the Piston Cylinder Assembly in Axial Piston Pumps. *International Journal of Fluid Power*, 1(1), 27–39. <https://doi.org/10.1080/14399776.2000.10781080>
- Palmberg, J. O. (n.d.). Modelling of flow ripple from fluid power piston pumps. In *2nd Bath International Power Workshop, University of Bath, UK*.
- Pelosi, M. (2012). *An Investigation on the Fluid-Structure Interaction of Piston/Cylinder Interface*. Purdue University.
- Pelosi, M., & Ivantysynova, M. (2013). The Impact of Axial Piston Machines Mechanical Parts Constraint Conditions on The Thermo-Elastohydrodynamic Lubrication Analysis of The Fluid Film Interfaces. *International Journal of Fluid Power*, 14(3), 35–51.
- Pettersson, M., Weddfelt, K., & Palmberg, J. (1991). Methods of Reducing Flow Ripple from Fluid. In *SAE Technical Paper*. Milwaukee, WI, USA.
- Richardson, D., Sadeghi, F., Rateick, R. G., & Rowan, S. (2017). Experimental and Analytical Investigation of Floating Valve Plate Motion in an Axial Piston Pump. *Tribology Transactions*, 60(3), 537–547. <https://doi.org/10.1080/10402004.2016.1184733>
- Schenk, A. (2014). *Predicting Lubrication Performance between the Slipper and Swashplate in Axial Piston Hydraulic Machines*. Purdue University.
- Schenk, A., & Ivantysynova, M. (2011). Design and Optimization of the Slipper-Swashplate Interface Using an Advanced Fluid-Structure-Interaction Model. In *Proceedings of the 52nd National Conference on Fluid Power 2011* (pp. 91–100).
- Schenk, A., & Ivantysynova, M. (2015). A Transient Thermoelastohydrodynamic Lubrication Model for the Slipper/Swashplate in Axial Piston Machines. *Journal of Tribology*, 137(3), 031701. <https://doi.org/10.1115/1.4029674>
- Schenk, A., Zecchi, M., & Ivantysynova, M. (2013). Accurate Prediction of Axial Piston Machine's Performance Through a Thermo-Elasto-Hydrodynamic Simulation Model. *Proceedings of the ASME/BATH 2013 Symposium on Fluid Power & Motion Control*, 6–9.
- Seeniraj, G. K., & Ivantysynova, M. (2008). Multi-objective Optimization Tool for Noise Reduction in Axial Piston Machines. *SAE International Journal of Commercial Vehicles*, 1(1), 544–552. <https://doi.org/10.4271/2008-01-2723>
- Shang, L., & Ivantysynova, M. (2015). Port and case flow temperature prediction for axial piston

machines. *International Journal of Fluid Power*, 16(1), 35–51.
<https://doi.org/10.1080/14399776.2015.1016839>

Shang, L., & Ivantysynova, M. (2017). A temperature adaptive piston design for swash plate type axial piston machines. *International Journal of Fluid Power*, 18(1), 38–48.
<https://doi.org/10.1080/14399776.2016.1213115>

Wieczorek, U., & Ivantysynova, M. (2002). Computer aided optimization of bearing and sealing gaps in hydrostatic machines - The simulation tool CASPAR. *International Journal of Fluid Power*, 3(1), 7–20.

Zecchi, M. (2013). *A novel fluid structure interaction and thermal model to predict the cylinder block/valve plate interface performance in swash plate type axial piston machines*. Purdue University. Retrieved from <http://gradworks.umi.com/36/13/3613547.html>

VITA

Rene was born in January 22nd, 1989 in Chihuahua, Chihuahua, Mexico. He received his B.Sc. in Mechanical Engineering from the University of Texas at El Paso in 2011. After his bachelor's he worked in the aerospace industry for one year. In July 2012, he joined the Maha Fluid Power Research center at Purdue University as graduate research assistant. He earned his M.Sc. in Mechanical Engineering from Purdue University in August 2014 where his research focus was the investigation of impact of micro-surfacing in axial piston machines specifically in the cylinder block/valve plate interface. In the Fall 2014, also at Purdue University, he started the Ph.D. program and received his doctorate degree in August 2019. His main research interests are numerical modelling and virtual prototyping of axial piston machines of swash plate type, pumps and motors.

PUBLICATIONS

- Chacon, R. and Ivantysynova, M. 2014. An investigation of the impact of micro surface on the cylinder block/valve plate interface performance. *Proceedings of the 8th FPNI Ph.D Symposium on Fluid Power, Lappeenranta, Finland.*
- Chacon, R. and Ivantysynova, M. 2016. An Investigation of the Impact of the Elastic Deformation of the Endcase/Housing on Axial Piston Machines Cylinder Block/Valve Plate Lubricating Interface. *Proceedings of the 10th IFK International Conference on Fluid Power, Dresden, Germany, Vol. 1, pp. 283-294.*
- Chacon, R. and Ivantysynova, M. 2016. Advanced Virtual Prototyping of Axial Piston Machines. *Proceedings of the 9th FPNI Ph.D. Symposium on Fluid Power, October 26-28, 2016, Florianópolis, SC, Brazil. FPNI2016-1561*
- Chacon, R. and Ivantysynova, M. 2019. Thermal Effects on the Fluid Film in the Cylinder Block/Valve Plate Interface due to Compression and Expansion of the Fluid. *JFPS International Journal of Fluid Power System*, 2018, Volume 11, Issue 3, Pages 136-142, Released May 10, 2019, Online ISSN 1881-5286.
- Chacon, R. and Ivantysynova, M. 2019. Virtual Prototyping of Axial Piston Machines: Numerical Method and Experimental Validation. *Energies* **2019**, 12, 1674.